ABGAIL PAULA PINHEIRO

EULERIAN-LAGRANGIAN MODELLING OF AVIATION KEROSENE SPRAY BREAKUP AND EVAPORATION

UNIVERSIDADE FEDERAL DE UBERLÂNDIA
FACULDADE DE ENGENHARIA MECÂNICA
2022

ABGAIL PAULA PINHEIRO

EULERIAN-LAGRANGIAN MODELLING OF AVIATION KEROSENE SPRAY BREAKUP AND EVAPORATION

Tese apresentada ao Programa de Pós-Graduação em Engenharia Mecânica da Universidade Federal de Uberlândia, como parte dos requisitos para a obtenção do título de **DOUTOR EM ENGENHARIA MECÂNICA**.

Área de concentração: Transferência de Calor e Mecânica dos Fluidos.

Orientador: Prof. Dr. João Marcelo Vedovotto
Coorientador: Prof. Dr. Fernando Luiz Sacomano Filho

Uberlândia - MG
2022

Ficha Catalográfica Online do Sistema de Bibliotecas da UFU
com dados informados pelo(a) próprio(a) autor(a).

P654 Pinheiro, Abgail Paula, 1992-
2022 Eulerian-Lagrangian modelling of aviation kerosene spray breakup and evaporation [recurso eletrônico] / Abgail Paula Pinheiro. - 2022.

Orientador: João Marcelo Vedovotto.
Coorientador: Fernando Luiz Sacomano Filho.
Tese (Doutorado) - Universidade Federal de Uberlândia, Pós-graduação em Engenharia Mecânica.
Modo de acesso: Internet.
Disponível em: http://doi.org/10.14393/ufu.te.2022.357
Inclui bibliografia.

1. Engenharia mecânica. I. Vedovotto, João Marcelo , 1981-, (Orient.). II. Sacomano Filho, Fernando Luiz , 1985-, (Coorient.). III. Universidade Federal de Uberlândia. Pós-graduação em Engenharia Mecânica. IV. Título.

CDU: 621

Bibliotecários responsáveis pela estrutura de acordo com o AACR2:
Gizele Cristine Nunes do Couto - CRB6/2091
Nelson Marcos Ferreira - CRB6/3074

UNIVERSIDADE FEDERAL DE UBERLÂNDIA
Coordenação do Programa de Pós-Graduação em Engenharia Mecânica
Av. João Naves de Ávila, nº 2121, Bloco 1M, Sala 212 - Bairro Santa Mônica, Uberlândia-MG, CEP 38400-902
Telefone: (34) 3239-4282 - www.posgrad.mecanica.ufu.br - secposmec@mecanica.ufu.br

ATA DE DEFESA - PÓS-GRADUAÇÃO

Programa de Pós-Graduação em:	Engenharia Mecânica				
Defesa de:	Tese de Doutorado Acadêmico, nº 328, COPEM				
Data:	26/07/2022	Hora de início:	09:00	Hora de encerramento:	12:30
Matrícula do Discente:	11823EMC001				
Nome do Discente:	Abgail Paula Pinheiro				
Título do Trabalho:	Eulerian-Lagrangian modelling of aviation querosene spray atomisation and evaporation				
Área de concentração:	Transferência de Calor e Mecânica dos Fluidos				
Linha de pesquisa:	Dinâmica dos Fluidos e Transferência de Calor				
Projeto de Pesquisa de vinculação:					

Reuniu-se por meio de videoconferência a Banca Examinadora, designada pelo Colegiado do Programa de Pós-graduação em Engenharia Mecânica, assim composta: Professores Doutores: Francisco José de Souza - FEMEC/UFU; Aldemir Aparecido Cavalini Júnior - FEMEC/UFU; Sergei Stepanovich Sazhin - University of Brighton; Dirceu Noriler - UNICAMP; Ricardo Serfaty - PETROBRAS; Fernando Luiz Sacomano Filho (co-orientador) - USP e João Marcelo Vedovotto - FEMEC/UFU, orientador da candidata.

Iniciando os trabalhos, o presidente da mesa, Dr. João Marcelo Vedovotto, apresentou a Comissão Examinadora e a candidata, agradeceu a presença do público, e concedeu à Discente a palavra para a exposição do seu trabalho. A duração da apresentação da Discente e o tempo de arguição e resposta foram conforme as normas do Programa.

A seguir o senhor(a) presidente concedeu a palavra, pela ordem sucessivamente, aos(às) examinadores(as), que passaram a arguir o(a) candidato(a). Ultimada a arguição, que se desenvolveu dentro dos termos regimentais, a Banca, em sessão secreta, atribuiu o resultado final, considerando o(a) candidato(a):

Aprovada.

Esta defesa faz parte dos requisitos necessários à obtenção do título de Doutora.

O competente diploma será expedido após cumprimento dos demais requisitos, conforme as normas do Programa, a legislação pertinente e a regulamentação interna da UFU.

Nada mais havendo a tratar foram encerrados os trabalhos. Foi lavrada a presente ata que após lida e achada conforme foi assinada pela Banca Examinadora.

Documento assinado eletronicamente por **João Marcelo Vedovotto**, **Professor(a) do Magistério**

Superior, em 26/07/2022, às 12:26, conforme horário oficial de Brasília, com fundamento no art. 6º, § 1º, do Decreto nº 8.539, de 8 de outubro de 2015.

Documento assinado eletronicamente por **Francisco José de Souza**, **Professor(a) do Magistério Superior**, em 26/07/2022, às 12:26, conforme horário oficial de Brasília, com fundamento no art. 6º, § 1º, do Decreto nº 8.539, de 8 de outubro de 2015.

Documento assinado eletronicamente por **Fernando Luiz Sacomano Filho**, **Usuário Externo**, em 26/07/2022, às 12:27, conforme horário oficial de Brasília, com fundamento no art. 6º, § 1º, do Decreto nº 8.539, de 8 de outubro de 2015.

Documento assinado eletronicamente por **Dirceu Noriler**, **Usuário Externo**, em 26/07/2022, às 12:29, conforme horário oficial de Brasília, com fundamento no art. 6º, § 1º, do Decreto nº 8.539, de 8 de outubro de 2015.

Documento assinado eletronicamente por **Aldemir Aparecido Cavalini Junior**, **Professor(a) do Magistério Superior**, em 26/07/2022, às 12:32, conforme horário oficial de Brasília, com fundamento no art. 6º, § 1º, do Decreto nº 8.539, de 8 de outubro de 2015.

Documento assinado eletronicamente por **ricardo serfaty**, **Usuário Externo**, em 26/07/2022, às 12:34, conforme horário oficial de Brasília, com fundamento no art. 6º, § 1º, do Decreto nº 8.539, de 8 de outubro de 2015.

Documento assinado eletronicamente por **Sergei Stepanovich Sazhin**, **Usuário Externo**, em 26/07/2022, às 12:41, conforme horário oficial de Brasília, com fundamento no art. 6º, § 1º, do Decreto nº 8.539, de 8 de outubro de 2015.

A autenticidade deste documento pode ser conferida no site https://www.sei.ufu.br/sei/controlador_externo.php?acao=documento_conferir&id_orgao_acesso_externo=0, informando o código verificador **3771682** e o código CRC **D198FF6D**.

"When you go through deep waters, I will be with you."

Isaiah 43:2

Dedicated to my beloved family.

ACKNOWLEDGEMENTS

First and foremost, I am sincerely grateful to God for giving me health and strength to finish this stage of my academic life.

I thank my supervisors Prof. João Marcelo Vedovotto and Prof. Fernando Sacomano, each of whom has provided me patient advice and guidance throughout the research process. I would also like to thank the members of my doctoral committee, Prof. Sergei Sazhin, Prof. Dirceu Noriler, Dr. Ricardo Serfaty, Prof. Francisco José de Souza, and Prof. Aldemir Cavalini, for their constructive comments. Additionally, I like to acknowledge the valuable contribution of Dr. Oyuna Rybdylova and Dr. Ivan Zubrilin in this research when studying Jet A evaporation.

I would like to acknowledge the financial and technical support from Petróleo Brasileiro S.A. (Petrobras), National Counsel of Technological and Scientific Development (CNPq), Minas Gerais State Agency for Research and Development (FAPEMIG), and Coordination for the Improvement of Higher Education Personnel (CAPES). Also, I thank the Faculty of Mechanical Engineering of the Federal University of Uberlândia, the coordination, and the secretaries of the Postgraduate Program for their support in carrying out this work.

And, finally, I thank those whom without their support I would be completely lost: my family, my husband, and my friends. Thank you for always being by my side, no matter the distance or the situation, giving me all the love I needed to continue.

PINHEIRO, A. P., **Eulerian-Lagrangian modelling of aviation kerosene spray breakup and evaporation.** 2022. 124 p. PhD Thesis, Federal University of Uberlândia, Uberlândia.

ABSTRACT

A Discrete Component Model (DCM), based on the analytical solutions to heat transfer and species diffusion equations, together with the Abramzon-Sirignano model are applied to analyse the droplet heating and evaporation of Jet A kerosene and its surrogates. The composition of Jet A fuel used in the analysis, with 61 components split into 7 hydrocarbon groups, is described. This composition is approximated by twelve previously developed surrogates. The number of components in these surrogates varies between two and nine, which is expected to lead to a significant reduction in computational cost for calculation of droplet heating and evaporation. The models implemented into the in-house code MFSim are validated against available experimental results and the surrogates best able to predict droplet evaporation time and temperature of the Jet A fuel are identified. It is shown that the number of terms in the series of analytical solutions for temperature and species mass fractions can be considerably reduced almost without affecting the accuracy of calculations. Then, a hybrid deterministic-stochastic secondary breakup model is also included into the MFSim code. Its implementation is validated using a benchmark case of a non-evaporating spray by comparison of both spray penetration and Sauter Mean Diameter (SMD) with experimental data. Finally, Large-Eddy Simulations (LES) of high-speed evaporating sprays are performed using a Eulerian–Lagrangian modelling approach. For the continuous gas phase, the filtered continuity, momentum, energy, and species mass fraction equations are solved together with the dynamic subgrid turbulent kinetic energy equation. For the discrete liquid droplets, motion, atomisation, heating, and evaporation models are considered. Different heating and evaporation models are tested, either considering or not finite thermal conductivity and finite diffusivity inside droplets. Two types of spray flows are studied in this work due to their practical interest for aeronautical engines: liquid jet injection in quiescent environment and liquid jet injection into a gaseous crossflow. Based on the modelling results obtained, it was possible to demonstrate the influence of the liquid composition on its breakup behaviour. Even though considering temperature and species gradients inside droplets increases the computational cost, the present study arrived to the conclusion that they should be considered, especially in high-

temperature cases. Also, this research recommends considering the multicomponent nature of real fuels by using surrogates as a strategy for reducing computational cost.

Keywords: Droplet heating, Multicomponent evaporation, Aviation kerosene, Jet A, Surrogates, Droplet breakup, LES of two phase flows, Turbulent sprays, Numerical simulation, Eulerian-Lagrangian approach.

PINHEIRO, A. P., **Modelagem euleriana-lagrangiana da quebra e evaporação de spray de querosene de aviação.** 2022. 124 f. Tese de Doutorado, Universidade Federal de Uberlândia, Uberlândia.

RESUMO

Um modelo de componentes discretos (DCM), baseado nas soluções analíticas das equações de transferência de calor e difusão das espécies, juntamente com o modelo de Abramzon-Sirignano foram aplicados para analisar o aquecimento e evaporação de gotas de querosene do tipo Jet A e seus surrogates. A composição do combustível Jet A usada na análise, com 61 componentes divididos em 7 grupos de hidrocarbonetos, foi descrita. Esta composição foi aproximada por doze surrogates previamente desenvolvidos. O número de componentes nesses surrogates varia entre dois e nove, o que deve levar a uma redução significativa em custo computacional no cálculo do aquecimento e evaporação das gotas. Os modelos implementados no código próprio MFSim foram validados em relação a resultados experimentais disponíveis e os melhores surrogates em termos de previsão do tempo de evaporação e da temperatura das gotas de combustível Jet A foram identificados. Mostrou-se que o número de termos nas séries das soluções analíticas para temperatura e frações mássicas das espécies pode ser consideravelmente reduzido quase sem afetar a precisão dos cálculos. Em seguida, um modelo de quebra secundária híbrido determinístico-estocástico também foi incluído no código MFSim. Sua implementação foi validada usando um caso de referência de um spray não-evaporativo comparando-se a penetração do spray e do diâmetro médio de Sauter (SMD) com dados experimentais. Finalmente, Simulações das Grandes Escalas (LES) de sprays evaporativos com alta velocidade foram realizadas usando a abordagem do tipo euleriana-lagrangiana. Para a fase contínua gasosa, as equações filtradas da continuidade, quantidade de movimento, energia e frações mássicas das espécies foram resolvidas, juntamente com a equação da energia cinética turbulenta do modelo de submalha dinâmico. Para as gotas de líquido discretas, foram considerados os modelos de movimento, atomização, aquecimento e evaporação. Diferentes modelos de aquecimento e evaporação foram testados, considerando-se ou não condutividade térmica finita e difusividade finita no interior das gotas. Dois tipos de escoamentos com spray foram estudados neste trabalho devido ao seu interesse prático para motores aeronáuticos, sendo estes injeção de jato de líquido em ambiente quiescente

e injeção de jato de líquido em fluxo gasoso cruzado. Com base nos resultados de modelagem obtidos, foi possível demonstrar a influência da composição do líquido no seu comportamento de quebra. Embora considerar gradientes de temperatura e espécies dentro das gotas aumente o custo computacional, o presente estudo chegou à conclusão de que eles devem ser considerados, principalmente em casos de alta temperatura. Além disso, esta pesquisa recomenda considerar a natureza multicomponente dos combustíveis reais usando surrogates como uma estratégia para reduzir o custo computacional.

Palavras-chave: Aquecimento de gotas, Evaporação multicomponente, Querosene de aviação, Jet A, surrogates, quebra de gotas, LES de escoamentos bifásicos, Sprays turbulentos, Simulação numérica, Abordagem euleriana-lagrangeana.

List of Figures

List of Tables

Contents

CHAPTER I

INTRODUCTION

Liquid spray is a complex two-phase flow of primary importance in many natural physical processes and in a host of industrial and man-related activities. This phenomenon can be found in several engineering application fields such as, automotive and aeronautic engineering, fire suppression, painting, and medical aerosol (ZANG *et al.*, 2019). The physics of liquid sprays includes, among other processes, atomisation, dispersion, inter-phase heat, mass and momentum transfer, and turbulent mixing of chemical species, all occurring simultaneously, entangled in a complex way and at multiple spatial and temporal scales (JENNY; ROEKAERTS; BEISHUIZEN, 2012). Dealing with all these phenomena simultaneously and their interactions poses a tremendous modelling task. Some of the processes here mentioned are illustrated in Fig. 1.1.

Basically, in sprays, the liquid fuel needs to be atomised into droplets, which evaporate in a hot gas environment. In principle, the atomisation process can greatly influence on the evaporation process, since evaporation highly depends on the droplet surface area. When the atomisation occurs, due to the aerodynamic forces acting on them, the breakup events generate droplets of different sizes. After the bulk liquid is atomised, the physical system consists of discrete liquid droplets with a wide spectrum of diameters being dispersed in a turbulent gaseous phase. The standard modelling approach for liquid fuel atomisation is to use a two-step process, in which the region near the liquid injection is solved using a primary atomisation model and, once the bulk liquid is atomised into droplets, a secondary atomisation model is used (PAKSERESHT;

APTE, 2019). However, this research compute the atomisation process only based on secondary atomisation models. Moreover, collision and coalescence effects are neglected (SOMMERFELD; KUSCHEL, 2016; KAMP; VILLWOCK; KRAUME, 2017).

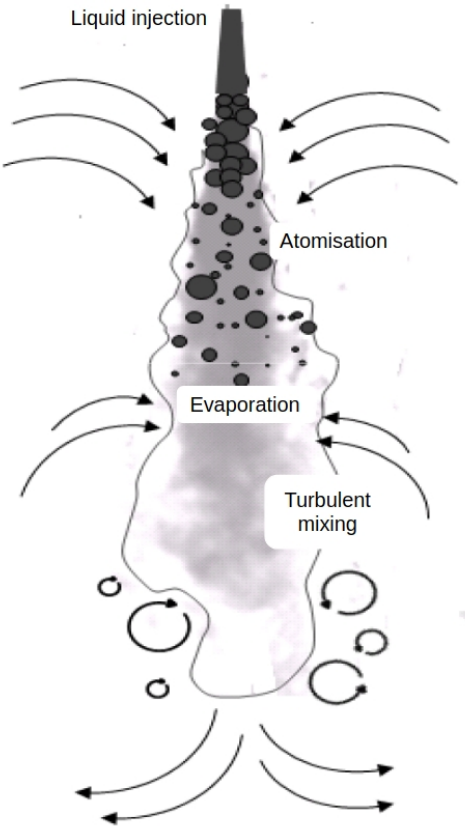

(a)

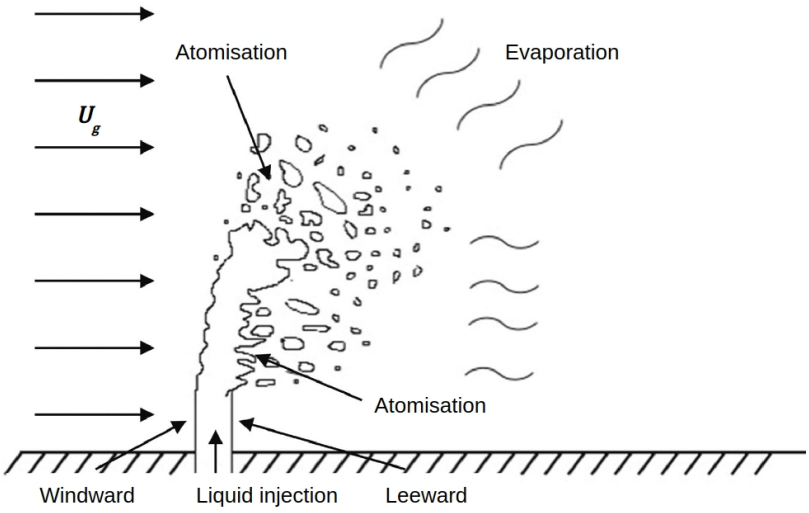

(b)

Figure 1.1: Schematic illustration of the two types of spray flows that are studied in this work due to their practical interest for aeronautical engines: (a) liquid jet injection into a still gas and (b) liquid jet injection into a gaseous crossflow - Adapted from Koesters (2012) and Wen *et al.* (2020).

Due to the very large number of droplets, resolving the detailed evolution of gas-liquid interfaces as well as the flow on both sides of the interfaces is not feasible considering the computational power currently available. Hence, within this research, the Eulerian-Lagrangian approach with an iterative two-way-coupling procedure is used, in which the continuous phase is the gaseous medium and the discrete phase is composed by the liquid droplets. In this approach, it is assumed that the volume fraction and the size of the dispersed phase is small compared to the computational cell used to discretise the continuous phase. Even though this assumption is not applicable to the region near the liquid injection (Fig. 1.1) (CAPECELATRO; DESJARDINS, 2013; EVRARD; DENNER; WACHEM, 2019), where a high volume fraction is observed, this hypothesis is still adopted in this research due to limitations in the thesis scope.

The complexities previously stated are further intensified when dealing with multicomponent liquid fuels. Different components evaporate at different rates, creating concentration gradients in the liquid phase and, therefore, causing mass diffusion inside the droplets. Coupled solutions between the dispersed and continuous phases, i.e. liquid droplets and gaseous medium, requires the computation of the species transport equation in the liquid phase, vapour-liquid equilibrium at the droplet surface and species transport equation in the gas phase, all these for each one of the multiple components. Therefore, the computational cost involved in simulating a fuel droplet evaporation increases as the number of components considered increases.

Mass diffusion is of primary importance in the evaporation process of a multicomponent fuel (SIRIGNANO, 2010). At first, for ideal mixtures, the more volatile substances at the droplet surface evaporates, leaving the less volatile components that evaporate slowly. Since the more volatile substance still exist in the droplet interior, they tend to diffuse toward the droplet surface due to the concentration gradients created previously. Consequently, the droplet composition can vary significantly during the droplet lifetime. Ignoring the presence of multiple components in fuel compositions means that species diffusion during droplet heating and evaporation is ignored or assumed infinitely fast. Also, once the droplets evaporate, the ambient composition also change.

Many studies of the modelling of droplet heating and evaporation of multicomponent fuels have been presented so far. However, in most cases, multicomponent fuels are simplified by assuming that they can be represented only using individual components (AL-QUBEISSI *et al.*, 2021). For instance, gasoline is usually represented by iso-octane (C_8H_{18}) and diesel by

n-tetradecane ($C_{14}H_{30}$)(RAUCH, 2018). Even though using single components in simulations might provide good results on a global scale, it is not possible to capture some important details, such as the selective evaporation of components that influences the vapour fuel and ambient gas mixture.

Although it is out of the scope of this work, it is important to highlight that evaporation and mixing are rate-controlling processes for combustion simulations, which supports the need of calculating such processes with accuracy. In other words, the atomised liquid fuel droplets should completely evaporate and the fuel vapour should mix with the ambient air before reaching the flame zone. Understanding multicomponent fuel droplet heating and evaporation are known to play a crucial role in the design and optimisation of liquid-fuelled internal combustion devices, since these two precombustion processes determine the fuel vapour concentration available in the environment and, thus, influence directly on the reaction rates (ECKEL *et al.*, 2019). Physically, as mentioned by Al-Qubeissi *et al.* (2021), several issues can arrive if droplets are not heated and evaporated properly, such as incomplete combustion, knocking, and high emissions.

Among the challenging tasks to be addressed in general topic of spray flows, modelling a complex multicomponent fuel evaporation focusing on computational cost stands out. Detailed models capable of capturing the relevant details, like the multicomponent nature of the fuels, are used here, and the feasibility of these models is also evaluated. Special attention has been paid here to computational costs in view of general modelling applications, particularly industrial usage for general spray flow modelling.

1.1 Importance of scientific and technological studies on Jet A

Crude oil, also known as petroleum, is a complex mixture of hydrocarbons. Atmospheric fractional distillation, illustrated in Fig. 1.2, is a process of separating many compounds present in crude oil by heating it, since each compound has its own boiling temperature (DAGAUT; CATHONNET, 2006). Aviation kerosene is distilled from crude oil at the distillation temperature range of 205 °C to 260 °C and it is composed mainly by alkanes, iso-alkanes, naphthenic and aromatic compounds, whose fuel composition directly influences the physicochemical characteristics of the fuel (DE-KLERK, 2012).

Aviation kerosene is the fuel used by airplanes and helicopters equipped with turbine engines, such as turbojets, turboshafts, turboprops, and turbofans. Piston engines, on the other hand, use aviation gasoline as fuel (CUMPSTY; HEYES, 2015). The liquid fuel atomisation and evaporation of aviation kerosene are important in both aero-engine combustion chamber design and spray combustion numerical simulation of propulsion and power systems. Deeply understanding the processes involved and being able to predict the behaviour of such processes by means of numerical simulations is important to enhance their efficiency.

The International Energy Agency (IEA) has estimated that the global oil production is approximately 76.9 million barrels per day in 2019, which is equivalent to an annual output of 3932 million tonnes. Aviation kerosene itself accounts for 8.5% of the total amount of oil produced. Although the COVID-19 pandemic caused a massive reduction in air travel demands, population increase is expected, especially in countries like China and India, as well as increase in the need for air travel (OLCAY *et al.*, 2018). In fact, according to Sundararaj *et al.* (2019), the world kerosene demand is projected to grow by 38% from 2008 to 2025. Consequently, studying aviation fuel is necessary to improve engine technologies and flight operations.

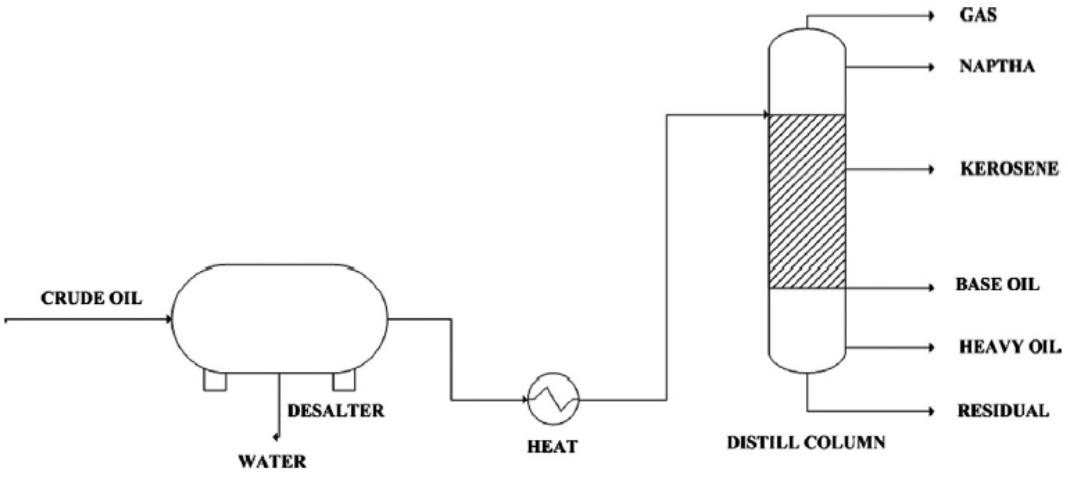

Figure 1.2: A schematic presentation of aviation kerosene production from crude oil (LIU; YAN; CHEN, 2013).

The two major jet fuel specifications for the aviation industry are the DS91-91 of the British Ministry of Defence defining Jet A-1, and the ASTM D1655, an American specification, defining Jet A. The main difference between Jet A-1 and Jet A is in the freezing point requirement Jet A has a maximum freezing point specification of -40 °C, whereas for Jet A-1 it is -47 °C,

which makes Jet A-1 more suitable for long international flights. The maximum freezing point is the temperature above which the fuel would completely solidifies. The United States mostly uses Jet A for national air travel and it is currently the most widely used civilian aviation fuel (BAUMI; BERTOSSE; GUEDES, 2020). Both fuel specifications, DS91-91 and ASTM D1655, do not explicitly define the fuel composition, but instead they indicate minimum and maximum requirements on performance, material and manufacture properties, which results in a range of possible composition. This study aims to investigate particularly Jet A.

Moreover, in relation to the Brazilian context, the ANP (*Agência Nacional do Petróleo, Gás Natural e Biocombustíveis* or National Agency of Petroleum, Natural Gas and Biofuels) approved a new resolution, number 856, on 21 October 2021, which authorises the introduction of Jet A type aviation kerosene in the Brazilian market. Before this resolution, only Jet A-1 was allowed for in the country. As stated by Oliveira (2021), this new guideline represents a great advance for the Brazilian aviation industry, as it allows the expansion of possible importation origins and increases the potential for cost reduction. According to a study carried out by the ANP, a cost reduction of up to 0.6% is estimated for airlines operating in Brazil, which represents about 10 million dollars per year (NOVAES, 2021). Thus, studying Jet A is also relevant in a national context.

1.2 Objectives

The objective of this thesis is to contribute to the development of computationally efficient numerical models of multicomponent evaporative sprays for industrial applications based on the Eulerian-Lagrangian methodology. This includes finding, implementing and validating methodologies of best practice, which are robust and reliable. More specifically, focus is given on atomisation and evaporation of a Jet A spray in this research. All the simulations are performed using the MFSim, and the results are either compared to experimental data obtained from the literature or parametrically analysed by means of artifical cases.

In order to accomplish the object of this work, the following steps are considered:

1. Generalisation of the Abramzon-Sirignano model implementation for monocomponent evaporation (PINHEIRO, 2018) to multicomponent;

2. Implementation of:

    - droplet breakup model for atomisation;
    - conduction-limit model for droplet heating;
    - discrete components model for liquid phase mass diffusion;
    - effective-conductivity and effective-diffusivity models to consider the effect of recirculation inside the droplets;

3. Characterization of Jet A composition and the thermodynamic and transport properties of each component for liquid and gas phases;

4. Evaluation of some surrogates proposed in the literature for Jet A specifically focusing on the heating and evaporation behaviour;

5. Implementation of the Eulerian-Lagrangian interaction terms due to droplet heating and evaporation;

6. Simulation of several cases in order to verify the implementations and to better understand the processes involved in spray heating and evaporation.

1.3 Computational platform

The focus of the present research is not only on the physical modelling of spray heating and evaporation, but also the development of efficient algorithms for performing the simulations. For a successful simulation of spray heating and evaporation it is crucial to have a well-established computational code, in which all necessary model components can be integrated efficiently. The in-house Computational Fluid Dynamic (CFD) code MFSim is employed in the current study. It has been developed by the research group of the Fluid Mechanics Laboratory (MFLab) of the Federal University of Uberlândia over the last 10 years in cooperation with a large research group, and it consists of hundreds of thousands of lines of code, in which enormous amount of effort and knowledge were invested to build the resulting code. The main advantages of developing an in-house code are the full accessibility, full transparency, and relatively straightforward possibility to change and implement new models.

Some preliminary works recently done in the MFLab are especially important as a starting point to assure the achievement of the present thesis objectives. The transport equations of linear momentum, energy, and species mass fractions for the continuous phase species are already implemented and prepared to receive the coupling terms coming from the Lagrangian motion, heating and evaporation (DAMASCENO, 2018). Particle tracking algorithms for the disperse phase and subgrid velocity effect on the particle motion have been implemented and validated (SANTOS, 2019).

So far, in terms of droplet heating and evaporation, only the infinite conductivity model, with uniform, but time-varying, droplet temperature, is available in the code (PINHEIRO, 2018). Hence, the temperature gradients inside the droplet are neglected, which is only appropriate for large Fourier number (RYBDYLOVA *et al.*, 2016). The evaporation models for monocomponent droplets can be adapted to multicomponent droplets. However, for multicomponent droplets species diffusion should be also taken into account. It is important to highlight that the new models implemented during this work in order to simulate a multicomponent spray atomisation, heating and evaporation are integrated with all the previously existing functionalities of the MFSim code, enabling a wide range of simulations for future applications.

1.4 Thesis outline

The present thesis consists of 6 chapters and 1 appendix. The remainder of this manuscript is organised in the following manner. In Chapter 2, the mathematical model for the Eulerian-Lagrangian approach, with the inter-phase coupling terms, is exhibited. In Chapter 3, the theoretical background about heating and evaporation of multicomponent droplets is explained, including the mathematical models used and some numerical and computational details, information about Jet A and its surrogates are gathered, and the results obtained are discussed. In Chapter 4, the atomisation model used is described and the results of its validation for a non-evaporating spray are presented. In Chapter 5, the results of a range of simulations performed are discussed. In Chapter 6, the major findings are summarised, general conclusions are drawn and some recommendations are given for future works. Finally, Appendix A is dedicated to display the thermodynamic and transport properties database used in this work.

CHAPTER II

EULERIAN-LAGRANGIAN MODEL

For spray combustion simulations the Eulerian-Lagrangian approach is widely employed, especially for dilute spray simulations, where the ratio between In the Lagrangian viewpoint, each individual droplet is tracked in its own frame of reference and ordinary differential equations are considered to determine their temporal evolution of position, velocity, diameter, and temperature. Point droplet approximation is assumed in the Lagrangian approach, while the continuous phase is modelled by mass, momentum, energy, and species transport equations computed based on the Eulerian viewpoint.

The heating and evaporation of Lagrangian droplets deeply impact the Eulerian variables spatial and temporal distributions, especially in the regions where droplets are encountered. The mixing between the fuel vapour released by the evaporating droplets and the surrounding gaseous phase, as well as the energy transfer between gaseous and liquid phases are treated here. Scalar gradients of temperature and species mass fraction, are the main variables affected, which also impact the computation of physical properties, such as density and viscosity.

2.1 Mathematical model

The present work is performed based on the Eulerian-Lagrangian framework, in which the continuous gaseous phase is modelled by the transport equations shown in the first part of this section. The dispersed liquid phase, based on Lagrangian referential is presented in the second

part of this section. Finally, the coupling between the two phases is achieved by the transfer terms presented in the third part of this section.

2.1.1 Continuous phase

The transport equations for of mass, momentum, energy, and mass of each species are given by the following partial differential equations:

$$\frac{\partial \rho}{\partial t} + \frac{\partial \rho u_i}{\partial x_i} = {S_m}^L, \tag{2.1}$$

$$\frac{\partial \rho u_i}{\partial t} + \frac{\partial \rho u_i u_j}{\partial x_i} = -\frac{\partial p}{\partial x_i} + \frac{\partial \tau_{ij}}{\partial x_i} + {S_{u,i}}^L, \tag{2.2}$$

$$\frac{\partial \rho c_p T}{\partial t} + \frac{\partial \rho u_i c_p T}{\partial x_i} = -\frac{\partial q_i}{\partial x_i} + \tau_{ij}\frac{\partial u_i}{\partial x_j} + {S_{c_pT}}^L, \tag{2.3}$$

$$\frac{\partial \rho Y_k}{\partial t} + \frac{\partial \rho u_i Y_k}{\partial x_i} = -\frac{\partial J_{k,i}}{\partial x_i} + {S_k}^L, \tag{2.4}$$

where ρ is the density, u_i the velocity in the i direction, p the pressure, τ_{ij} the viscous stress tensor, T the gas temperature, c_p the specific heat capacity at constant pressure, k the thermal conductivity, and Y_k is the mass fraction of the kth species. q_i is the heat flux and $J_{k,i}$ is the molecular diffusion flux of species, which are evaluated based on the Fourier's and Fick's laws, respectively (BIRD; LIGHTFOOT; STEWART, 2002). In the present research, Soret and Dufour effects are both neglected. ${S_m}^L$, ${S_{u,i}}^L$, ${S_{c_pT}}^L$, and ${S_k}^L$ are the mass, momentum, energy, and species sources terms to account for the existence of the Lagrangian phase. t represents time and $(i = 1, 2, 3)$ represent the three directions in space.

Considering a Newtonian fluid, the viscous stress tensor is given by:

$$\tau_{ij} = \mu \left(\frac{\partial u_i}{\partial x_j} + \frac{\partial u_j}{\partial x_i} \right) - \frac{2}{3} \mu \frac{\partial u_k}{\partial x_k} \delta_{ij}, \tag{2.5}$$

where μ is the viscosity and δ_{ij} is the Kronecker delta tensor.

A key factor in the prediction of high-speed liquid jet sprays is accurate modelling the interaction between gas and liquid phases. Due to the unsteady and turbulent nature of the gas flow resulting from high-speed sprays, as well as the intrinsically transient behaviour of the other physical processes happening in the liquid droplets, Large-Eddy Simulation (LES) is considered more suitable than Reynolds-Averaged Navier-Stokes (RANS) to capture such features, although the latter is widely useful for the design of practical engineering systems Irannejad and Jaberi (2014). Therefore, the LES methodology is used in this work.

Since of shaky and turbulent nature of the gas stream produced by high-speed showers and other intrinsically transitory physical forms included in a commonplace building framework, Large-Eddy Recreation (LES) is anticipated to be more reasonable than Reynolds-Averaged Navier-Stokes (RANS), indeed in spite of the fact that the last mentioned remains to be valuable for the plan of commonsense frameworks

2.1.1.1 Filtered transport equations

The main idea behind the LES methodology is to compute the largest structures of the flow field, typically larger than the computational grid, whereas the non-linear interaction between large and sub-grid scales are modelled. In the present work a box filter in physical space is adopted. A filtered quantity f is defined as:

$$\overline{f}(\mathbf{x}) = \int f(\mathbf{x}') F(\mathbf{x} - \mathbf{x}') d\mathbf{x}', \tag{2.6}$$

where F is the LES filter, defined as:

$$F(\mathbf{x}) = F(x_1, x_2, x_3) = \begin{cases} 1/\Delta^3 & \text{, if } |x_i| \leq \Delta,\ i = 1, 2, 3 \\ 0 & \text{, otherwise} \end{cases}, \tag{2.7}$$

where (x_1, x_2, x_3) are the spatial coordinates of the vector $\mathbf{x}$, and $\Delta = \sqrt[3]{V_c}$ is a cubic box of size equivalent to that of the finite-volume grid retained for discretising the transport equations in the Eulerian field, and V_c is the volume of a mesh element.

In variable density flows it is useful to define the mass-weighted Favre filtering:

$$\overline{\rho}\tilde{f}(\mathbf{x}) = \int \rho f(\mathbf{x}') F(\mathbf{x} - \mathbf{x}') d\mathbf{x}'. \tag{2.8}$$

The filtered quantities $\overline{f}$ and $\tilde{f}$ are computed by the numerical simulations. The fluctuations $f' = f - \overline{f}$ are the unresolved, subgrid scale part of the quantity f. Therefore, the gas flow is simulated by solving the following filtered equations:

$$\frac{\partial \overline{\rho}}{\partial t} + \frac{\partial \overline{\rho}\tilde{u}_i}{\partial x_i} = \overline{S_m{}^L}, \tag{2.9}$$

$$\frac{\partial \overline{\rho}\tilde{u}_i}{\partial t} + \frac{\partial \overline{\rho}\tilde{u}_i\tilde{u}_j}{\partial x_i} = -\frac{\partial \overline{p}}{\partial x_i} + \frac{\partial \bar{\tau}_{ij}}{\partial x_i} - \frac{\partial \tau_{ij}^{\mathrm{sgs}}}{\partial x_j} + \overline{S_{u,i}{}^L}, \tag{2.10}$$

$$\frac{\partial \overline{\rho}\widetilde{c_pT}}{\partial t} + \frac{\partial \overline{\rho}\tilde{u}_i\widetilde{c_pT}}{\partial x_i} = -\frac{\partial (\overline{q_i} + q_i{}^{\mathrm{sgs}})}{\partial x_i} + \frac{\partial [(\bar{\tau}_{ij} - \tau_{ij}^{\mathrm{sgs}})\tilde{u}_i]}{\partial x_j} + \overline{S_{c_pT}{}^L}, \tag{2.11}$$

$$\frac{\partial \overline{\rho}\tilde{Y}_k}{\partial t} + \frac{\partial \overline{\rho}\tilde{u}_i\tilde{Y}_k}{\partial x_i} = -\frac{\partial (\overline{J_{k,i}} + J_{k,i}{}^{\mathrm{sgs}})}{\partial x_i} + \overline{S_k{}^L}, \tag{2.12}$$

where sgs represent the subgrid-scale (SGS) terms.

2.1.1.2 Subgrid-scale models

The unclosed SGS terms in the filtered equations are closed here by gradient type closures (LEBOISSETIER; OKONG'O; BELLAN, 2005). The unresolved subgrid stress tensor τ_{ij}^{sgs} is

expressed according to the Boussinesq assumption (FERZIGER; PERIĆ; STREET, 2002):

$$\tau_{ij}^{\text{sgs}} - \frac{\delta_{ij}}{3}\tau_{kk}^{\text{sgs}} = \mu_{\text{sgs}}\left(\frac{\partial \tilde{u}_i}{\partial x_j} + \frac{\partial \tilde{u}_j}{\partial x_i} - \frac{2}{3}\frac{\partial \tilde{u}_k}{\partial x_k}\delta_{ij}\right) = 2\mu_{\text{sgs}}\left(\tilde{S}_{ij} - \frac{\delta_{ij}}{3}\tilde{S}_{kk}\right), \tag{2.13}$$

where μ_{sgs} is the subgrid or turbulent viscosity and $\tilde{S}_{ij}$ is the strain rate tensor of the resolved field.

In the dynamic Smagorinsky model (GERMANO *et al.*, 1991), with the modifications proposed by (LILLY, 1992), the eddy viscosity μ_{sgs} is obtained by assuming that the small scales are in equilibrium, so that energy production and dissipation are in balance:

$$\mu_{\text{sgs}} = 2\bar{\rho}(C_s\Delta)^2|\tilde{S}| = 2\bar{\rho}(C_s\Delta)^2\left(2\tilde{S}_{ij}\tilde{S}_{ij}\right)^{1/2}, \tag{2.14}$$

where the constant C_s is evaluated using the dynamical procedure as described in details by Vedovoto (2011).

The unresolved subgrid heat and diffusion fluxes, ${q_i}^{\text{sgs}}$ and ${J_{k,i}}^{\text{sgs}}$, are also modelled with similar gradient type closures as:

$${q_i}^{\text{sgs}} = -\bar{\rho}\frac{\mu_{\text{sgs}}}{Pr_t}\frac{\partial \widetilde{c_p T}}{\partial x_i}, \tag{2.15}$$

$${J_{k,i}}^{\text{sgs}} = -\bar{\rho}\frac{\mu_{\text{sgs}}}{Sc_t}\frac{\partial \tilde{Y}_k}{\partial x_i}, \tag{2.16}$$

where Pr_t and Sc_t are turbulent Prandtl and Schmidt numbers, respectively.

For more details on the mathematical model of the Eulerian phase, the reader can refer to previous works developed in the MFLab, such as Vedovoto (2011), Melo (2017) and Damasceno (2018).

2.1.2 Discrete phase

In this section, the approach used for modelling droplet dispersion, heating, and evaporation is presented. The formulation for droplet atomisation is later presented in Chapter 4. It is

important to highlight that the equations presented in this section are only valid as they are for monocomponent evaporation and if it is assumed no temperature gradient inside the droplets. This model based on the assumption that there is no temperature gradient inside the droplets is known as the Infinite Thermal Conductivity (ITC) model. The generalisation of the Abramzon-Sirignano model (ABRAMZON; SIRIGNANO, 1989) for multicomponent droplets is presented in Section 3.1 of the next chapter, as well as the models in which temperature and concentration gradients inside the droplets are taken into account.

2.1.2.1 Droplet motion

For engineering applications involving spray evaporation, the droplet drag force and the gravitational force are predominant compared to other forces, such as Basset history, added mass, Magnus, Saffman, buoyancy, and pressure gradient terms (SHIROLKAR; COIMBRA; MCQUAY, 1996). Under these conditions and considering the Lagrangian approach, droplet motion and momentum equations are:

$$\frac{dx_{d,i}}{dt} = u_{d,i}, \tag{2.17}$$

$$m_d \frac{du_{d,i}}{dt} = \sum F_{d,i} = \frac{u_i - u_{d,i}}{\tau_d} + g_i, \tag{2.18}$$

where $x_{d,i}$ and $u_{d,i}$ are droplet position and velocity respectively, u_i is the carrier gas velocity, , and g_i is the gravitational acceleration. The droplet relaxation time, τ_d, is determined by:

$$\tau_d = \frac{4}{3}\frac{\rho_l}{\rho_g}\frac{D_d}{C_D|u_i - u_{d,i}|}, \tag{2.19}$$

where ρ_l and ρ_g, respectively, refer to liquid droplet and gas phase densities and $|u_i - u_{d,i}|$ is the slip velocity. Note that the droplet mass variation due to evaporation is neglected in Eq. 2.18.

The drag coefficient, C_D, is given by semi-empirical correlations. The correlation proposed by Feng and Michaelides (2001) for viscous spheres is used here, in which λ is the viscosity ratio of the internal to the external fluid viscosity, or, for liquid spray applications, $\lambda = \mu_l/\mu_g$. Many

analytical and numerical solutions for the drag coefficients of solid spheres ($\lambda \to \infty$) or inviscid bubbles ($\lambda \to 0$) exist in the literature (CLIFT; GRACE; WEBER, 2005; MICHAELIDES, 2006). However, very few actually take into consideration that the internal flow in viscous spheres is important in the determination of the hydrodynamic force.

$$C_D = \frac{8}{Re_d}\frac{3\lambda+2}{\lambda+1}\left(1+0.05\frac{3\lambda+2}{\lambda+1}Re_d\right) - 0.01\frac{3\lambda+2}{\lambda+1}Re_d \ln\left(Re_d\right), \quad \text{if} \quad 0 \leq Re_d \leq 5, \tag{2.20}$$

where the droplet Reynolds number, Re_d, is defined as:

$$Re_d = \frac{\rho_g D_d |u_i - u_{d,i}|}{\mu_g}. \tag{2.21}$$

$$C_D = \begin{cases} \frac{2-\lambda}{2}C_{D,0} + \frac{4\lambda}{6+\lambda}C_{D,2}, & \text{if} \quad 5 < Re_d \leq 1000 \quad \text{and} \quad 0 \leq \lambda \leq 2 \\ \frac{4}{\lambda+2}C_{D,2} + \frac{\lambda-2}{\lambda+2}C_{D,\infty}, & \text{if} \quad 5 < Re_d \leq 1000 \quad \text{and} \quad 2 < \lambda \leq \infty \end{cases}, \tag{2.22}$$

where the functions $C_{D,0}$, $C_{D,2}$ and $C_{D,\infty}$ are given by:

$$C_{D,0} = \frac{48}{Re_d}\left(1 + \frac{2.21}{\sqrt{Re_d}} - \frac{2.14}{Re_d}\right), \tag{2.23}$$

$$C_{D,2} = 17.0 {Re_d}^{-2/3}, \tag{2.24}$$

and

$$C_{D,\infty} = \frac{24}{Re_d}\left(1 + \frac{1}{6}{Re_d}^{2/3}\right). \tag{2.25}$$

Finally,

$$C_D = 0.44, \quad \text{if} \quad Re_d > 1000. \tag{2.26}$$

For more details on the mathematical model presented in this section, the reader can refer to previous works developed in the MFLab, such as Pinheiro (2018) and Santos (2019).

2.1.2.2 Droplet heating and evaporation

The energy and mass transfers resulting from the heating and evaporation processes are described by differential equations, which express the temporal changes of droplet size and temperature:

$$\frac{dm_d}{dt} = -\dot{m}_d, \tag{2.27}$$

where m_d is the droplet mass and $\dot{m}_d$ is the droplet evaporation rate.

$$\frac{dD_d}{dt} = -\frac{2\dot{m}_d}{\pi\rho_l {D_d}^2}, \tag{2.28}$$

where D_d is the droplet diameter and ρ_l is the liquid droplet density.

$$\frac{dT_d}{dt} = \frac{\dot{Q}_S}{m_d c_l}, \tag{2.29}$$

where T_d is the droplet temperature, c_l is the liquid droplet specific heat capacity and recalling that $\dot{Q}_S$ is the power transferred to promote the droplet thermal energy variation per unit of time, which is transferred as heat.

Considering the model proposed by Abramzon and Sirignano (1989):

$$\dot{m}_d = \pi D_d D_{v,m} \rho_m Sh_m \ln\left(1 + B_M\right), \tag{2.30}$$

$$\dot{Q}_S = \frac{\ln\left(1 + B_T\right)}{B_T} \pi D_d Nu_m k_m \left(T_g - T_d\right) - L_v \dot{m}_d, \tag{2.31}$$

where D_v is the vapour diffusion coefficient, L_v is the vapour latent heat, ρ is the density, k is the thermal conductivity, subscript m represents that the physical properties are evaluated at the gas-vapour mixture conditions in the film around the droplet, Sh and Nu are the modified Sherwood

and Nusselt numbers proposed by Abramzon and Sirignano (1989), B_M is the Spalding mass transfer number, B_T is the Spalding thermal energy transfer number, and T_g is the carrier gas temperature. More details on calculation of these parameters are given in Section 3.1. For more details on the mathematical model presented in this section, the reader can refer to previous works developed in the MFLab, such as Pinheiro (2018), Pinheiro and Vedovoto (2019) and Pinheiro, Vedovoto and Silveira-Neto (2019).

2.1.3 Inter-phase coupling

The effects of droplets on the carrier gas are included via a series of source/sink terms in the continuous phase equations based on the Particle-Source-In-Cell (PSI-Cell) method (CROWE; SHARMA; STOCK, 1977). These inter-phase coupling terms are evaluated by volumetric averaging and interpolation of the Lagrangian droplet quantities as:

$$S_m{}^L = \frac{1}{V_c}\sum_1^{n_d} \dot{m}_d, \tag{2.32}$$

$$S_{u,i}{}^L = \frac{1}{V_c}\sum_1^{n_d} \left[m_d \left(\frac{du_{d,i}}{dt} - g_i \right) + \dot{m}_d u_i \right], \tag{2.33}$$

$$S_{c_pT}{}^L = \frac{1}{V_c}\sum_1^{n_d} \left[m_d \frac{d\left(c_l T_d\right)}{dt} - \dot{m}_d L_v \right], \tag{2.34}$$

$$S_k{}^L = \frac{1}{V_c}\sum_1^{n_d} \dot{m}_d \varepsilon_k, \tag{2.35}$$

where ε_k is fractional evaporation rate of the kth species, which is given by Eq. 3.45 and n_d is the number of droplets inside a certain Eulerian cell of volume V_c.

2.2 Numerical details

The MFSim code is a computational framework able to solve monophasic and multiphasic turbulent flows using Lagrangian and Eulerian based numerical methods on an adaptive, block-structured mesh (VILLAR, 2007). It uses a semi-backward difference (SBDF) method to discretise the filtered momentum transport equations. It treats the diffusive term implicitly and the advective term explicitly. For the discretisation of the advective terms, the total variation diminishing method CUBISTA (ALVES; OLIVEIRA; PINHO, 2003) and the second-order central difference scheme (FERZIGER; PERIĆ; STREET, 2002) to approximate diffusive terms of the transport equations are applied. Scalar variables, such as pressure, density, viscosity, and species mass fractions, are located at the cell center, and velocity components are stored on cell faces according to the staggered arrangement (DAMASCENO; SANTOS; VEDOVOTO, 2018).

The flow variables evolve on an adaptive, block-structured mesh. There is a certain interest in locally refining regions of instabilities in the flow, regions of high turbulent intensity, regions close to walls, regions where you have the interface between two fluids and even regions with the presence of particles (DENNER *et al.*, 2014; SANTOS, 2019). As the refinement can be positioned only where it is necessary, it is possible to reduce the computational cost while still guaranteeing numerical accuracy. The resulting mesh is easily parallelized compared to unstructured meshes. Lima (2012) discoursed on MFSim parallelization methods and used Message Passing Interface (MPI) (GROPP *et al.*, 1996; GABRIEL *et al.*, 2004) to communicate Eulerian based data among processes. The same approach is used to communicate Lagrangian information using the parallel Lagrangian map (CASTRO *et al.*, 2021). The multigrid-multilevel technique, which employs the successive over-relaxation iterative solver to provide numerical solution for the Poisson equation, must be used because the diffusive terms of momentum equation are treated implicitly by the temporal discretisation scheme (VILLAR, 2007; LIMA, 2012).

A classical fractional step method (CHORIN, 1968; COLELLA; PAO, 1999) solves pressure and velocity separately and sequentially. First, it determines an auxiliary filtered velocity field based on the filtered momentum transport equations, at this point without regards to mass conservation. Further, a Poisson equation provides an estimated filtered pressure based on the auxiliary filtered velocity field. Then, the method forces the auxiliary filtered velocity field to fit

mass conservation, correcting auxiliary filtered velocity with the estimated filtered pressure. After these steps, the filtered velocity field obeys mass conservation (VILLAR, 2007).

All the data structure used to represent the Lagrangian droplets computationally and store their properties is based on a hash table. The application of this table in the MFSim code is made through the Uthash package, developed by Hanson (2013) and implemented in C. For this reason, much of the Lagrangian module is developed in this same language, even though the base structure of MFSim code and the Eulerian module are developed in Fortran. The barycentric interpolation method is used (SCHERER, 2013) to estimate the values of the mean field variables at a certain particle position. For more details on the Lagrangian solver structure and the models of the Lagrangian phase, the reader can refer to previous works developed in the MFLab, such as Ferreira (2015), Silva (2016), Pinheiro (2018) and Santos (2019).

CHAPTER III

DROPLET HEATING AND EVAPORATION MODEL

This work focuses on the modelling of aviation kerosene droplets, more specifically Jet A. This liquid fuel includes many dozens of components, so for realistic engineering sprays, rigorous modelling of the contribution of each component might be problematic, due to the excessive CPU requirements. To address this issue, various simplifications have been proposed in the literature aiming to reduce the number of variables and, thus, the computational expense. The Distillation Curve Model (BURGER *et al.*, 2003) and the Continuous Thermodynamics Model (HALLETT; LEGAULT, 2011), have been widely used, but their major limitation is that both models are based on the assumption of infinitely fast diffusivity of species inside droplets (SAZHIN, 2014). The Multi-Dimensional Quasi-Discrete Model suggested in Sazhin *et al.* (2014), and further developed in Al-Qubeissi, Al-Esawi and Sazhin (2021), takes into account the diffusion of species inside droplets and it could be potentially applied for modelling of Jet A droplet heating and evaporation without excessive CPU requirements (AL-QUBEISSI; AL-ESAWI; SAZHIN, 2021). This model, however, is based on the introduction of quasi-components with non-integer values of carbon numbers, which limits its application to the modelling of ignition and general combustion processes.

A promising approach to the approximation of Jet A, which would allow the modelling of heating and evaporation of droplets, as well as ignition and combustion of fuel vapour-air mixture, could be to replace its hundreds of components with a surrogate containing only a

few components. Results of preliminary research in this direction are presented in Poulton *et al.* (2020). Poulton *et al.* (2020) considered a number of kerosene surrogates, selected mainly based upon their ignition and combustion characteristics, and they investigated how well heating and evaporation of kerosene droplets can be predicted if using the surrogates as opposed to the composition presented in Lissitsyna *et al.* (2014). The fact that Poulton *et al.* (2020) did not make a distinction between the different types of kerosene limits the applicability of their analysis. Additionally, some simplifications used in the analysis presented in Poulton *et al.* (2020) turned out to be too crude for accurate investigation of droplet heating and evaporation.

The present research addresses essentially the same problem as considered in Poulton *et al.* (2020), but using a rather different approach to its solution. Firstly, the analysis is restricted to Jet A and surrogates developed specifically for this fuel. Secondly, a number of improvements to the model used in Poulton *et al.* (2020) have been made, which are described later in this chapter. Thirdly, the model was implemented in the in-house code MFSim, which is written in the C programming language, opening the way for modelling the droplet heating and evaporation process alongside other spray processes.

This chapter is organized as follows. In Sections 3.1 and 3.2, the mathematical model for multicomponent droplet heating and evaporation is presented with numerical and computational details. The composition of Jet A and its surrogates are described in Section 3.3. In Section 3.4, transport and thermodynamic properties of both liquid and vapour phases are summarised. In Section 3.5, the results of calculations are presented and discussed. Section 3.6 summarises the main conclusions achieved based on the results presented in this chapter. It is important to highlight that this whole chapter comes from a paper previously published by Pinheiro *et al.* (2021).

3.1 Mathematical model

A Discrete Component Model (DCM), based on the analytical solutions to heat transfer and species diffusion equations, together with the Abramzon-Sirignano model, are applied to analyse the droplet heating and evaporation of multicomponent droplets. In this section, the formulation of the problem is presented. It is important to highlight that thermal radiation effect

is not considered in this research (ABRAMZON; SAZHIN, 2006).

3.1.1 Evaporation rate

Based on a detailed investigation of different evaporation models (PINHEIRO; VEDOVOTO, 2019), the Abramzon-Sirignano model (ABRAMZON; SIRIGNANO, 1989), generalised to multi-component droplets in Continillo and Sirignano (1989), is used for the analysis of the processes in the gas phase. In this model, the droplet evaporation rate $\dot{m}_d$ is estimated as:

$$\dot{m}_d = 2\pi R_d D_{v,m} \rho_m Sh_m \ln\left(1 + B_M\right), \tag{3.1}$$

where R_d is the droplet radius, D_v is the vapour diffusion coefficient, ρ is the density, subscript m represents that the physical properties are evaluated at the gas-vapour mixture conditions in the film around the droplet, Sh is the modified Sherwood number proposed by Abramzon and Sirignano (1989) and B_M is the Spalding mass transfer number.

$$Sh_m = 2 + \frac{Sh_0 - 2}{F_M}, \tag{3.2}$$

$$F_M = (1 + B_M)^{0.7} \frac{\ln(1 + B_M)}{B_M}, \tag{3.3}$$

The well-known Ranz-Marshall empirical correlation (RANZ; MARSHALL, 1952), with the modification proposed by Li and Mason (2000) for high Reynolds, is used for estimating Sh_0:

$$Sh_0 = \begin{cases} 2 + 0.6 {Re_m}^{1/2} {Sc_m}^{1/3}, & \text{if} \quad Re_m \leq 200 \\ 2 + 0.6 {Re_m}^{1/2} {Sc_m}^{1/3} + 0.02 {Re_m}^{0.8} {Sc_m}^{1/3}, & \text{if} \quad 200 < Re_m \leq 1500 \\ 2 + 0.000045 {Re_m}^{1.8}, & \text{if} \quad Re_m > 1500 \end{cases}, \tag{3.4}$$

where Sc is the Schmidt number and Re_m is the droplet Reynolds number:

$$Sc_m = \frac{\mu_m}{\rho_m D_{v,m}}, \tag{3.5}$$

$$Re_m = \frac{2\rho_g R_d |u_i - u_{d,k}|}{\mu_m}, \tag{3.6}$$

in which μ refers to the dynamic viscosity and $|u_i - u_{d,k}|$ represents the relative gas-droplet velocity, also known as slip velocity.

$$B_M = \frac{\sum_k Y_{v,k_s} - \sum_k Y_{v,k_g}}{1 - \sum_k Y_{v,k_s}}, \tag{3.7}$$

where Y_{v,k_s} and Y_{v,k_g} are the vapour mass fractions at the droplet surface and in the ambient gas far away from the droplet for each component k, respectively.

In the equilibrium state, the partial pressure of each component k at the droplet surface p_{v,k_s} can be determined by:

$$p_{v,k_s} = \gamma_i \chi_{l,k_s} {p^*}_{v,k}, \tag{3.8}$$

where χ_{l,k_s} is the molar fraction of the kth component in the liquid phase at the droplet surface, ${p^*}_{v,k}$ is the partial vapour pressure of the kth component in the absence of other components ($\chi_{l,k_s} = 1$), and γ_k is the activity coefficient. Assuming phase equilibrium at the droplet surface, ${p^*}_{v,k} = {p^{sat}}_{v,k}$. Additionally, assuming that a mixture of hydrocarbons, whose molecular structures are similar, form a nearly ideal solution, $\gamma_k \approx 1$ and Eq.(3.8) can be simplified to the Raoult's law:

$$p_{v,k_s} = \chi_{l,k_s} {p^*}_{v,k}. \tag{3.9}$$

In fact, according to Woodrow (2003), Eq. (3.9) is a reasonable assumption for the fuel vapour of a Jet A fuel mixture. Even though Jet A is a mixture of different hydrocarbons, the generally uniform chemical nature of its components contributes to the observed ideal behaviour.

The vapour molar fraction of each component k at the droplet surface χ_{v,k_s} is equal to

the ratio between its partial pressure and the ambient pressure p_g:

$$\chi_{v,k_s} = \frac{p_{v,k_s}}{p_g}. \tag{3.10}$$

Therefore, once χ_{v,k_s} is determined, Y_{v,k_s} can be computed as:

$$Y_{v,k_s} = \frac{\chi_{v,k_s} W_{v,k}}{\chi_{v,k_s} W_{v,k} + \chi_{g_s} W_g}, \tag{3.11}$$

where W is the molecular weight, and subscripts v and g refer to the fuel vapour and the ambient gas, respectively.

Concerning the gas-vapour mixture conditions in the film around the droplet, an averaging procedure may be used in order to determine the reference conditions to be used to estimate transport and thermodynamic properties. Hubbard, Denny and Mills (1975) and Yuen and Chen (1976) advise using the $1/3$ averaging rule, which is the empirical rule typically selected for spray combustion simulations. Hence, the reference conditions are given by:

$$T_m = T_s + \frac{1}{3}\left(T_g - T_s\right), \tag{3.12}$$

and

$$Y_{v,k_m} = Y_{v,k_s} + \frac{1}{3}\left(Y_{v,k_g} - Y_{v,k_s}\right). \tag{3.13}$$

3.1.2 Convective heating

Considering the energy balance equation in spherical coordinates, assuming Fourier's law of heat conduction, and supposing constant liquid density, constant liquid thermal conductivity, and constant liquid specific heat, spherical symmetry condition and null velocity inside the droplet ($u_R = u_\theta = u_\phi = 0$), the following equation describes the mathematical model for droplet heating:

$$\frac{\partial T}{\partial t} = \frac{k_l}{\rho_l c_{p_l}} \left(\frac{\partial^2 T}{\partial R^2} + \frac{2}{R} \frac{\partial T}{\partial R} \right), \tag{3.14}$$

where T stands for the droplet temperature, R is the radial coordinate, t represents time, c_p is the specific heat, and the subscript l refers to liquid. Note that assuming k_l, ρ_l and c_{pl} as constants is a valid approximation for a short time step.

This one-dimensional heat conduction equation, for $T(R,t)$, should be solved subject to the following initial condition:

$$T(R)|_{t=0} = T_0, \tag{3.15}$$

and the Robin boundary condition at the droplet surface:

$$h(T_{\text{eff}} - T_s) = k_l \left.\frac{\partial T}{\partial R}\right|_{R=R_d-0}, \tag{3.16}$$

where $T_{\text{eff}} = T_{\text{eff}}(t)$ is the effective temperature to take into account the effect of droplet evaporation instead of considering only the carrier gas temperature T_g, $T_s = T_s(t)$ is the droplet surface temperature at $R = R_d$, and h is the convection heat transfer coefficient.

$$T_{\text{eff}} = T_g + \frac{\dot{m}_d L_v}{4\pi R_d^2 h}, \tag{3.17}$$

and

$$h = \frac{Nu^*}{2}\frac{k_g}{R_d}, \tag{3.18}$$

in which Nu represents the Nusselt number.

$$Nu^* = Nu_m \frac{\ln(1.0 + B_T)}{B_T}, \tag{3.19}$$

where B_T is the Spalding thermal energy transfer number:

$$B_T = (1 + B_M)^{\varphi} - 1, \tag{3.20}$$

$$\varphi = \left(\frac{c_{p_v}}{c_{p_g}}\right)\left(\frac{Sh_m}{Nu_m}\right)\frac{1}{Le_m}, \tag{3.21}$$

where Le is the Lewis number:

$$Le_m = \frac{k_m}{c_{p_m} D_{v,m} \rho_m}, \tag{3.22}$$

and

$$Nu_m = 2 + \frac{Nu_0 - 2}{F_T}. \tag{3.23}$$

As for Sh_0, the same empirical correlation given by Eq. (3.4) can also be used for estimating Nu_0:

$$Nu_0 = \begin{cases} 2 + 0.6 {Re_m}^{1/2} {Pr_m}^{1/3}, & \text{if} \quad Re_m \leq 200 \\ 2 + 0.6 {Re_m}^{1/2} {Pr_m}^{1/3} + 0.02 {Re_m}^{0.8} {Pr_m}^{1/3}, & \text{if} \quad 200 < Re_m \leq 1500 \\ 2 + 0.000045 {Re_m}^{1.8}, & \text{if} \quad Re_m > 1500 \end{cases}, \tag{3.24}$$

where Pr is the Prandlt number:

$$Pr_m = \frac{\mu_m c_{p_m}}{k_m}, \tag{3.25}$$

and

$$F_T = (1 + B_T)^{0.7} \frac{\ln(1 + B_T)}{B_T}. \tag{3.26}$$

Assuming that h is constant, what is a reasonable hypothesis within a small time step, the

analytical solution of Eq. (3.14) is (SAZHIN, 2014):

$$T(r,t) = \frac{1}{r}\sum_{n=1}^{\infty}\left\{\left(I_n - \frac{\sin\lambda_n}{\lambda_n^2}\zeta\right)\frac{\exp\left(-\kappa\lambda_n^2 t\right)}{b_n} - \right. \\ \left. -\frac{\sin\lambda_n}{b_n\lambda_n^2}\int_0^t \frac{d\zeta(\tau)}{d\tau}\exp\left(-\kappa\lambda_n^2(t-\tau)\right)d\tau\right\}\sin(\lambda_n r) + T_{\text{eff}}, \tag{3.27}$$

where $r = R/R_d$ is the normalised radial coordinate from the droplet centre, λ_n are positive roots of the following equation arranged in ascending order:

$$\lambda\cos\lambda + j\sin\lambda = 0, \tag{3.28}$$

$$b_n = \frac{1}{2}\left(1 + \frac{j}{j^2+\lambda_n^2}\right), \tag{3.29}$$

$$I_n = \int_0^1 rT_0(r)\sin(\lambda_n r)\,dr, \tag{3.30}$$

where $T_0(r)$ is the initial temperature distribution inside the droplet or the distribution predicted at the previous time step,

$$\kappa = \frac{k_l}{c_{pl}\rho_l R_d^2}, \tag{3.31}$$

$$\zeta = \frac{hT_{\text{eff}}R_d}{k_l}, \tag{3.32}$$

and

$$j = \frac{hR_d}{k_l} - 1. \tag{3.33}$$

Proof of the convergence of the series of Eq. (3.27) and the details of its derivation using separation of variables and expansions in the Fourier series are given in Sazhin (2014). Furthermore, as declared by Rybdylova *et al.* (2016), the term

$$\frac{\sin\lambda_n}{b_n\lambda_n^2}\int_0^t \frac{d\zeta(\tau)}{d\tau}\exp\left(-\kappa\lambda_n^2(t-\tau)\right)d\tau$$

from Eq. (3.27) is negligibly small. Thus, Eq. (3.27) can be simplified to:

$$T(r,t)=\frac{1}{r}\sum_{n=1}^{\infty}\left\{\left(I_n-\frac{\sin\lambda_n}{\lambda_n^2}\zeta\right)\frac{\exp(-\kappa\lambda_n^2 t)}{b_n}\right\}\sin(\lambda_n r)+T_{\text{eff}}, \tag{3.34}$$

The analysis of energy exchange between the ambient gas and a stationary droplet can be simplified due to the fact that it is essentially one-dimensional in space. However, the same simplification cannot be considered when a moving droplet is considered. While in stagnant droplets the only energy transfer mechanism is conduction, in moving droplets both conduction and advection occur. Eq. (3.27), nevertheless, can still be used if k_l is replaced by the effective thermal conductivity k_{eff}. Abramzon and Sirignano (1989) proposed the following model to compute k_{eff}:

$$k_{\text{eff}}=\chi k_l, \tag{3.35}$$

where the coefficient χ is greater than 1 always and increases with the Peclet number Pe_l as:

$$\chi=1.86+0.86\ \tanh\left(2.225\log\frac{Pe_l}{30}\right), \tag{3.36}$$

in which the Peclet number represents the ratio between advective transport rate bulk flow and conduction transport rate in the liquid phase:

$$Pe_l=Re_l Pr_l \tag{3.37}$$

with

$$Re_l = \frac{2\rho_l R_d U_{\mathrm{s,max}}}{\mu_l}, \tag{3.38}$$

and

$$Pr_l = \frac{\mu_l c_{pl}}{k_l}, \tag{3.39}$$

where $U_{\mathrm{s,max}}$ is the maximum velocity at the droplet surface expressed as:

$$U_{\mathrm{s,max}} = \frac{1}{32}|u_i|\frac{\mu_g}{\mu_l}Re_d C_F, \tag{3.40}$$

where C_F the friction drag coefficient for an evaporating spherical droplet:

$$C_F = \frac{12.69{Re_d}^{2/3}}{1+B_M}. \tag{3.41}$$

Using the correction factor χ allows the transformation of the conduction coefficient k_l into a global convection coefficient k_{eff}, which considers both conduction and advection effects.

Solution (3.34) was incorporated into the numerical code and it is updated at each time step in the calculations. The results achieved with Eq. (3.34) were shown to be the same as the results achieved based on the numerical solution of the corresponding one-dimensional heat conduction equation inside a spherical droplet (SAZHIN, 2014).

3.1.3 Species diffusion

Considering the continuity equation for species in spherical coordinates, assuming Fick's law of binary diffusion, and supposing constant liquid density and constant liquid diffusion coefficient, spherical symmetry condition and null velocity inside the droplet ($u_R = u_\theta = u_\phi = 0$), the following equation describes the mathematical model for species transport of each component k:

$$\frac{\partial Y_{l,k}}{\partial t} = D_l\left(\frac{\partial^2 Y_{l,k}}{\partial R^2} + \frac{2}{R}\frac{\partial Y_{l,k}}{\partial R}\right), \tag{3.42}$$

where $Y_{l,k}$ represents the mass fraction of the kth species in the liquid phase and D_l is the liquid diffusivity coefficient of the mixture considering its k species. Note that assuming k_l, ρ_l and c_l as constants is a valid approximation for a short time step.

This equation, for $Y_{l,k}(R,t)$, should be solved subject to the following initial and boundary conditions:

$$Y_{l,k}(R)|_{t=0} = Y_{l,k0}, \tag{3.43}$$

and

$$D_l \left.\frac{\partial Y_{l,k}}{\partial R}\right|_{R=R_d} = \frac{\dot{m}_d}{4\pi\rho_l {R_d}^2}\left(Y_{l,ks} - \varepsilon_k\right), \tag{3.44}$$

where $Y_{l,ks} = Y_{l,ks}(t)$ describes the liquid mass fraction of the species k at the droplet surface and ε_k is fractional evaporation rate given by:

$$\varepsilon_k = \frac{Y_{v,ks}}{\sum\limits_i Y_{v,ks}}, \tag{3.45}$$

in which the subscript v indicates the vapour phase. Clearly, $\sum\limits_k \varepsilon_k = 1$.

The evaporation rate of each species k is:

$$\dot{m}_{d,k} = \varepsilon_k \dot{m}_d. \tag{3.46}$$

Assuming that R_d is constant, an approximation valid for a short time step, the analytical solution of Eq. (3.42) is (SAZHIN, 2014):

$$Y_{l,k}\left(r,t\right) = \varepsilon_k + \frac{1}{r}\left\{\exp\left[D_l\left(\frac{\lambda_0}{R_d}\right)^2 t\right]\left[q_{Y_0,k} - Q_{Y_0}\varepsilon_k\right]\sinh\left(\lambda_0 r\right) + + \right. \tag{3.47}$$

$$\left. + \sum_{n=1}^{\infty}\left[\exp\left[-D_l\left(\frac{\lambda_n}{R_d}\right)^2 t\right]\left[q_{Y_n,k} - Q_{Y_n}\varepsilon_k\right]\sin\left(\lambda_n r\right)\right]\right\}, \tag{3.48}$$

where λ_0 and λ_n for $n \geq 1$ are solutions to the equations:

$$\tanh\lambda = -\frac{\lambda}{h_{Y_0}} \quad \text{and} \quad \tan\lambda = -\frac{\lambda}{h_{Y_0}}. \tag{3.49}$$

$$h_{Y_0} = -\left(1 + \frac{\alpha_m R_d}{D_l}\right), \tag{3.50}$$

$$\alpha_m = \frac{|\dot{m}_d|}{4\pi\rho_l {R_d}^2}, \tag{3.51}$$

$$Q_{Y_n} = \begin{cases} -\frac{1}{\|\nu_{Y_0}\|^2}\frac{\left(1+h_{Y_0}\right)\sinh\lambda_0}{{\lambda_0}^2}, & \text{when} \quad n = 0, \\ \frac{1}{\|\nu_{Y_n}\|^2}\frac{\left(1+h_{Y_0}\right)\sin\lambda_n}{{\lambda_n}^2}, & \text{when} \quad n \geq 1, \end{cases} \tag{3.52}$$

$$q_{Y_n,k} = \frac{1}{\|\nu_{Y_n}\|^2}\int_0^1 r Y_{l,k_0}(r)\,\nu_{Y_n} dr, \quad \text{for} \quad n \geq 0, \tag{3.53}$$

$Y_{l,k_0}(r)$ are the initial species mass fraction distributions inside the droplet or the distributions predicted at the previous time step,

$$\nu_{Y_n} = \begin{cases} \sinh(\lambda_0 r), & \text{when} \quad n = 0, \\ \sin(\lambda_n r), & \text{when} \quad n \geq 1, \end{cases} \tag{3.54}$$

$$\|\nu_{Y_n}\|^2 = \begin{cases} -\frac{1}{2}\left[1 + \frac{h_{Y_0}}{{h_{Y_0}}^2 - {\lambda_0}^2}\right], & \text{when} \quad n = 0, \\ \frac{1}{2}\left[1 + \frac{h_{Y_0}}{{h_{Y_0}}^2 + {\lambda_n}^2}\right], & \text{when} \quad n \geq 1. \end{cases} \tag{3.55}$$

Proof of the convergence of the series of Eq. (3.47) and the details of its derivation using

separation of variables and expansions in the Fourier series are given in Sazhin (2014).

In the case of moving droplets, the mass fractions distributions can be still described by Eq. (3.47), but with D_l replaced by the effective diffusivity D_{eff} defined as:

$$D_{\text{eff}} = \chi D_l, \tag{3.56}$$

where

$$\chi = 1.86 + 0.86 \tanh\left(2.225 \log \frac{Pe_l}{30}\right), \tag{3.57}$$

in which the Peclet number represents the ratio between advective and diffusive mass transport rate in the liquid phase and it is calculated by:

$$Pe_l = Re_l Sc_l, \tag{3.58}$$

with

$$Sc_l = \frac{\mu_l}{\rho_l D_l}. \tag{3.59}$$

and Re_l computed as presented in Eq. (3.38). The idea when using the correction factor χ is transforming the diffusion coefficient D_l into a global convection coefficient D_{eff}, which considers both diffusion and advection effects.

As in the case of Solution (3.34), Solution (3.47) was incorporated into the numerical code and was used at each time step in the calculations. The results achieved with Eq. (3.47) were shown to be the same as the results achieved based on the numerical solution of the corresponding one-dimensional species diffusion equation inside a spherical droplet (SAZHIN, 2014).

Both analytical solutions for temperature and species mass fraction were obtained assuming that droplet radius is constant, which is justified for sufficiently short time steps, assuming that the surface regression rate is much smaller than the transport rate in the liquid (LAW; SIRIGNANO, 1977). In the results presented the in this chapter, the model is only applied to isolated stationary droplets. However, its generalisation to moving droplets, using the Effective

Thermal Conductivity-Effective Diffusivity (ETC-ED) models, is used is the simulations presented in Chapter 5.

3.2 Numerical and computational details

The model described in the previous section was implemented into in-house code MFSim. All calculations presented in this chapter were performed using an Intel(R) Core(TM) i7-3612QM CPU @ 2.10 GHz processor with a 100 MHz clock.

In what follows, the main steps of the numerical algorithm are summarised.

Algorithm 1 Multicomponent droplet heating and evaporation

1: Initially, distributions of temperature and mass fractions of species inside the droplet are assumed uniform, and the initial molar fractions of species presented in Table 3.1 are adopted. For the subsequent time steps, the distributions obtained in the previous time step are used.
2: Calculation of the species partial pressures at the droplet surface using the supplementary data and Eq. (3.9).
3: Calculation of the species evaporation rates using the supplementary data and Eq. (3.64).
4: Determination of the reference conditions of the gas-vapour mixture.
5: Calculation of the mixture properties μ_m, ρ_m, $D_{v,m}$, k_m and c_{p_m} using the Cantera database.
6: Calculation of the gas properties ρ_g, μ_g and k_g using the Cantera database.
7: Calculation of the fuel vapour property c_{p_v} using the Cantera database.
8: Calculation of the liquid properties ρ_l, c_l, k_l, μ_l and D_l using the expressions in the supplementary data and the equations presented in Section 3.4.
9: Calculation of the dimensionless numbers, the total evaporation rate and the contribution of each component.
10: Calculation of the effective temperature, κ and ζ using Eqs. (3.17) and (3.31).
11: Calculation of the distribution of temperature inside the droplet based on Eq. (3.34). The roots of Eq. (3.28) are found using the bisection method (KIUSALAAS, 2013).
12: Calculation of the droplet average temperature using Simpson's method (KIUSALAAS, 2013).
13: Calculation of the distribution of species inside the droplet based on Eq. (3.47). The roots of Eq. (3.49) are found using the bisection method (KIUSALAAS, 2013).
14: Calculation of the droplet average composition using Simpson's method (KIUSALAAS, 2013).
15: Update ρ_l based on the change in droplet average temperature and average composition.

16: Update the droplet diameter using the 4th-order Runge-Kutta scheme (KIUSALAAS, 2013) and taking into account both its evaporation and thermal swelling.

17: Return to Step 1 and repeat all steps for the next time step.

3.3 Compositions of Jet A and surrogates

The composition of Jet A, taken from Vozka *et al.* (2019), is presented in Fig. 3.1 and Table 3.1. The analysis performed by Vozka *et al.* (2019) was based on 'two-dimensional gas chromatography a with flame ionization detector'. Altogether, 61 components were identified, which were split into 7 hydrocarbon groups. The detailed description of the 61 components is hereafter referred to as the 'complete composition'.

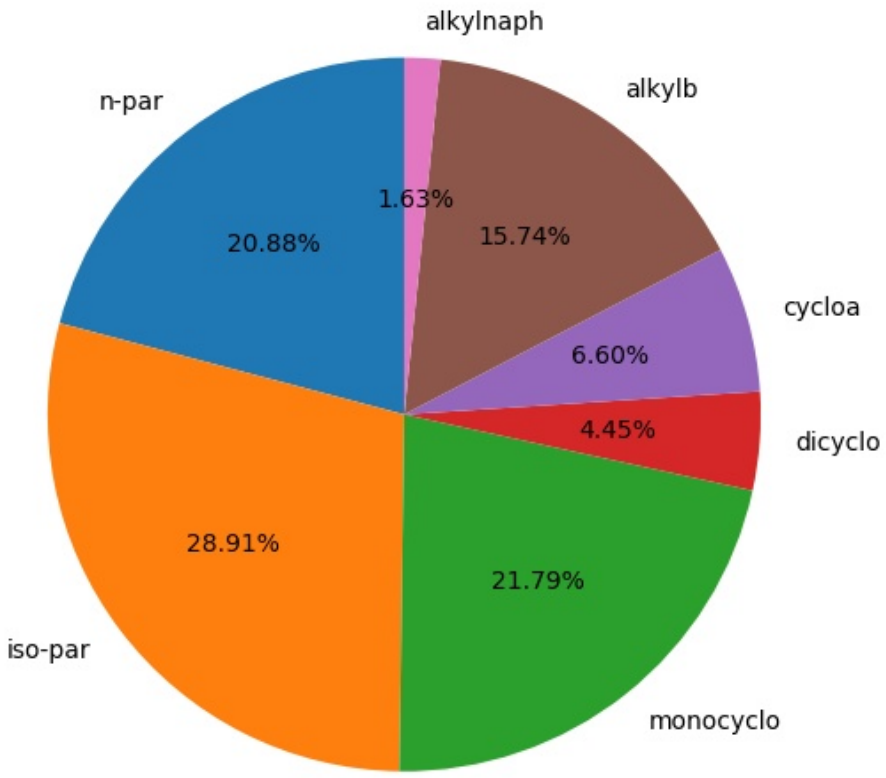

Figure 3.1: A schematic presentation of the composition of Jet A in terms of the molar fractions presented in Table 3.1.

To the best of the authors' knowledge, the first attempt to investigate heating and evaporation characteristics of kerosene surrogate droplets, using the model described in Section 3.1,

Table 3.1: Molar fractions of the components of Jet A. C_n stands for carbon number, n-par for n-paraffins, iso-par for iso-paraffins, monocyclo for monocycloparaffins, dicyclo for dicycloparaffins, alkyb for alkylbenzenes, cycloa for cycloaromatics, alkylnaph for alkylnaphthalenes.

C_n	n-par	iso-par	monocyclo	dicyclo	alkyb	cycloa	alkylnaph
C_7	0	0	0.0034	0	0	0	0
C_8	0.0109	0.0037	0.0500	0.0031	0.0010	0	0
C_9	0.0590	0.0581	0.0531	0.0094	0.0223	0.0018	0
C_{10}	0.0523	0.0731	0.0438	0.0110	0.0543	0.0088	0.0013
C_{11}	0.0322	0.0514	0.0277	0.0105	0.0331	0.0177	0.0043
C_{12}	0.0209	0.0325	0.0200	0.0072	0.0199	0.0210	0.0061
C_{13}	0.0154	0.0285	0.0137	0.0022	0.0146	0.0108	0.0038
C_{14}	0.0096	0.0199	0.0053	0.0011	0.0082	0.0058	0.0007
C_{15}	0.0054	0.0139	0.0009	0	0.0026	0.0001	0.0001
C_{16}	0.0024	0.0062	0	0	0.0013	0	0
C_{17}	0.0006	0.0014	0	0	0.0001	0	0
C_{18}	0.0001	0.0004	0	0	0	0	0

was undertaken in Poulton *et al.* (2020). The authors of that paper compared thirteen surrogates without making a distinction between standard kerosene and Jet A surrogates. For the present analysis, twelve Jet A surrogates developed over the last decade, between 2010 and 2019, were selected, without any overlap with surrogates considered in Poulton *et al.* (2020). This aspect makes the present research a complementary study to the one conducted in Poulton *et al.* (2020).

Table 3.2: Jet A surrogates selected for the present analysis, their brief description, the numbers of components in them, and the references to the papers in which they were first described.

Surrogates	Description	N Comp	References
1	Dooley's 1st generation	3	Dooley *et al.* (2010)
2	Huber's surrogate	8	Huber, Lemmon and Bruno (2010)
3	Dooley's 2nd generation	4	Dooley *et al.* (2012)
4	Kim's UM1	4	Kim, Martz and Violi (2014)
5	Kim's UM2	4	Kim, Martz and Violi (2014)
6	Improved Dooley's 1st gen.	3	Yu, Ju and Gou (2016)
7	Improved Dooley's 2nd gen.	4	Yu, Ju and Gou (2016)
8	Won's 1st surrogate	3	Won *et al.* (2017)
9	Won's 2nd surrogate	3	Won *et al.* (2017)
10	Won's 3rd surrogate	4	Won *et al.* (2017)
11	Won's 4th surrogate	9	Won *et al.* (2017)
12	Jameel's surrogate	2	Abdul-Jameel *et al.* (2019)

The twelve previously developed surrogates used in the present analysis are listed in Table 3.2. As can be seen from this table, the number of components in these surrogates varies between two and nine, which is expected to lead to a significant reduction in CPU requirements for the calculation of droplet heating and evaporation compared with that for Jet A droplets containing 61 components (VOZKA *et al.*, 2019).

In all cases, the selection of surrogates was based mainly on the similarity between the key properties of the surrogates and Jet A. There was specific justification, however, for the selection of each surrogate. The components of Surrogate 1, called Dooley's 1st generation surrogate, were selected based on several combustion related properties, including cetane number, ratio of the numbers of hydrogen and carbon atoms, sooting propensity and average molecular weight. The selection of the components of Surrogate 2, on the other hand, focused on thermophysical properties, such as density, viscosity, thermal conductivity, and volatility. Surrogate 3 is known as Dooley's 2nd generation surrogate. Even though its formulation is based on the same target properties of Surrogate 2, it prioritises emulation of the average molecular weight, as both physical properties and combustion kinetic phenomena are highly influenced by the molecular structure.

The selection of components of Surrogates 4 and 5 was based on the same target criteria, including cetane number, net calorific value, hydrogen to carbon ratio, average molecular weight, density, viscosity, surface tension, and distillation curve, but with different weights for each criterion. Surrogate 4 reproduces better temperature-independent properties, i.e. the first four target criteria from the ones listed above, while Surrogate 5 was shown to better emulate liquid density and volatility. Surrogates 6 and 7 are generally referred to as improved versions of Surrogates 1 and 3, respectively, the Dooley's surrogates, as they were developed based on a new surrogate formulation method. The novelty of this method lies in constructing surrogates by directly matching molecular structures and key functional groups instead of using combustion parameters explicitly.

The selection of Surrogates 8 to 11 was based on statistical analysis of the relation between each chemical functional group and a specific combustion property of the fuel. Although the combustion behaviour of the four surrogates is similar, their physical properties show considerable variation. This is particularly visible in the case of the distillation characteristics, which dictate preferential evaporation effects. Finally, Surrogate 12 was designed using a 'minimalist functional

group approach', which focuses on matching fundamental molecular parameters rather than broad molecular classes. Also, this new surrogate formulation method limited the number of components to two.

Table 3.3: The components used in the Jet A surrogates, their chemical formulae, names and Chemical Abstracts Service (CAS) numbers.

Comps	Formulae	Names	CAS numbers
1	C_8H_{18}	n-octane	111-65-9
2	$C_{10}H_{22}$	n-decane	124-18-5
3	$C_{12}H_{26}$	n-dodecane	112-40-3
4	$C_{14}H_{30}$	n-tetradecane	629-59-4
5	$C_{16}H_{34}$	n-hexadecane	544-76-3
6	C_7H_{16}	iso-heptane	591-76-4
7	C_8H_{18}	iso-octane	592-27-8
8	$C_{12}H_{26}$	iso-dodecane	7045-71-8
9	$C_{16}H_{34}$	iso-cetane	1560-93-6
10	C_7H_{14}	methylcyclohexane	108-87-2
11	$C_{13}H_{26}$	heptylcyclohexane	5617-41-4
12	$C_{10}H_{18}$	decalin	493-02-7
13	$C_{11}H_{20}$	1-methyldecalin	-
14	$C_{11}H_{20}$	2-methyldecalin	4683-94-7
15	$C_{11}H_{20}$	5-methyldecalin	2547-27-5
16	C_7H_8	toluene	108-88-3
17	C_8H_{10}	o-xylene	95-47-6
18	C_9H_{12}	propylbenzene	103-65-1
19	C_9H_{12}	1,3,5-trimethylbenzene	108-67-8
20	$C_{13}H_{20}$	heptylbenzene	1078-71-3
21	$C_{10}H_{12}$	tetralin	119-64-2

The chemical formulae of the components used in surrogates, their names and Chemical Abstracts Service (CAS) numbers are presented in Table 3.3. Note that the CAS number for 1-methyldecalin is not available. Molar fractions of the components in the surrogates are presented in Table 3.4. Data provided in Table 3.4 are used for the analysis of surrogate droplet heating and evaporation.

3.4 Thermodynamic and transport properties of the components

The transport and thermodynamic properties of fuel vapour and ambient gas, including density, dynamic viscosity, thermal conductivity, specific heat capacity, and binary diffusion coefficient, are obtained from the open source Cantera software package (GOODWIN; MOFFAT;

Table 3.4: Molar fractions of the components used in each Jet A surrogate (in per cent).

	Surrogates											
Comps	1	2	3	4	5	6	7	8	9	10	11	12
1	-	-	-	-	-	-	-	-	-	-	2.30	-
2	42.67	-	-	-	-	54.71	-	-	-	-	5.00	-
3	-	-	40.40	38.44	28.97	-	48.57	49.00	-	31.20	29.90	-
4	-	5.70	-	-	-	-	-	-	-	-	10.00	-
5	-	3.30	-	-	-	-	-	-	36.50	12.30	1.40	-
6	-	-	-	-	-	-	-	-	-	-	-	69.10
7	33.02	-	29.50	-	-	20.75	22.86	21.00	31.00	-	3.40	-
8	-	-	-	-	-	-	-	-	-	24.30	14.30	-
9	-	-	-	14.84	14.24	-	-	-	-	-	-	-
10	-	-	-	23.36	-	-	-	-	-	-	-	-
11	-	27.9	-	-	-	-	-	-	-	-	-	-
12	-	-	-	-	31.88	-	-	-	-	-	-	-
13	-	1.30	-	-	-	-	-	-	-	-	-	-
14	-	15.40	-	-	-	-	-	-	-	-	-	-
15	-	16.50	-	-	-	-	-	-	-	-	-	-
16	24.31	-	-	23.36	24.91	24.54	-	-	-	-	5.20	-
17	-	7.10	-	-	-	-	-	-	-	-	-	-
18	-	-	22.80	-	-	-	23.81	-	-	-	-	-
19	-	-	7.30	-	-	-	4.76	30.00	32.50	32.20	28.50	-
20	-	-	-	-	-	-	-	-	-	-	-	30.90
21	-	22.80	-	-	-	-	-	-	-	-	-	-

SPETH, 2016; SANJOSÉ, 2009). All properties are mixture averaged based on molar composition. The Cantera input file that provides information for each component is provided in the supplementary data. The transport and thermodynamic properties of liquid hydrocarbons, including density, dynamic viscosity, thermal conductivity, and specific heat capacity, alongside latent heat of evaporation, saturated vapour pressure, critical temperature, and pressure, are inferred from the databases in Yaws' books (YAWS, 2003; YAWS, 2008; YAWS, 2009). These properties for the Jet A liquid components are calculated at the average temperature inside the droplets, while latent heat of evaporation and saturated vapour pressure are calculated at the droplet surface temperature. The approximations inferred from Yaws (2003), Yaws (2008), Yaws (2009) and used in the present analysis are presented in the supplementary data.

The Wilke-Chang approximation for the liquid species diffusion coefficient is used (BIRD; LIGHTFOOT; STEWART, 2002):

$$D_{l,k} = \frac{7.4 \times 10^{-15} \sqrt{M_l} T}{\mu_l {V_{l,k}}^{0.6}}, \tag{3.60}$$

where M_l is average molar mass of the liquid mixture:

$$M_l = \left[\sum_k \left(\frac{Y_{l,k}}{M_{l,k}} \right) \right]^{-1}, \tag{3.61}$$

$$V_{l,k} = \left(\frac{\sigma_{l,k}}{1.18} \right)^3, \tag{3.62}$$

$\sigma_{l,k}$ is the Lennard-Jones length for the ith component, in Å (SILVA; LIU; MACEDO, 1998):

$$\sigma_{l,k} = 0.17791 + 11.779 \left(\frac{T_{\mathrm{cr},k}}{p_{\mathrm{cr},k}} \right) - 0.049029 \left(\frac{T_{\mathrm{cr},k}}{p_{\mathrm{cr},k}} \right)^2, \tag{3.63}$$

critical temperatures $T_{\mathrm{cr},k}$ and critical pressures $p_{\mathrm{cr},k}$ of the components are in K and bar, respectively.

The properties of the mixtures were estimated as (SAZHIN *et al.*, 2014):

$$L_v = \sum_k \left(\varepsilon_i L_i \right), \tag{3.64}$$

$$p_{vs} = \sum_k \left(\chi_{l,k} p_{v,k_s} \right), \tag{3.65}$$

$$\rho_l = \left[\sum_k \left(\frac{Y_{l,k}}{\rho_{l,k}} \right) \right]^{-1}, \tag{3.66}$$

$$\ln \mu_l = \sum_k \left(\chi_{l,k} \ln \mu_{l,k} \right), \tag{3.67}$$

$$k_l = \left[\sum_k \left(\frac{Y_{l,k}}{{k_{l,k}}^2} \right) \right]^{-1/2}, \tag{3.68}$$

$$c_l = \sum_k \left(Y_{l,k} c_{l,k} \right), \tag{3.69}$$

$$D_l = \sum_k \left(\chi_{l,k} D_{l,k} \right). \tag{3.70}$$

The thermodynamic and transport properties are assumed constant during each time step, but they vary from one time step to another due to the changes in temperature and composition.

3.5 Results and discussion

3.5.1 Modelling versus experimental data

To validate the predictions of the model described in Section 3.1 the experimental data for aviation kerosene (Jet A) provided in Wang *et al.* (2018) is used. The main reason for selecting this paper is its focus on aviation kerosene; it shows that aviation kerosene droplets evaporate more slowly than common kerosene ones. In contrast, previous experimental studies have focused upon common kerosene droplet heating and evaporation (e.g. (GHASSEMI; BAEK; KHAN, 2006), (KHAN; BAEK; LEE, 2007), (JAVED *et al.*, 2013), (YOON; BAEK, 2015)).

The experiment described in Wang *et al.* (2018) was performed in a heated furnace in which the droplet was suspended from a nickel-chromium alloy wire of 200 μm diameter. The initial droplet temperature was the room temperature, assumed to be equal to 298 K, and the initial droplet diameter was 1.38 mm. The ambient pressure was atmospheric, assumed to be equal to 0.1 MPa, and the furnace temperature was monitored by a thermocouple and maintained at 573 K. Both the droplet and the ambient air were quiescent.

In the present study, the droplet volume was discretised into 500 concentric layers to calcu-

late the integrals in Solutions (3.34) and (3.47), whereas time steps of 1×10^{-5} s were considered. 200 eigenvalues were used to calculate the temperature distribution and 100 eigenvalues were used to calculate the species mass fraction distributions. The roots of the equation for eigenvalues were found using the bisection method with accuracy of 1×10^{-12}. The results of sensitivity analysis based on the choice of these parameters are presented in the next section.

As follows from Table 1 of Rybdylova *et al.* (2016), when the number of layers used in calculations is less than 50, the predictions of the model are dependent upon that number, but they do not change when the number of layers is between 50 and 500. Since the conditions of the present simulations are not the same as in the setup analysed in Rybdylova *et al.* (2016), 500 layers are used in the present analysis to mitigate this effect. As can be seen in Figure 4 of Rybdylova *et al.* (2018), using 10 eigenvalues leads to unacceptably large errors when predicting the values of mass fractions of the components near the centre and the surface of the droplets, whilst using 40 eigenvalues led to reasonably accurate predictions of these mass fractions within the whole volume of the droplet. This justifies the decision to use 50 eigenvalues in the present analysis. A discussion on computational cost and a further investigation of how the numerical parameters influence the results are presented in Section 3.5.3 (see Table 3.5).

Fig. 3.2 shows a comparison of the normalised squared droplet diameter $versus$ time obtained from the numerical simulations and the experimental data, while Fig. 3.3 presents plots of temperature at the droplet surface and at its centre, as well as the average temperature predicted by the numerical simulations.

As follows from Fig. 3.2, the results of simulations agree reasonably well with experimental data, giving confidence in the present modelling approach. In agreement with experimental data, the simulations show initial thermal swelling, which is followed by a steady evaporation period. Although a Jet A droplet contains a mixture of many components, its evaporation characteristics can be well approximated by the D^2 law. Fig. 3.3 shows that, at the beginning of the droplet heating and evaporation process, the droplet surface temperature increases more quickly than the droplet average and centre temperatures. Then follows a rather long 'plateau' period when the values of these temperatures coincide and there is almost no change over time. This 'plateau' corresponds to the D^2 law for droplet evaporation clearly seen in Fig. 3.2. At the very end of the droplet evaporation period, an oscillatory increase in all three temperatures was identified. The

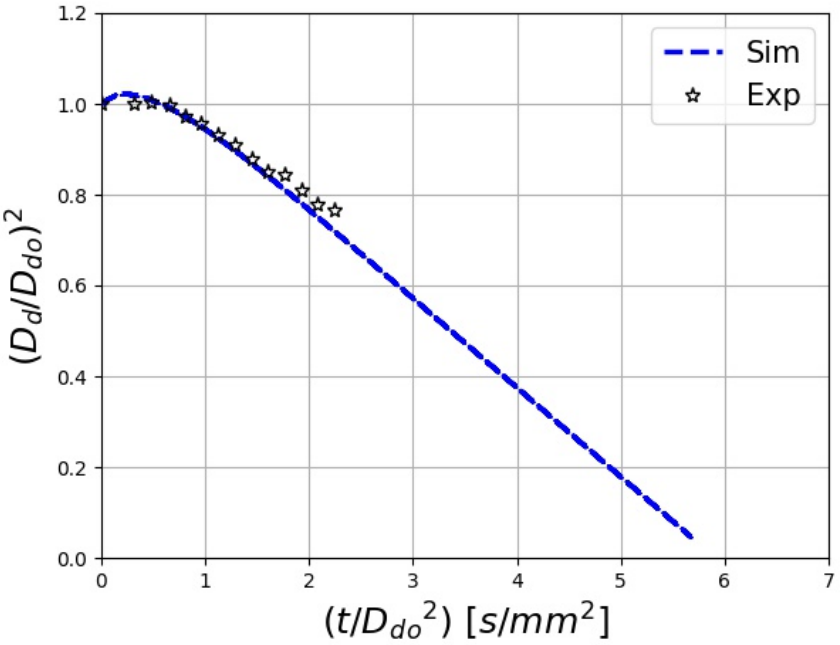

Figure 3.2: Normalised squared droplet diameter *versus* time predicted by the present simulation (dashes) and the results of measurements performed by Wang *et al.* (2018) (stars).

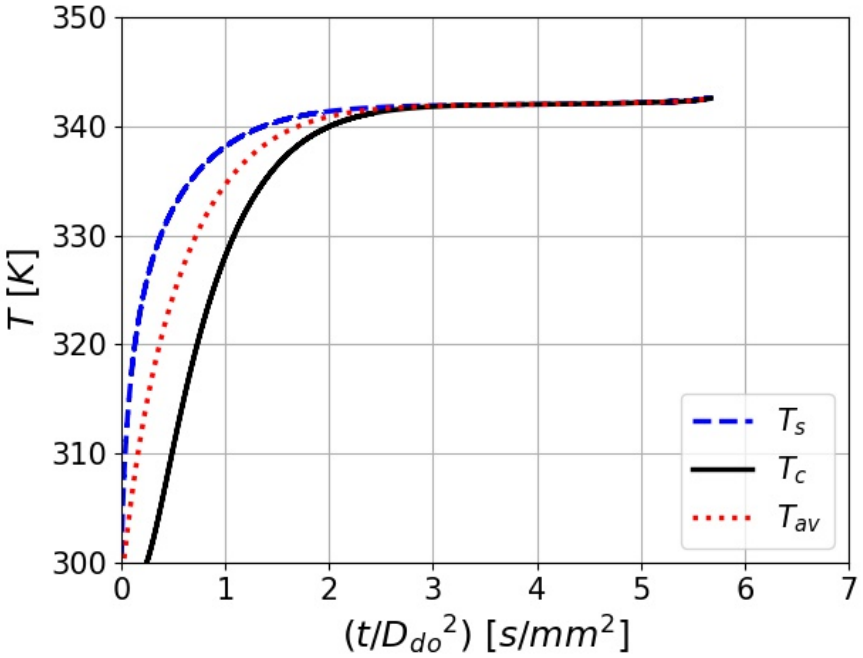

Figure 3.3: Droplet surface, centre and average temperatures *versus* time predicted by the present simulation.

model predictions at this stage, however, are not expected to be reliable due to the very small size of the droplet. Therefore, this oscillatory behaviour, which is non-physical, is not presented in Fig. 3.3.

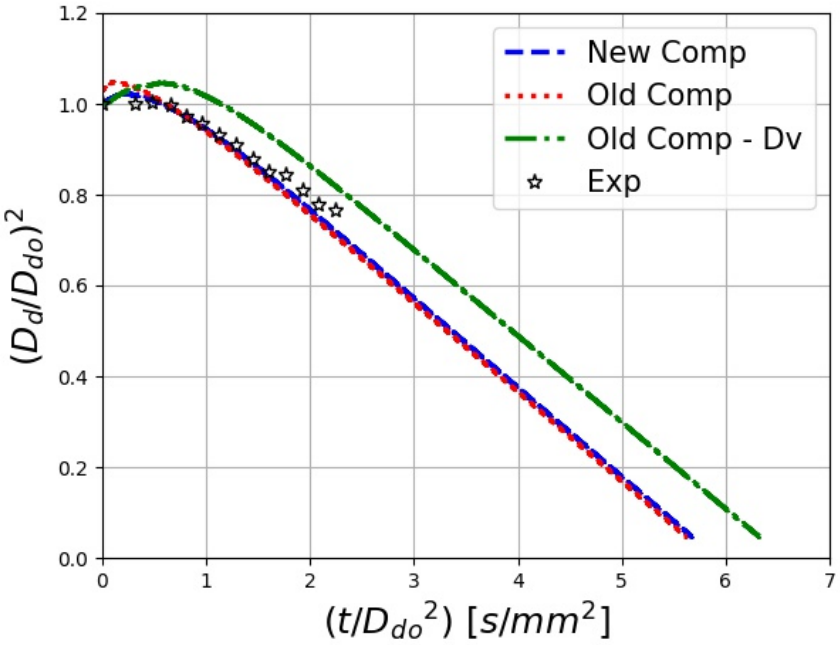

Figure 3.4: Normalised squared droplet diameter *versus* time predicted by the simulations (dashed curves) and the results of measurements performed by Wang *et al.* (2018) (stars). 'New comp' refers to Jet A composition from Vozka *et al.* (2019) presented in Table 3.1, 'Old comp' refers to kerosene composition from Lissitsyna *et al.* (2014), which is used in Poulton *et al.* (2020), and 'Old comp - Dv' refers to the case when the cycloundecane approximation for the vapour diffusion coefficient was used.

Fig. 3.4 shows a comparison between the normalised squared droplet diameter *versus* time predicted using several modelling approaches and the experimental data, while Fig. 3.5 shows the droplet average temperature *versus* time predicted by these modelling approaches. In both figures, the term 'New comp' refers to the simulation results when the Jet A composition presented in Table 3.1 is used. The kerosene composition analysed by Lissitsyna *et al.* (2014), previously used by Poulton *et al.* (2020) and identified as 'Old comp', is also shown here in order to demonstrate the effect of using different kerosene compositions. Additionally, the assumption made by Poulton *et al.* (2020), that the vapour diffusion coefficient can be approximated by cycloundecane, is tested to understand how it would affect the results. The results obtained taking this approximation into account are referred to in the plots as 'Old comp - Dv'.

As can be seen in Fig. 3.4, using the composition from Lissitsyna *et al.* (2014) also delivers a good agreement with the experimental data. At the same time, one can see from this figure that the assumption that the vapour diffusion coefficient can be approximated by that of cycloundecane may not be the best choice, as in this case droplet diameter predictions clearly deviate from the

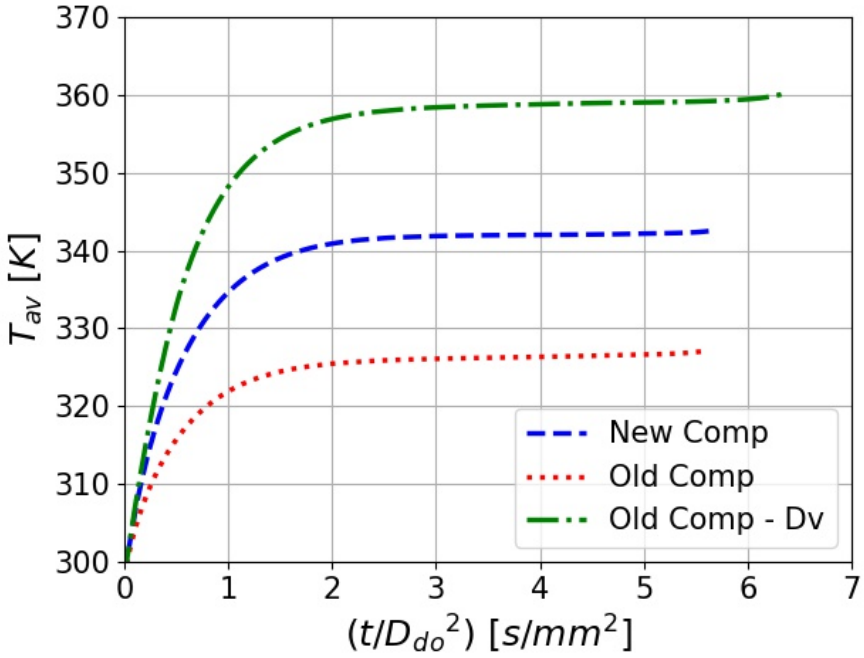

Figure 3.5: Droplet average temperature *versus* time for the same cases as presented in Figure 3.4. 'New comp' refers to Jet A composition from Vozka *et al.* (2019) presented in Table 3.1, 'Old comp' refers to kerosene composition from Lissitsyna *et al.* (2014), which is used in Poulton *et al.* (2020), and 'Old comp - Dv' refers to the case when the cycloundecane approximation for the vapour diffusion coefficient was used.

experimental measurements. Note that Poulton *et al.* (2020) used experimental measurements of common kerosene evaporation extracted from Javed *et al.* (2013) to validate the simulations performed for the composition described by Lissitsyna *et al.* (2014) for aviation kerosene.

3.5.2 Analysis of surrogates

Droplet evaporation behaviours using the Jet A complete composition from Table 3.1 and surrogates from Table 3.4 are compared using the same boundary and initial conditions as in Section 3.5.1, $T_{d_0} = 298$ K, $D_{d_0} = 1.38$ mm, $p_g = 0.1$ MPa, and $T_g = 573$ K. These parameters are the same as the ones used in the experiment described in Wang *et al.* (2018). Figure 3.6 shows a comparison of the normalised squared droplet diameters and the droplet average temperature versus time inferred from the numerical simulations.

The results for the twelve surrogates are presented in three groups of plots. Surrogates 1, 6, 3 and 7 are grouped together since they are Dooley's 1st and 2nd generation surrogates; Surrogates 1 and 3 are the original ones and 6 and 7 are the improved ones. Surrogates 8, 9, 10 and 11 were all formulated by Won *et al.* (2017) using the same statistical methodology based on

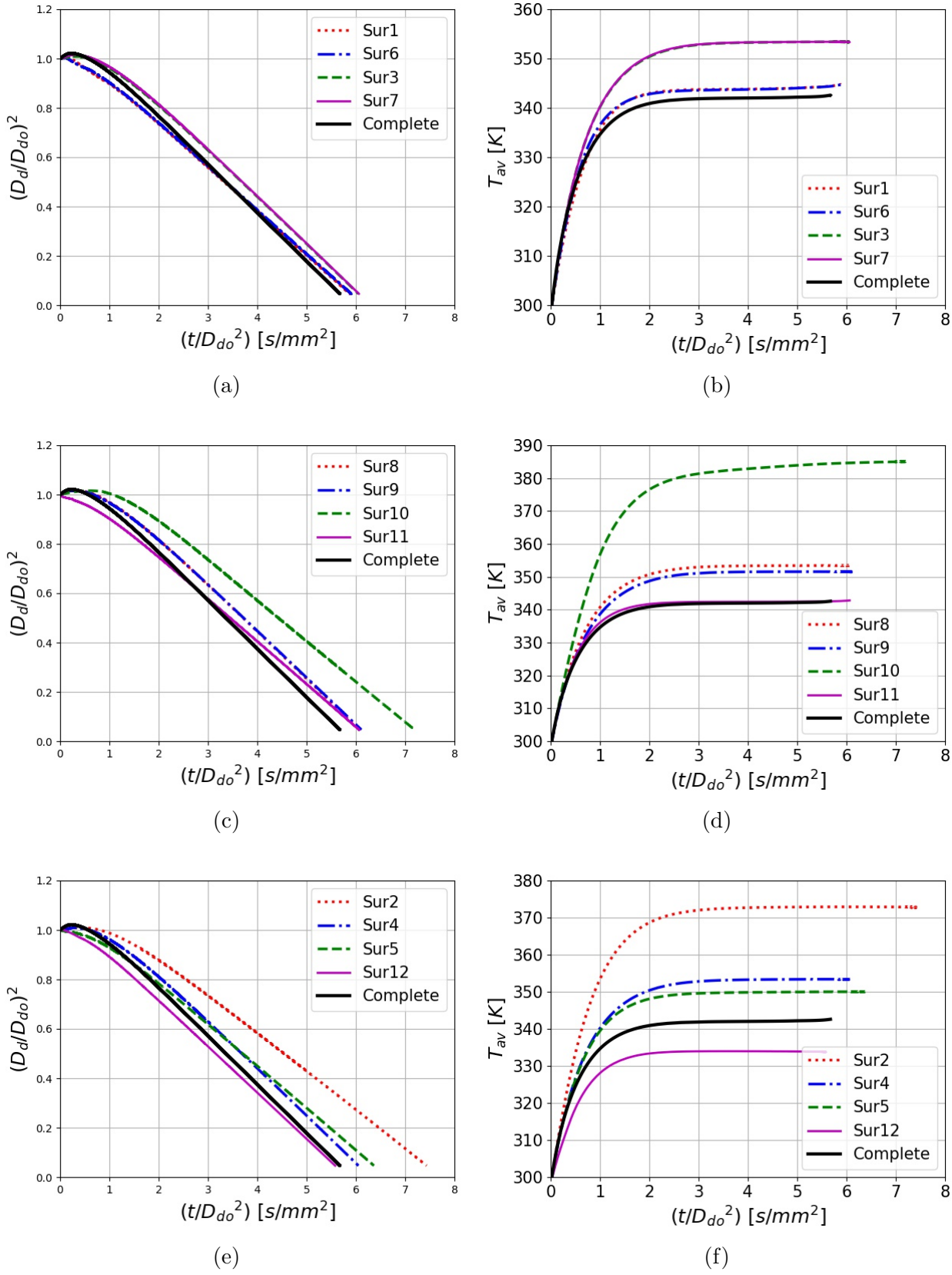

Figure 3.6: Normalised squared droplet diameter *versus* time (a, c, e) and droplet average temperature *versus* time (b, d, f) for droplets of complete composition and surrogates.

chemical functional groups. The remaining Surrogates 2, 4, 5 and 12 are presented in the final pair of plots.

Plots of relative deviations between the evaporation times for the cases when the complete Jet A composition and surrogates were used (ϕ_t) are shown in Fig. 3.7. ϕ_t was estimated as:

$$\phi_t = \frac{t_{\text{evap,complete}} - t_{\text{evap,surrogate}}}{t_{\text{evap,complete}}} \times 100\%. \tag{3.71}$$

The values of $t_{\text{evap,complete}}$ and $t_{\text{evap,surrogate}}$ were estimated at the time instants when droplet volumes reached 10% of their initial values.

For Surrogates 1 to 11 evaporation times are longer than that calculated for the complete Jet A composition. For Surrogate 12, on the other hand, the evaporation time is 1.7% shorter than that calculated for the complete Jet A composition. For this surrogate, the absolute value of ϕ_t is the smallest. Even though Surrogate 2 focuses on thermophysical properties, the results of calculations for this surrogate show the biggest deviation for evaporation time, with a droplet lifetime 30.6% longer than that predicted for a droplet with the complete fuel composition. This happens because this surrogate was developed prioritising components with higher boiling points. The droplets of Surrogate 10 are predicted to take 26.5% longer to evaporate than those with the complete fuel composition. Although this surrogate is specifically intended to emulate the Jet A distillation curve, is also designed to replicate the Jet A molecular weight, and this adversely affects its performance. The models using Surrogates 2 and 10 tend to predict higher equilibrium temperatures, as seen in Fig. 3.6, due to the significant presence of species with higher boiling temperatures in their composition. Even though the droplet is heated to a higher temperature, the less volatile components take longer to completely evaporate.

When the well-known D^2 law is followed, as observed for Jet A droplet evaporation, the droplet surface area decreases linearly with time. The average area reduction rate, known as the evaporation constant K, can be estimated as a slope of the variation of the squared droplet diameter. Relative average area reduction rate for droplets of complete composition and surrogates was estimated as:

$$\phi_K = \frac{K_{\text{complete}} - K_{\text{surrogate}}}{K_{\text{complete}}} \times 100\%. \tag{3.72}$$

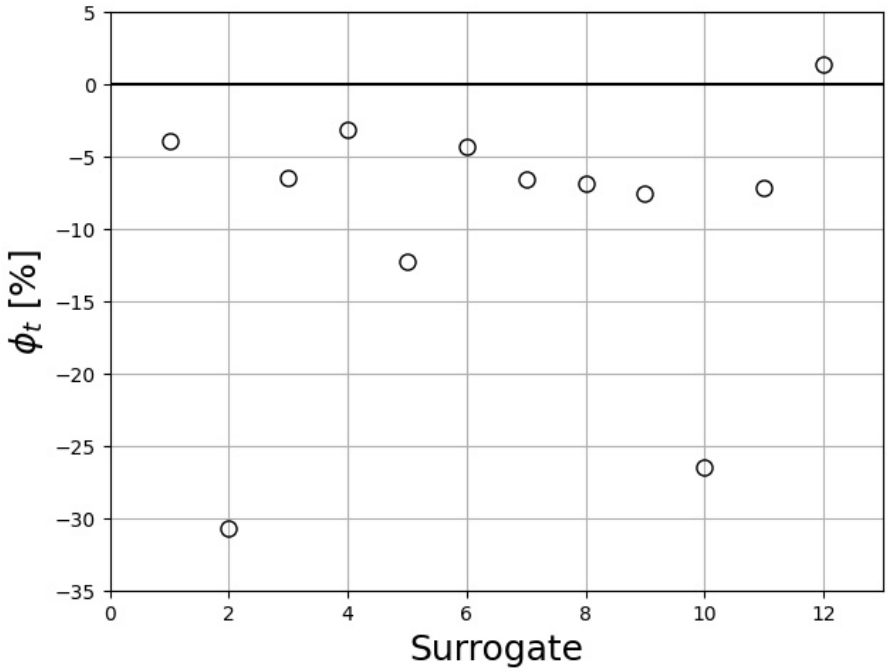

Figure 3.7: Relative evaporation time *versus* surrogate numbers.

The results are shown in Fig. 3.8. The values of K_{complete} and $K_{\text{surrogate}}$ for each surrogate were calculated from the data presented in Fig. 3.6. The best-fit straight lines used to estimate K were found using least squares regression.

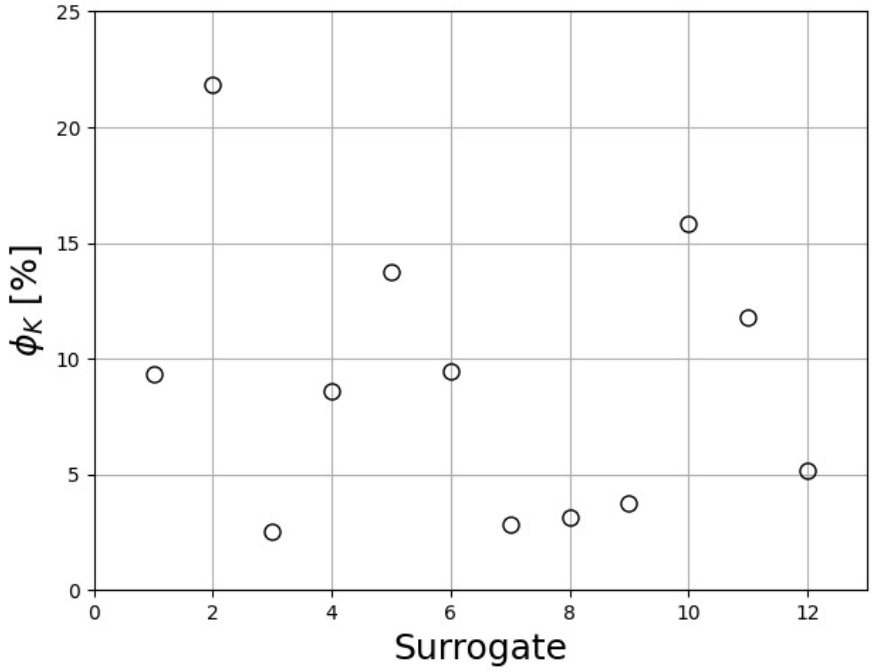

Figure 3.8: Relative average area reduction rate *versus* surrogate numbers.

For all surrogates the predicted droplet evaporation rates are lower than that of a droplet

with complete fuel composition. For Surrogates 3 and 7, which are both Dooley's 2nd generation surrogates, these deviations are the smallest, at 2.5% and 2.7%, respectively. The highest deviations are observed for Surrogates 2 and 10, at 21.8% and 15.9%, respectively. These trends are similar to those which follow from the analysis of evaporation times.

Relative differences between the maximal values of average droplet temperatures calculated for complete fuel composition and surrogates are estimated as:

$$\phi_T = \frac{\phi T_{\text{complete}} - \phi T_{\text{surrogate}}}{\phi T_{\text{complete}}} \times 100\%, \tag{3.73}$$

$$\phi T = T_{\text{av,max}} - T_0, \tag{3.74}$$

where T_0 are the initial droplet temperatures, which were the same for all droplets, at 298 K. The plots of ϕ_T *versus* surrogate number are shown in Fig. 3.9. The values of maximum average temperatures $T_{\text{av,max}}$ for complete fuel composition and surrogates were obtained during the last time steps of the calculations.

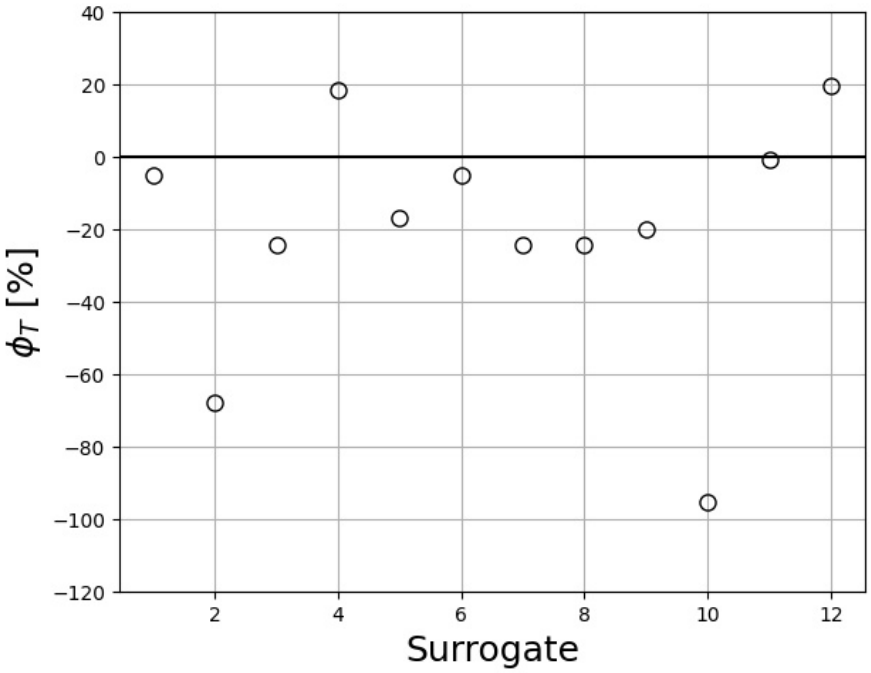

Figure 3.9: Relative temperature variation *versus* surrogate numbers.

As follows from Fig. 3.9, the highest absolute values of ϕ_T are predicted for Surrogates

2 and 10, which is consistent with the earlier results for droplet lifetimes and evaporation rates. The smallest absolute value of ϕ_T is predicted for Surrogate 11, at 0.5%.

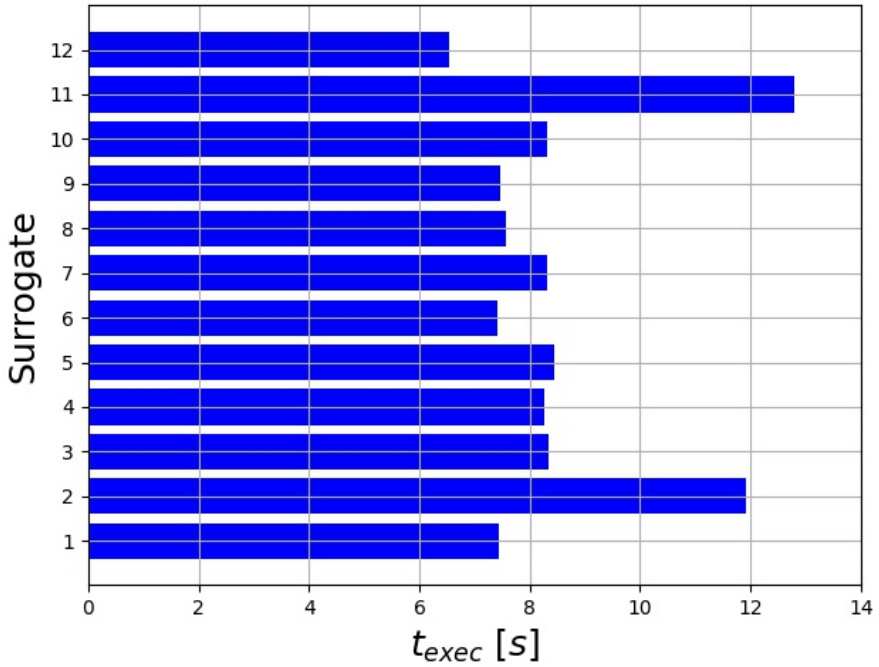

Figure 3.10: Execution time for each surrogate.

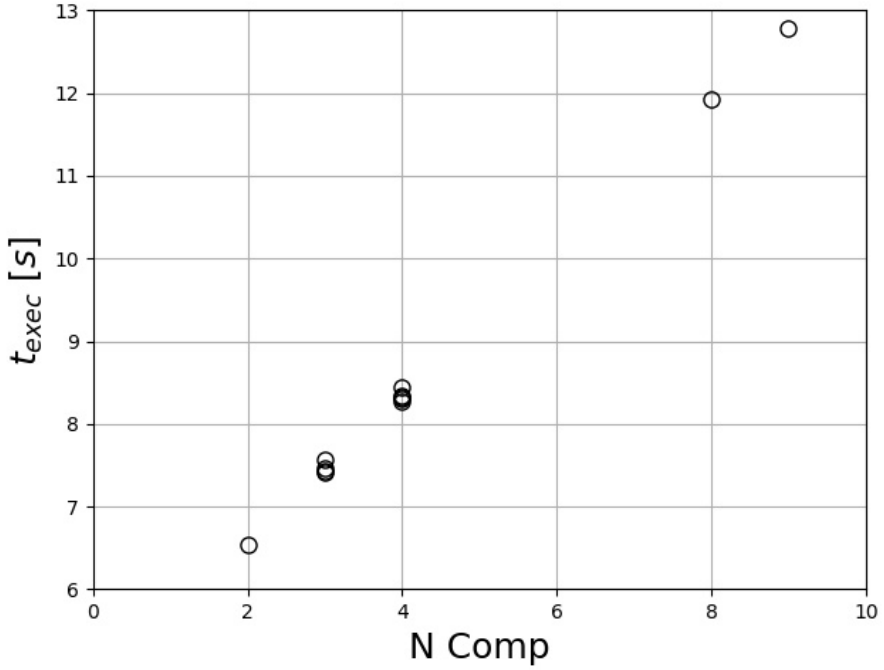

Figure 3.11: Execution time *versus* the number of components.

In order to evaluate the computational cost of each numerical simulation, the execution time required to run 500 time steps was measured and the values acquired for each surrogate are

shown in Fig. 3.10. This time turned out to be proportional to the number of components used in surrogates as shown in Fig. 3.11. The computational cost of simulations using Jet A complete composition, with 61 components, was always higher than that for surrogates. For example, to run 500 time steps using 61 components, it takes approximately 58.6 seconds, while in the case of 9 components, as in Surrogate 11, the required time is 4.6 times less. In the case of Surrogates 3 and 7, which have 4 components, the computational cost is about 7.1 times less. For Surrogate 12, with 2 components, the computational expense is 9 times less. This test considers only a single droplet. For spray simulations tracking millions of droplets, using surrogates to achieve computational cost reduction would be a sensible choice.

3.5.3 Numerical analysis

Temperature and mass fraction distributions computed by the analytical solutions are affected by the number of terms used in the series, the numerical accuracy of calculating the eigenvalues and the number of layers used to calculate integrals in these series. In order to evaluate the influence of these parameters, and the time step (Δt) used in calculations, on the computational cost and on the accuracy of the results, 8 cases considering the complete Jet A composition were simulated, as presented in Table 3.5. The five parameters used in the present analysis are: the number of concentric layers used to discretise the droplet volume (n_{layers}), the absolute accuracy of the bisection method (α_{BSM}), the number of eigenvalues used to calculate the series in Eq. (3.34) (n_T), the number of eigenvalues used to calculate the series in Eq. (3.47) (n_Y) and the time step used in simulations.

The main focus of this section is to quantify how changing the above-mentioned five parameters affects the droplet diameter and temperature results, as well as the computational cost. All the simulations were conducted taking into consideration the same boundary and initial conditions as in Section 3.5.1, $T_{d_0} = 298$ K, $D_{d_0} = 1.38$ mm, $p_g = 0.1$ MPa, and $T_g = 573$ K. The time required for the droplet to reduce to 10% of its initial volume (t_{evap}) is considered, as well as the temperature difference at 5 s after the start of heating ($\phi T_{t=5s}$), namely the difference between the initial temperature and the average plateau temperature. Firstly, the values of both parameters, t_{evap} and $\phi T_{t=5s}$, are computed for Case 1, for which the finest mesh and the shortest time steps are used. For this case, $t_{\text{evap}} = 10.72$ s and the average temperature at 5 s was 341.2

K, which represented $\phi T_{t=5s} = 43.2$ K. The computational cost is evaluated as the execution time needed to run 10 ms of the droplet lifetime t_{exec} for each case. Since Δt varied, the number of time steps required to reach the target time of 10 ms also varied. The data for each case is presented in Table 3.5.

The accuracy of calculations was assessed based on the relative errors of calculation of t_{evap} and $\phi T_{t=5s}$ in relation to Case 1:

$$\tilde{t}_{\text{evap}} = \frac{t_{\text{evap,Case1}} - t_{\text{evap}}}{t_{\text{evap,Case1}}} \times 100\%, \tag{3.75}$$

$$\tilde{\phi T}_{t=5s} = \frac{\phi T_{t=5s,\text{Case1}} - \phi T_{t=5s}}{\phi T_{t=5s,\text{Case1}}} \times 100\%. \tag{3.76}$$

Table 3.5: Analysis of the effects of numerical parameters for 8 cases.

Case	n_{layers}	α_{BSM}	n_T	n_Y	Δt [s]	$\tilde{t}_{\text{evap}}$ [%]	$\tilde{\phi T}_{t=5s}$ [%]	t_{exec} [s]
1	1000	10^{-12}	200	100	1×10^{-6}	-	-	4133.8
2	500	10^{-12}	200	100	1×10^{-5}	0.7	1.2	342.3
3	250	10^{-12}	200	100	5×10^{-5}	1.1	2.6	31.6
4	100	10^{-12}	200	100	1×10^{-3}	2.4	8.2	1.0
5	250	10^{-8}	200	100	5×10^{-5}	1.6	5.7	31.3
6	250	10^{-12}	100	50	5×10^{-5}	1.1	2.6	16.5
7	250	10^{-12}	50	25	5×10^{-5}	1.1	2.6	9.2
8	250	10^{-12}	20	20	5×10^{-5}	1.1	2.6	7.4

As follows from Table 3.5, for Case 2 the computational cost is approximately 12 times lower than for Case 1. This is achieved by reducing n_{layers} from 1000 to 500 and increasing Δt from 10^{-6} s to 10^{-5} s. The difference in predicted evaporation time and temperature in this case is rather small, at 0.7% and 1.2%, respectively. When n_{layers} is reduced to 250 and Δt increased to 5×10^{-5} s, maintaining the values of all the other parameters (see Case 3), the computational cost is approximately 131 times lower, while the relative errors for estimating t_{evap} and $\phi T_{t=5s}$ are only 1.1% and 2.6%, respectively. When n_{layers} was reduced to 100 and Δt increased to 10^{-3} s, maintaining the values of all the other parameters (see Case 4), the computational cost was more than 4000 times lower, while the relative errors of estimating t_{evap} and $\phi T_{t=5s}$ are still only

2.4% and 8.2%, respectively.

Comparing Cases 3 and 5, it can be observed that even though increasing α_{BSM} reduces the computational cost, this reduction is not significant. On the other hand, this leads to more than doubling of $\phi\tilde{T}_{t=5s}$, which brings into question the usefulness of adopting Case 5 instead of Case 3. Analysis of Cases 3, 6, 7, and 8 shows that reducing n_T and n_Y from 200 and 100 to 20 and 20, respectively, does not affect the results of calculations of droplet diameters and temperatures, but leads to a reduction in execution time from 31.6 s to 7.4 s. Note that if Surrogates 3, 7, 11 or 12, which showed the best performance in Section 3.5.2, were used, the execution time needed would be even lower due to the reduction in the number of components used in calculations.

3.6 Summary of the chapter

A Discrete Component Model (DCM), based on the analytical solutions to the heat transfer and species diffusion equations, is used to analyse the droplet heating and evaporation of Jet A and its surrogates. The Abramzon-Sirignano model is used for the analysis of the processes in the gas phase during droplet heating and evaporation. The partial pressures of vapour species are estimated based on Raoult's law. The implementation of these models into the MFSim code opens the way to modelling the evaporation and combustion of fuel sprays.

The results achieved using the MFSim code, with new models implemented into it, are successfully validated against experimental results described in Wang *et al.* (2018). Heating and evaporation characteristics of droplets of 12 surrogates are compared with those of Jet A droplets using the same input parameters as in the experiments described in Wang *et al.* (2018). It is shown that the evaporation time of a droplet of Surrogate 12 from Abdul-Jameel *et al.* (2019) is the closest to that predicted for a Jet A droplet, while Surrogate 3 from Dooley *et al.* (2010) and Surrogate 7 from Yu, Ju and Gou (2016) presented the best results when droplet evaporation rate was the target parameter. Furthermore, the maximum temperature predicted for droplets of Surrogate 11 from Won *et al.* (2017) is shown to be the closest to that predicted for a Jet A droplet. Considering the three target parameters simultaneously, Surrogate 11 is the best one to represent Jet A heating and evaporation processes. Therefore, it is used in Chapter 5 for the multicomponent simulations.

Sensitivity analysis of various numerical parameters was conducted, which included: the number of concentric layers used to discretise the droplet volume, the absolute accuracy of the bisection method used for finding the eigenvalues in the analytical solutions for temperature and species mass fractions, the number of terms in the series for temperature and species mass fractions, and the duration of time steps used in simulations. For the investigated cases, it is shown that: the number of layers should not be lower than 250; using a less restrictive accuracy for finding the eigenvalues does not significantly reduce the computational cost and results in greater deviations; and the number of terms of the series for temperature and species mass fractions can be reduced from 200 to 20 almost without affecting the accuracy of calculations. Additionally, it is observed that droplet temperature is more sensitive than evaporation time to variations in the analysed numerical parameters. Finally, it is demonstrated that the best compromise between accuracy and CPU requirement is achieved for the combination of numerical parameters used in Case 8 shown in Table 3.5. This combination of numerical parameters, $n_{\text{layers}} = 250$, $\alpha_{\text{BSM}} = 10^{-12}$, $n_T = 20$, $n_Y = 20$ and $\Delta t = 5 \times 10^{-5}$, can also be used to study other multicomponent droplets.

CHAPTER IV

DROPLET BREAKUP MODEL

Droplet fragmentation is a multiphase flow process common for a wide variety of spray systems (LEFEBVRE; MCDONELL, 2017). Liquid injection in combustion systems typically results in droplet dynamics that are not in equilibrium with the ambient gaseous phase flow characteristics. Therefore, droplets are subject to aerodynamic forces that cause deformation, oscillations, and a variety of breakup events, as shown in Fig. 4.1. Atomisation in sprays is defined as the disintegration of larger droplets into smaller ones. In other words, it is said that parent droplets fragment into child droplets. It is known that such processes can be classified by the Weber number:

$$We_g = \frac{2\rho_g(u_i - u_{d,i})^2 R_d}{\sigma}, \tag{4.1}$$

which represents the ratio between the disruptive aerodynamic force and the restorative surface tension σ, and the Ohnesorge number:

$$Oh_l = \frac{\sqrt{We_l}}{Re_l} = \frac{\mu_l}{\sqrt{2\rho_l R_d \sigma}}, \tag{4.2}$$

which compares the viscous force to the surface tension. A larger Weber number indicates a higher tendency toward fragmentation, while a larger Ohnesorge number indicates a lower tendency toward fragmentation. Droplet viscosity prevents deformation and also dissipates energy

supplied by the aerodynamic forces (ASHGRIZ, 2011). According to Guildenbecher, López-Rivera and Sojka (2009), the influence of liquid viscosity on the breakup regime reduces when Oh_l is below 0.1, leaving We_g as the dominant factor. Using these parameters, widely accepted regime diagrams for droplet deformation and breakup have been compiled, such as the one displayed in Fig. 4.2.

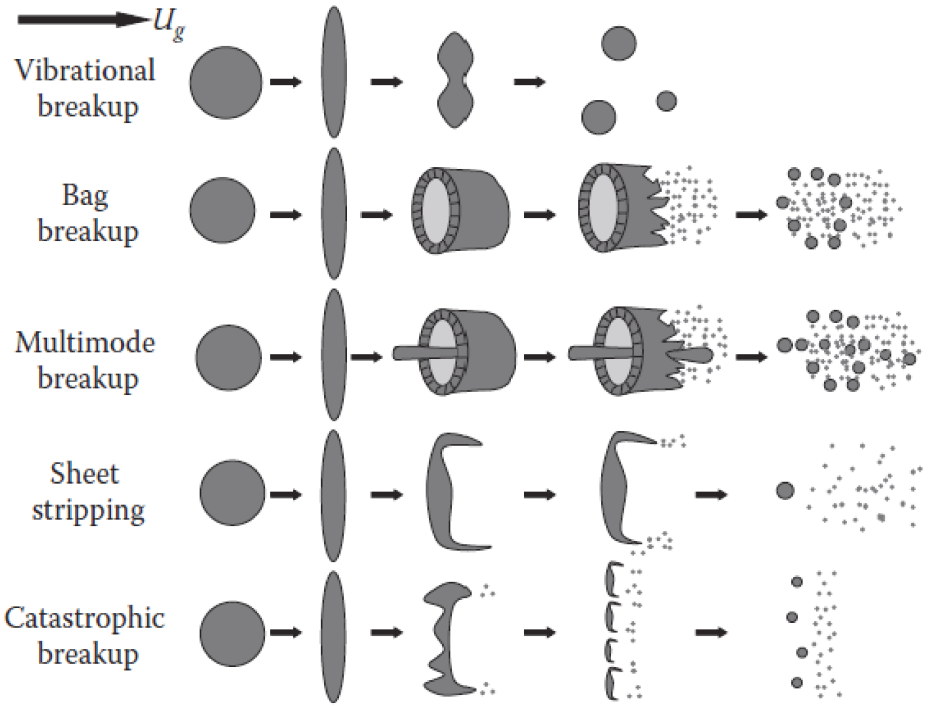

Figure 4.1: Typical modes of droplet breakup (MICHAELIDES; CROWE; SCHWARZKOPF, 2016).

A variety of models have been developed to simulate droplet breakup over the past several decades. However, two models in particular have found wide acceptance and are used extensively in both academic and commercial CFD codes. The first is the WAVE model originally developed by Reitz (1987). The second is the Taylor-Analogy-Breakup (TAB) model originally developed by O'Rourke and Amsden (1987). The WAVE breakup model relates the mechanism of droplet breakup with the Kelvin-Helmholtz instabilities along a cylindrical viscous liquid jet, assuming that the time of breakup and related droplet sizes are proportional to the growth rate and wavelength of the most unstable Kelvin-Helmholtz instability. The TAB model, on the other hand, is developed based on Taylor's analogy between drop dynamics and a forced spring-mass-damper system. More recently, stochastic breakup models have gained some popularity due to their capacity to predict the essential global features of sprays without being too computationally expensive (IRANNEJAD;

JABERI, 2014). The stochastic droplet breakup model proposed by Gorokhovski and Saveliev (2003) stands out for its ability to generate droplets with different sizes leading to log-normal distribution. Additionally, in high pressure injection sprays, which are characterised by large Weber numbers, the hydrodynamic mechanisms of atomisation are even more complex due to turbulence. Under such conditions, stochastic breakup models are more appropriate than deterministic ones (SAZHIN, 2014).

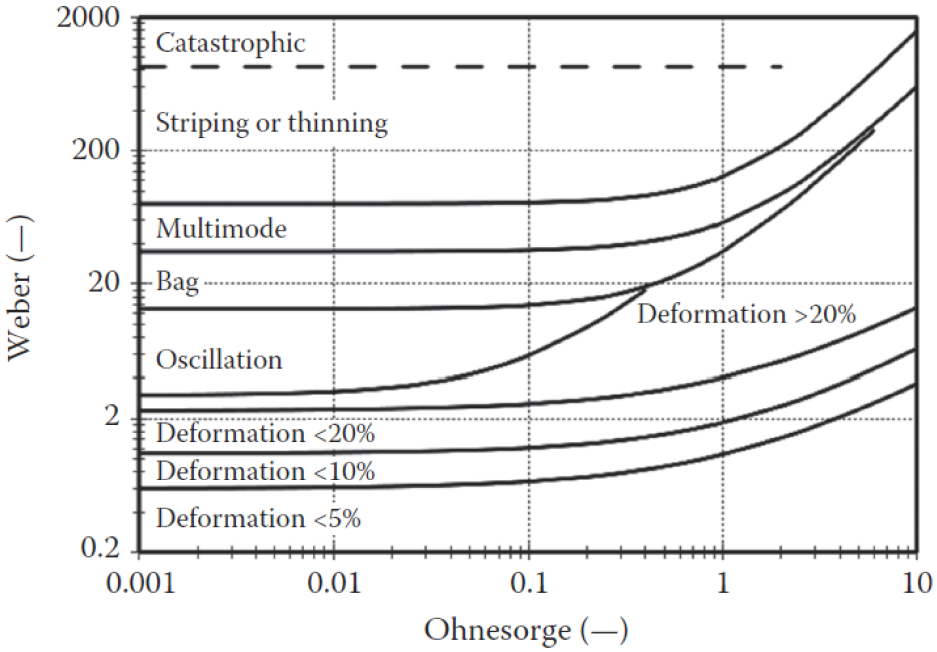

Figure 4.2: Droplet deformation and breakup regime map considering We_g and Oh_l (MICHAELIDES; CROWE; SCHWARZKOPF, 2016).

This chapter is organized as follows. In Section 4.1, the mathematical model for droplet breakup is presented with numerical and computational details. In Section 4.2, the results of comparing modelling predictions with experimental data are presented and discussed. Finally, Section 4.3 summarises the main conclusions achieved in this chapter.

4.1 Mathematical model with numerical and computational details

As mentioned before, a hybrid deterministic-stochastic secondary breakup model capable of generating a broad range of droplet sizes at high Weber numbers is used for predicting the new droplet formation (GOROKHOVSKI; SAVELIEV, 2003). The main assumption of the model is that the number of fragments generated by a breakup event is independent of the parent

droplet size. Kolmogorov (1941) demonstrated that under this assumption and for a constant breakup frequency, the long-time limit of droplet size distribution follows a log-normal law. In this model, the size distribution of droplets generated by the breakup is based on the solution of a Fokker–Planck equation with main parameters being the breakup frequency and the first two moments of the fragmentation intensity spectrum. The breakup frequency and, consequently, the evolution of droplet diameter are controlled by the relative velocity between the gas and liquid phases and their thermophysical properties.

From a global perspective and a processual viewpoint, a breakup model consists in the following steps: 1) at each time step of the simulation, it is checked whether a droplet remains stable as it is or disintegrated into others; 2) if a parent droplet breaks up, the size of resulting child droplets must be determined; 3) lastly, in addition to the radius, all other physical properties of the child droplets must be defined. The physical criterion used to distinguish between breaking and stable droplets is focused on establishing whether a certain droplet Weber number exceeds a critical value, $We > We_{cr}$. This relation can be rearranged to define a critical droplet radius $R_{d,cr}$ above which droplets are considered unstable:

$$R_{d,cr} = \frac{We_{cr}\sigma}{2\rho_g(u_i - u_{d,i})^2}, \tag{4.3}$$

where the critical Weber based on droplet radius is defined following Pilch and Erdman (1987) to account for the viscosity effects:

$$We_{cr} = 6\left(1 + 1.077 Oh_l^{1.6}\right). \tag{4.4}$$

In addition to the droplet stability criterion, a characteristic breakup time scale must be determined, since a droplet does not undergo breakup immediately once it becomes unstable. Before, it is either deformed by aerodynamic forces or oscillates through individual droplet instability mechanisms. Gorokhovski and Saveliev (2003) specifically associates the characteristic droplet breakup time scale with the fastest growth rate of Rayleigh-Taylor waves in the high-speed limit:

$$t_d^{bu} = B\frac{R_d}{|u_i - u_{d,i}|}\sqrt{\frac{\rho_l}{\rho_g}}, \tag{4.5}$$

with $B = \sqrt{3}$.

Thus, it is checked at each computational time step if the droplet lifetime exceeds the breakup time scale given by Eq. (4.5) and if its Weber number lies above the critical value provided by Eq. (4.4). If both criteria are fulfilled for the considered droplet, it breaks up. On the contrary, if the parent droplet does not break up in a certain time step, its lifetime is just incremented then. Note that the droplet lifetime is initialized to zero for newly injected droplets and newborn child droplets.

For each breaking droplet, the size of its child droplets must be determined, knowing that one parent droplet of radius R_d generates several child droplets with different radii R. Apte, Gorokhovski and Moin (2003) showed that the evolution of the droplet radius distribution under breakup is governed by:

$$T(R) = \frac{1}{2}\left[1 + erf\left(\frac{ln(R/R_d) - \zeta_1}{\sqrt{2\zeta_2}}\right)\right], \tag{4.6}$$

where erf denotes the error function.

The relation presented in Eq. (4.6) yields the cumulative droplet distribution after the breakup of a parent droplet of radius R_d. Following Gorokhovski and Saveliev (2008), the two moments, ζ_1 and ζ_2, are assumed to be -0.36 and 0.14, respectively, where the former controls the mean of the distribution used to generate the droplet sizes after breakup and the later controls the deviation from this mean.

Note that the number and size of new droplets are determined by a stochastic sampling procedure that conserves the liquid mass. Hence, child droplets radii are randomly generated as long as their mass remains below the mass of the parent droplet:

$$\sum_{1}^{n_d}\left(R_{d,child}^3\right) < R_{d,parent}^3. \tag{4.7}$$

When the sum of the child droplets masses exceeds the parent droplet mass, the last sampled

radius is rejected. Instead, a final child droplet radius is deduced from the mass difference between parent and the sum of the child droplets to ensure mass conservation during breakup.

Apart from the radius, the child droplets inherit all physical properties from their parents. However, the child droplets velocities differ from the parent droplet velocity by adding a factor $u_{d,i}^{bu}$ to the parent droplet velocity. The additional velocity is randomly distributed in a plane normal to the relative velocity vector between the gas and parent droplet $(u_i - u_{d,i})$ as seem in Fig.4.3, and its norm is given by:

$$|u_{d,i}^{bu}| = R_d / t_d^{bu}. \tag{4.8}$$

This is based on the physical picture of parent droplets being torn apart by aerodynamic forces, giving momentum to the newly formed droplets in the direction normal to the relative velocity between the gas and parent droplets (O'ROURKE; AMSDEN, 1987). In fact, this velocity is responsible for the radial expansion of the spray. To finalize the breakup event, the parent droplet is removed from the simulation at the end of the time step.

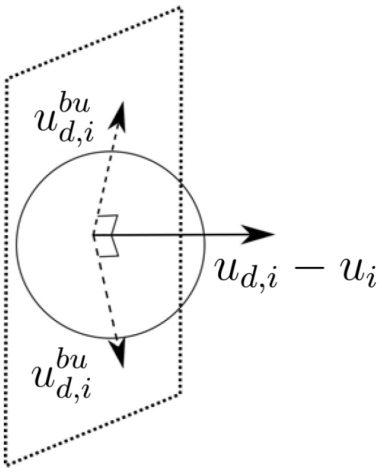

Figure 4.3: Schematic illustration of the velocity $u_{d,i}^{bu}$ added to a newborn droplet after the breakup event (SENONER, 2010).

4.2 Results and discussion

The classical non-evaporating spray experiment performed by Hiroyasu and Kadota (1974), which is benchmark case for atomisation studies, is used in this section to evaluate droplet dispersion and breakup models. In this experiment, a high-speed liquid jet of diesel fuel is sprayed

Parameter	Value
Ambient pressure [MPa]	1.1
Ambient temperature [K]	300.0
Injection time [ms]	2.5
Injection velocity [m/s]	102.0
Injection diameter [μm]	300.0
Injection mass flow rate [g/s]	6.05
Surface tension [N/m]	0.0261
Gas density [kg/m^3]	12.36
Gas viscosity [Pa·s]	1.77E-5
Liquid density [kg/m^3]	840
Liquid viscosity [Pa·s]	2.1E-3
We_g [-]	1478
Oh_l [-]	0.026

Table 4.1: Test case conditions.

into a closed cylindrical chamber filled with constant temperature stagnant nitrogen. The injector is a single hole nozzle with orifice diameter of 300 μm. The computational domain consists of a cylindrical volume with a length of 13.6 cm and a diameter of 5.6 cm, while the nozzle is placed in the centre of the most upstream transversal section of this domain. A sketch of the cylindrical domain geometry is provided in Fig. 4.4. Other information referring to ambient conditions, injection parameter, diesel and nitrogen physical properties are displayed in Table 4.1. We_g and Oh_l at injection indicate that the disintegration of the liquid takes place in a catastrophic mode (see Figs. 4.1 and 4.2).

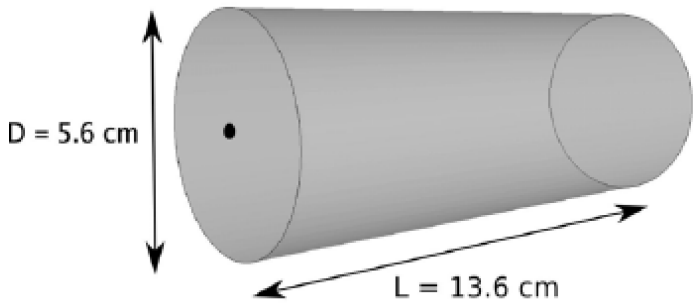

Figure 4.4: View of the cylindrical domain, where the black circle at the centre denotes the location of the injection point (SENONER, 2010).

The computational mesh used in this work is composed of $128\times64\times64$ hexaedric cells, in x, y and z directions, respectively, forming an uniform grid and the time step used is $\Delta t = 1.0\times10^{-6}$

s. As in the experiment, the domain is completely closed and a no-slip condition is applied at the wall. Due to the high liquid injection velocity, the two-way coupling between both phases is strong, which consequently induces a substantial acceleration of the gas in the spray region. In order to address the generated gradients, the CUBISTA scheme is used for convection because of its non-difusive nature. Furthermore, the dynamic Smagorinsky turbulence closing model is used for turbulence closure, no parcel approach is used in the present work, and collision/coalescence effects are not taken into account.

Fig. 4.5 displays the simulated spray pattern at $t = 0.5\ ms$. The disintegration of the injected droplets into smaller ones is clearly visible. A fine mist, located mostly in the spray wake region, is a result of the child droplets that travel radially outwards as they inherit a velocity component normal to the relative velocity ($u_{d,i}^{bu}$). These small droplets are then gradually decelerated due to momentum exchange with the gaseous phase. It is believed, though, that the account for collision/coalescence phenomena would limit the occurrence of the mist effect, as verified by Irannejad and Jaberi (2014).

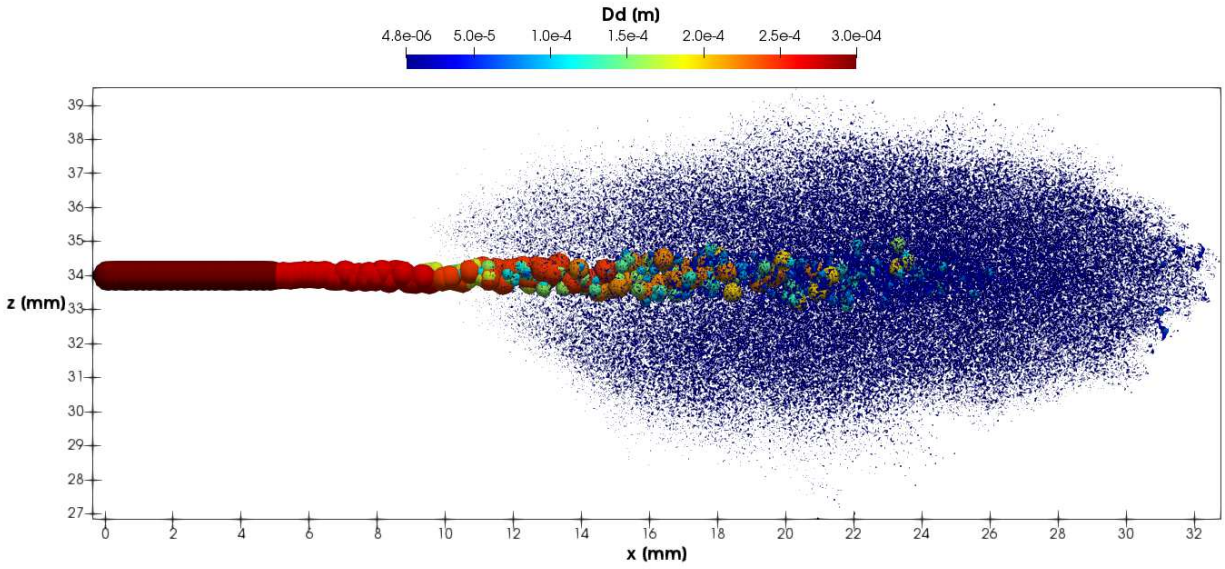

Figure 4.5: Spray pattern on the middle plane at $t = 0.5\ ms$. The droplets sizes and colors indicate their diameter.

Fig. 4.6 shows the spray tip penetration length predicted by the simulation compared with experimental measurements. Note that the spray tip is computed as the axial distance including more than 99% of the liquid mass (PATEL; MENON, 2008). The spray penetration curve tends to flatten as time evolves because the spray momentum in axial direction is progressively reduced

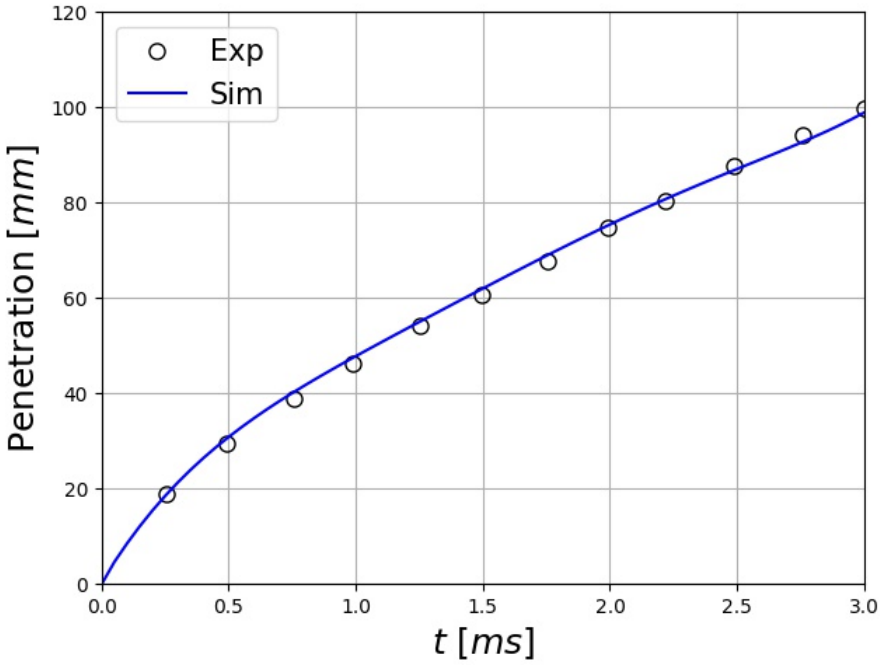

Figure 4.6: Spray penetration as a function of time.

due to the increasing radial expansion of the spray and the momentum exchange between the droplets and the carrier gas. Overall, the numerical results are in a reasonable agreement with the experimental data.

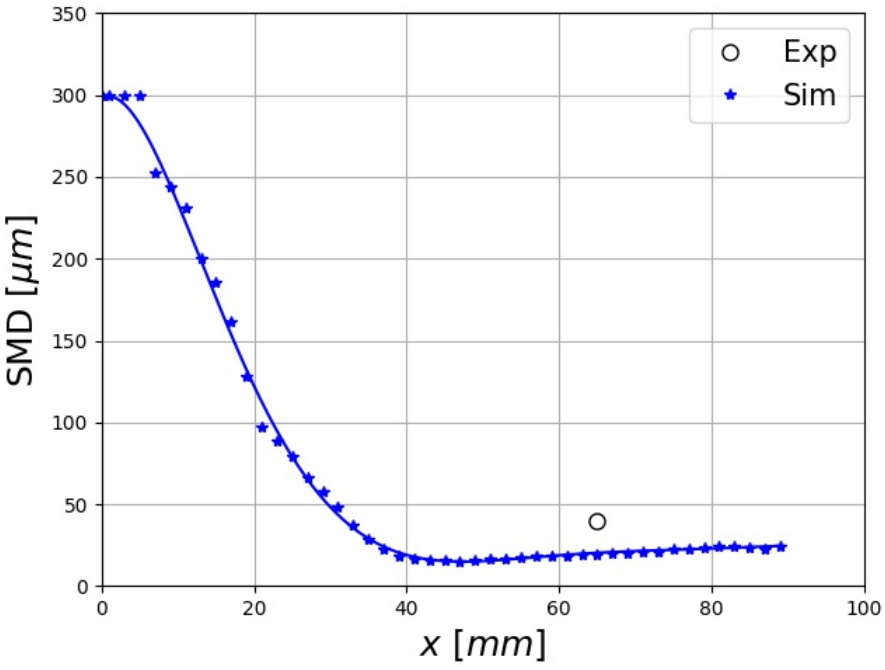

Figure 4.7: Variation of Sauter mean diameter (SMD) along the spray direction.

The Sauter mean diameter (SMD), given by:

$$D_{d,32} = \frac{\sum_{1}^{n_d} {D_d}^3}{\sum_{1}^{n_d} {D_d}^2}, \tag{4.9}$$

describes the averaged ratio of droplet volume to surface, considering n_d droplets. Fig. 4.7 displays the evolution of SMD along the spray axis x. The abscissa origin represents the location of the nozzle. The SMD is obtained from an average of the droplet diameters in transversal slices of 2 mm thickness. Experimental data through the axial direction are not available, but a single data measurement point at $x = 65\ mm$, which is included in Fig. 4.7 for comparison. The curve decreases rapidly close to injection point, caused by the dominant breakup process, before reaching more or less constant value further downstream. As reported by Irannejad and Jaberi (2014), taken into account collision and coalescence processes impacts the results at locations far from the nozzle. Senoner (2010) have tested different values for the constants ζ_1 and ζ_2 in order to improve the SMD prediction, but he also concluded that coalescence effects need to be included. However, Irannejad and Jaberi (2014) declared that coalescence does not have a dominant effect on the global evaporating spray variables, which is the focus of the present research.

4.3 Summary of the chapter

This chapter presented the validation of the secondary breakup model implemented in the MFSim code considering a high-speed jet of fuel sprayed into a quiescent gaseous medium. The simulation consisted of injecting a liquid jet formed by droplets through a single hole nozzle into a closed cylindrical chamber at high gas pressure. No effects of droplet heating and evaporation was studied in this chapter, since ambient gas and liquid droplets were in thermal equilibrium at $T =$ 300.0 K. The results achieved showed good agreement with experimental data for both liquid penetration length and SMD. However, the underestimation of the SMD compared to experimental data seem to happen due to the negligence of coalescence phenomena in the simulation. Additionally, it is important to highlight that even though the breakup constants, ζ_1 and ζ_2, used here were able represent the fragmentation behaviour as expected, they may not be suitable for

every condition. This aspect requires further investigation depending on the case of interest.

CHAPTER V

COMPUTATIONAL SIMULATIONS

5.1 Temperature distribution inside droplets

This section is focused on the verification of the different models implemented in the MFSim code to solve the temperature inside a droplet. The idea here is to simulate the heating and evaporating processes of a single n-dodecane droplet in similar conditions as the simulations later performed in Section 5.3 for multiple droplets in a spray case. The temporal evolution of droplet diameter and temperature are analysed for various models and the physical behaviour of each parameter is evaluated in comparison with the results achieved by Abramzon and Sirignano (1989) when they also verified the implementation of these various models. Table 5.1 present the test case conditions, such as droplet initial parameters, ambient gas parameters and some numerical parameters. Note that the numerical parameters chosen here are based on the results from Section 3.5.3, but n_{layers} and Δt change depending on $D_{d,0}$.

Figs. 5.1, 5.2 and 5.3 show the temporal variation of droplet non-dimensional diameter ($D_d/D_{d,0}$), surface temperature (T_s) and average temperature (T_{av}), respectively. Each figure present the simulation results achieved for four different models: infinite thermal conductivity model (ITC), finite thermal conductivity model (FTC), effective thermal conductivity model (ETC), and finite thermal conductivity model with the assumption of $k_l \to \infty$ (FTC inf). More precisely, it is assumed that $k_l = k_l \cdot 1 \times 10^6$. As noticed in Fig. 5.1, thermal swelling effects are taken into account in this simulation, which was not the case in the simulation performed

Parameter	Value
Droplet diameter $D_{d,0}$ [μm]	50.0
Droplet temperature $T_{d,0}$ [K]	300.0
Droplet velocity $u_{d,0}$ [m/s]	30.0
Gas velocity u_g [m/s]	0.0
Gas pressure p_g [atm]	10.0
Gas temperature T_g [K]	1200.0
Number of layers n_{layers} [-]	50
Time step Δt [s]	1×10^{-6}
Bisection method accuracy α_{BSM} [-]	10^{-12}
Number of eigenvalues for temperature n_T [-]	20
Number of eigenvalues for species diffusion n_Y [-]	20

Table 5.1: Test case conditions for n-dodecane single droplet heating and evaporation.

by Abramzon and Sirignano (1989). Therefore, in order to better compare the droplet diameter evolution of each model with the results from Abramzon and Sirignano (1989), the results for a new simulation without thermal swelling effects is shown in Fig. 5.4.

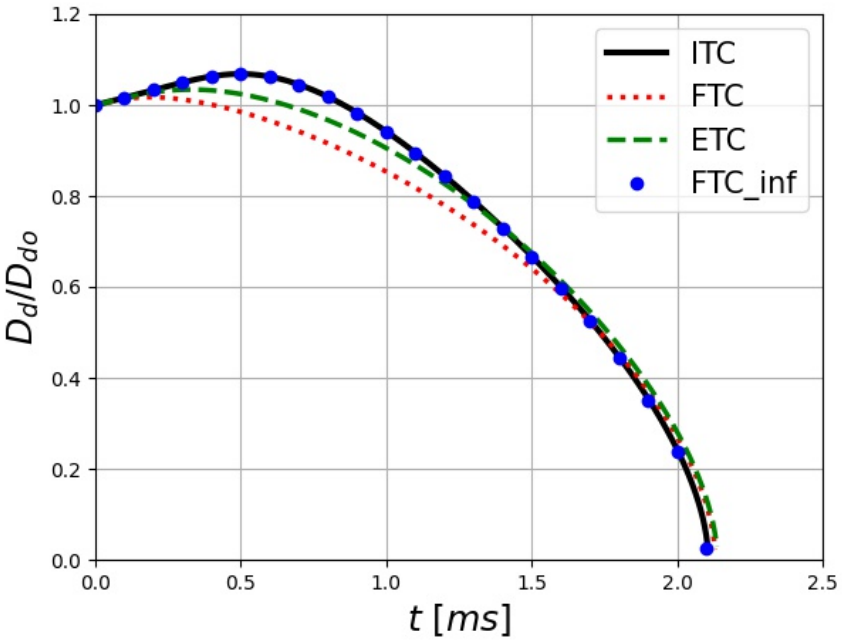

Figure 5.1: Normalised droplet diameter *versus* time.

First, in all the figures presented in this section, for both droplet diameter and temperature, it is possible to see that for large k_l the FTC model converge to the ITC model as expected, since having a large k_l represents going from a finite thermal conductivity to an infinite one. From now on, when discussing the results of each figure, FTC inf model is not mentioned because it

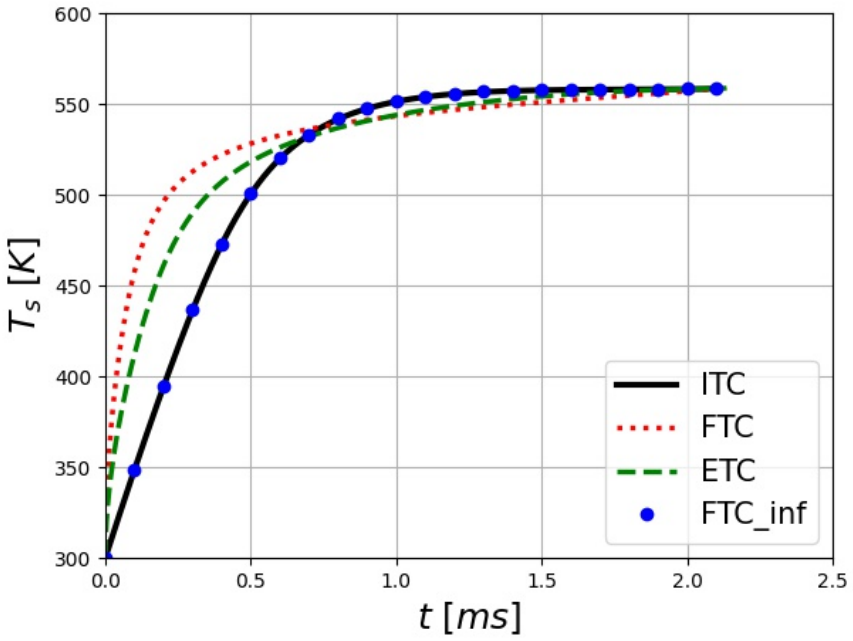

Figure 5.2: Droplet surface temperature *versus* time.

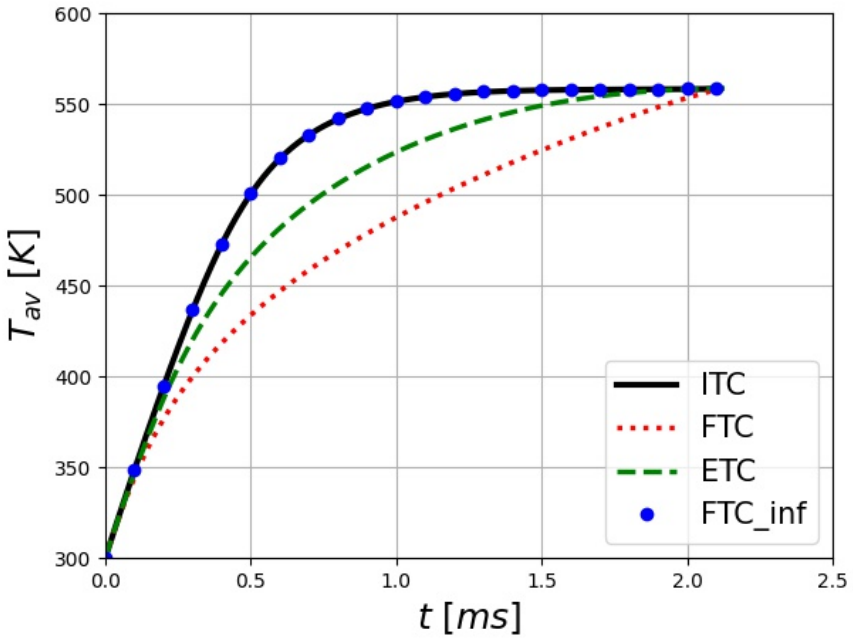

Figure 5.3: Droplet average temperature *versus* time.

presented results similar to ITC. In Fig. 5.1, it can be observed that by taken into account the thermal swelling effects, ITC model is the one which achieved the higher droplet diameter. Also, due to thermal swelling, there is not a significant difference between the droplet lifetime predicted by each model, since the thermal swelling effect counterbalance the convection effect. In Fig. 5.4, on the other hand, the same tendency reported by Abramzon and Sirignano (1989) is observed:

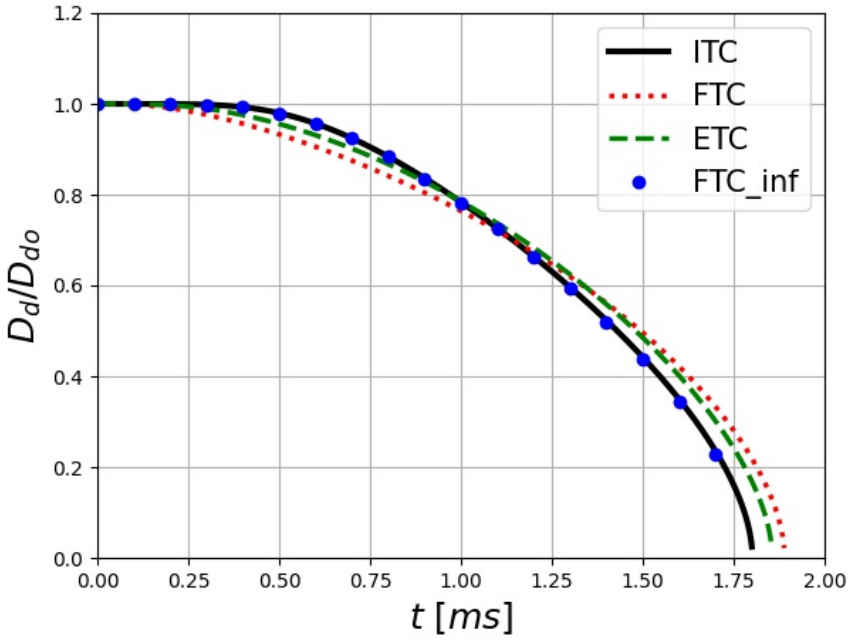

Figure 5.4: Normalised droplet diameter *versus* time when thermal swelling effects are not taken into account.

droplet lifetime predicted by ITC is the lowest one, followed by ETC and FTC, respectively, which is consistent with what is expected physically. By assuming an infinitely large k_l, as in ITC, there is no temperature gradient inside the droplets. Actually, all the energy transferred from the ambient gas to the liquid droplet is instantaneously and uniformly distributed inside it. Therefore, it evaporates quickly, as seen in Fig. 5.4. Once a finite k_l is considered, as in FTC, the heat diffusion effects, namely conduction, lead to a slower heating process. Additionally, if the effects of bulk fluid motion, namely advection, are incorporated, as in ETC, the droplet evaporates quicker than when considering FTC, but slower than when considering ITC.

As for the droplet temperature, it is observed in Figs. 5.2 and 5.3 that both average and surface temperature of all models tend to the same value. Also, the behaviour of each model is in agreement with what was observed in Abramzon and Sirignano (1989). Average temperature growth in ITC happens quicker, followed by ETC and FTC, respectively. Surface temperature growth, contrarily, happens faster for FTC, followed by ETC and ITC, respectively. The behaviour of both average and surface temperature for each model is justified by the effects of heat diffusion and bulk fluid motion previously explained. The opposite tendency observed between average and surface temperature predictions is due to the fact that considering convection effects on the

droplet heating process slows down the heating of the droplet centre, which results in $T_{av} < T_s$ at a given time. It is important to highlight here that for ITC $T_{av} = T_s$, since there is no temperature gradient.

5.2 Integration of droplet atomisation, heating and evaporation models

This section is dedicated to demonstrate the functionality of the droplet atomisation, heating and evaporation models implemented when used together for simulating spray problems. Also, it is verified the effect of the Lagrangian source/sink terms on the Eulerian phase. As mentioned in Section 1, two types of spray flows are studied here, liquid jet injection in a quiescent gaseous environment and liquid jet injection into a gaseous crossflow. The simulations are performed considering both monocomponet and multicomponent droplets. For the monocomponent simulations, n-dodecane is used. For the multicomponent simulations, Surrogate 11 is used to represent the heating and evaporation processes of aviation kerosene Jet A, based on the conclusions from Section 3.6. Table 5.2 presents Surrogate 11 composition in terms of mass fraction for each kth component, as well as its vapour pressure at 300.0 K. ID, as shown in Table 5.2, identifies how each component is later referred in the plot results. Note that vapour pressure is a property to measure the volatility of a certain substance. In other words, the more volatile a a substance is, it has a higher vapour pressure. In addition, for monocomponent simulations only ETC model is considered, while for multicomponent simulations both ETC and ED models are considered.

Table 5.2: Surrogate 11 composition in terms of mass fraction (Y_l) of each kth component, with its chemical formula, name, identifier and vapour pressure $p^*_{v,k}$ at 300.0 K.

Comps	Formulae	Names	ID	$Y_{l,k}$	$p^*_{v,k}$ [Pa]
1	C_8H_{18}	n-octane	NC8H18	0.017	2179.26
2	$C_{10}H_{22}$	n-decane	NC10H22	0.047	240.05
3	$C_{12}H_{26}$	n-dodecane	NC12H26	0.337	23.13
4	$C_{14}H_{30}$	n-tetradecane	NC14H30	0.131	1.92
5	$C_{16}H_{34}$	n-hexadecane	NC16H34	0.021	0.24
6	C_8H_{18}	iso-octane	IC8H18	0.026	3171.90
7	$C_{12}H_{26}$	iso-dodecane	IC12H26	0.161	21.92
8	C_7H_8	toluene	C7H8	0.052	4241.07
9	C_9H_{12}	1,3,5-trimethylbenzene	C9H12	0.227	382.50

5.2.1 Liquid jet injection into a gaseous crossflow

5.2.1.1 Geometry and computational details

The first test case simulates the injection of a liquid jet perpendicularly to a gaseous crossflow of nitrogen at high temperature. The computational domain consists of a rectangular box with a length of 128 mm and sides of 32 mm, as seen in Fig. 5.5. The gaseous bulk flow is in the x direction, while the liquid injection happens in the z direction. The liquid injection point is located 10 mm downstream the air inlet. Considering the air is injected with 120 m/s and the channel width is 32 mm, the flow Reynolds number is 2.32×10^5. Other information referring to ambient gas conditions and injection parameters are displayed in Table 5.3. We_g and Oh_l at injection indicate that the disintegration of the liquid takes place in a catastrophic breakup mode.

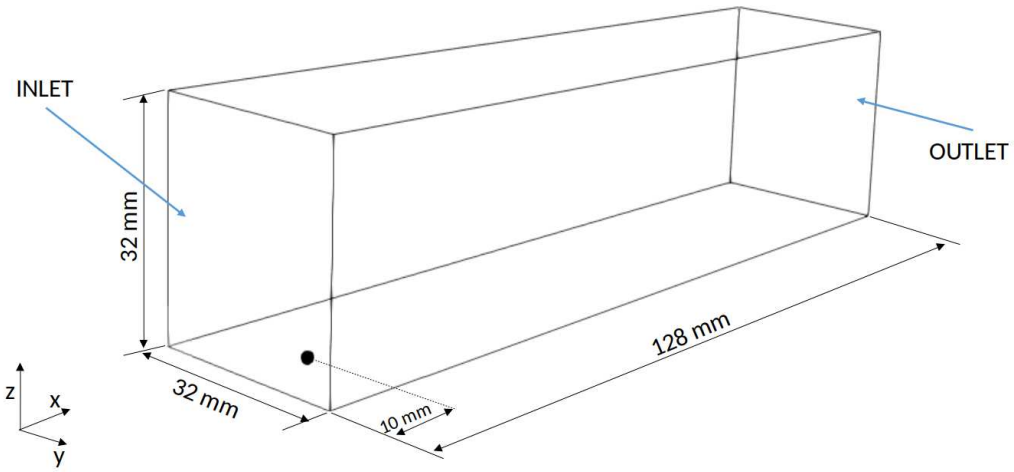

Figure 5.5: View of the computational domain, where the black circle are denotes the location of the injection point.

The computational domain is discretised considering an adaptive mesh with 4 levels of refinement and base level composed of $32 \times 8 \times 8$ hexaedric cells, in x, y and z directions, respectively. Vorticity, particle presence and temperature gradient are considered as criteria to determine where the mesh is refined. As for the domain boundary conditions, where it is neither inlet nor outlet in Fig. 5.5, the free-slip condition is applied. No turbulence generator is specified in the inlet for this case. Furthermore, the CUBISTA scheme is used for convection and the dynamic Smagorinsky model for turbulence closure. Other information referring to numerical parameters are in Table 5.4.

Parameter	Value
Gas pressure p_g [atm]	10.0
Gas temperature T_g [K]	1200.0
Gas bulk velocity u_g [m/s]	120.0
Liquid mass flow rate $\dot{m}_l$ [g/s]	3.0
Droplet diameter $D_{d,0}$ [μm]	450.0
Droplet temperature $T_{d,0}$ [K]	300.0
Droplet injection velocity $u_{d,0}$ [m/s]	40.0
We_g [-]	826
Oh_l [-]	0.015

Table 5.3: Test case conditions for jet injection in gaseous crossflow simulation.

Parameter	Value
Number of layers n_{layers} [-]	100
Time step Δt [s]	1×10^{-7}
Bisection method accuracy α_{BSM} [-]	10^{-12}
Number of eigenvalues for temperature n_T [-]	20
Number of eigenvalues for species diffusion n_Y [-]	20

Table 5.4: Numerical parameters for jet injection in gaseous crossflow simulation.

5.2.1.2 Results and discussion

Figs. 5.6 to 5.10 present the results considering monocomponent droplets. In Fig. 5.6, the adaptive computational mesh is shown, as well as the droplets injected in the domain. Both droplet colour and size are based on its diameter, but the droplet size representation is scaled by 5 in order to facilitate visualisation. Two main points should be observed in Fig. 5.6: mesh refinement and droplet size variation. First, the mesh criteria applied properly worked as there are 4 mesh levels and finest level is located in regions where there are particles, vorticity or temperature gradient. Second, droplets are injected with $D_{d,0} = 450.0$ μm and, as they interact with the hot gaseous crossflow, their diameter decreases because they evaporate and atomise. The minimum droplet diameter observed is of 50.0 μm due to the droplet vanishing criterion adopted for this simulation. Even though the droplets no longer exist below this limit, before deleting them from the domain their energy, mass and momentum are transferred for the Eulerian phase using Lagrangian source/sink terms.

In Fig. 5.7, the ambient gas temperature distribution in a mid plane at $y = 16$ mm is shown. From this figure it can be noticed the inter-phase coupling term for energy (${S_{c_pT}}^L$) is

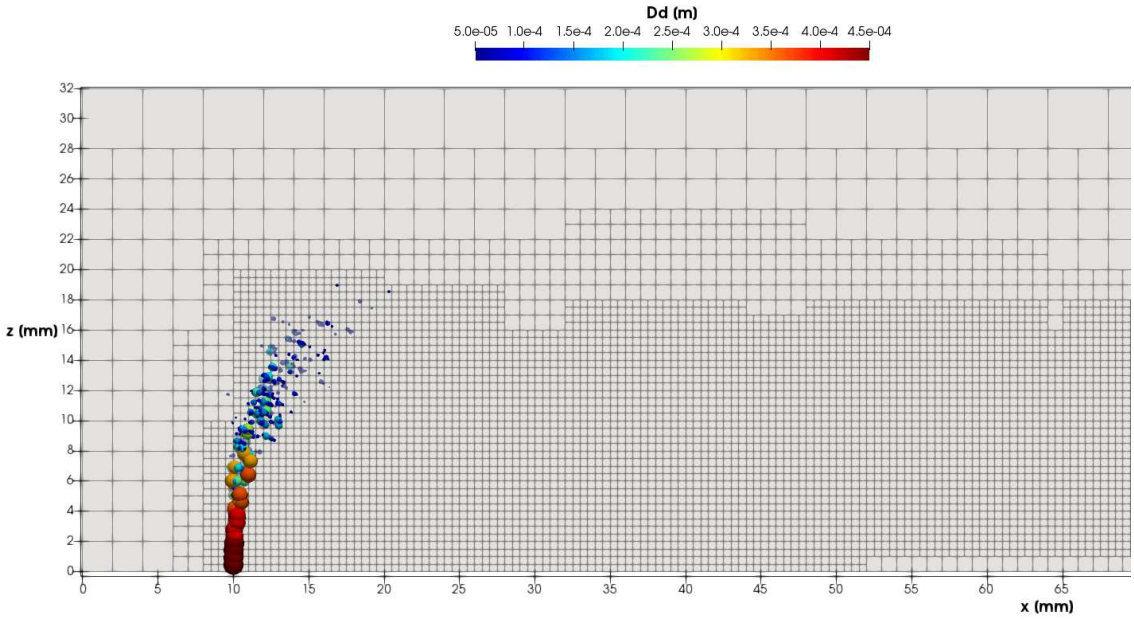

Figure 5.6: Computational mesh with droplets coloured their diameter for n-dodecane evaporation at $t = 5.0$ ms.

properly working. The liquid fuel droplets are injected with $T_{d,0} = 300.0$ K in a hot environment, so energy is transferred from the ambient to the droplets, resulting in a local reduction of the ambient temperature. The minimum ambient temperature of 1120 K is seen at approximately 40 mm downstream the injection point.

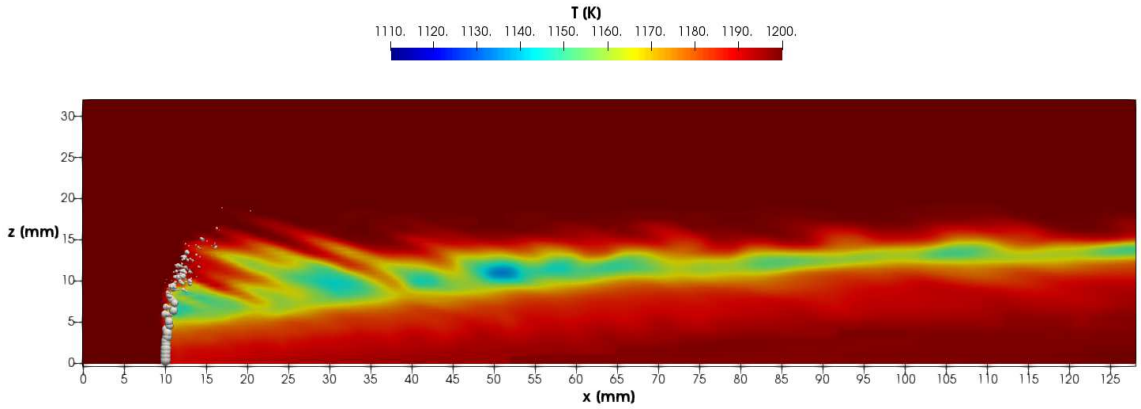

Figure 5.7: Contours of gas temperature in a mid plane for n-dodecane evaporation at $t = 5.0$ ms.

In Fig. 5.8, the mass fraction distribution of nitrogen and n-dodecane in a mid plane at $y = 16$ mm is shown. From this figure it can be noticed the inter-phase coupling term for species (${S_k}^L$) is properly working. As the liquid fuel droplets evaporate, the amount of vapour fuel in the ambient increases. Also, as $\sum_k Y_k = 1$, $Y_{N2} + Y_{NC12H26}$ must always be equals 1, which is

verified in Fig. 5.8. Finally, it is important to highlight that the turbulent vapour mixing expected in this type of flows is actually seen in Fig. 5.8.

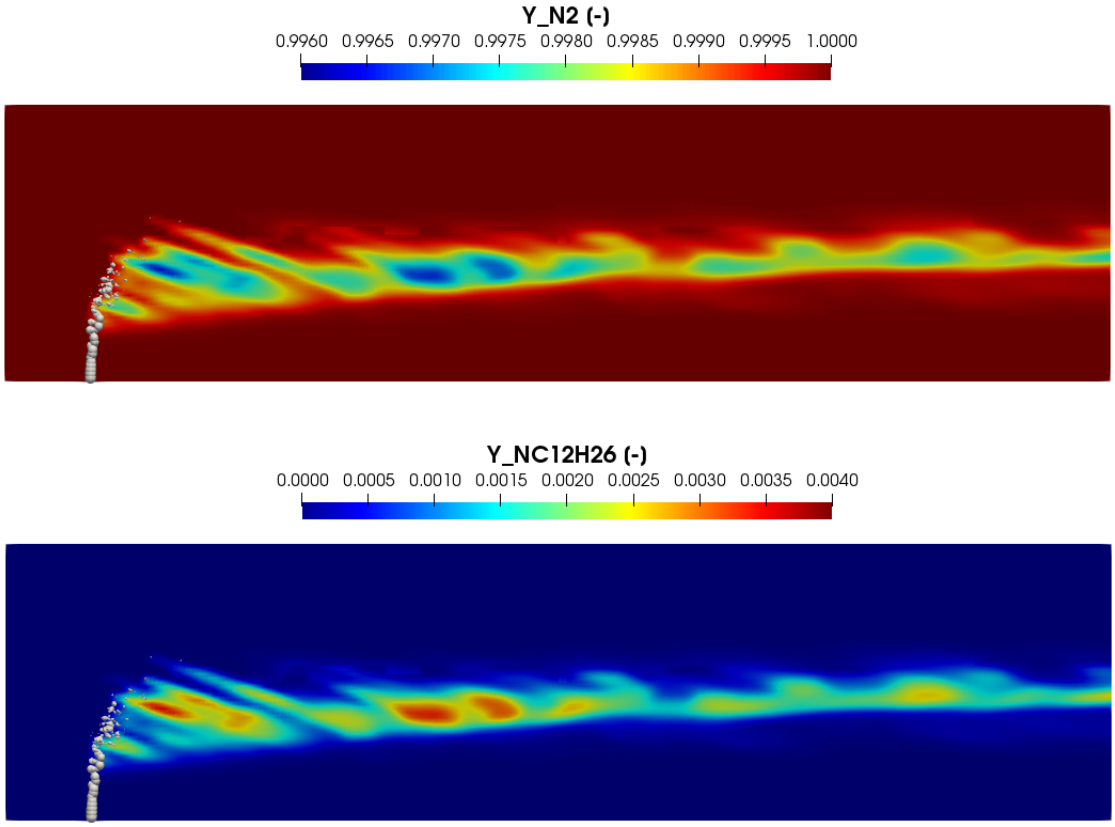

Figure 5.8: Contours of nitrogen and fuel vapour in a mid plane for n-dodecane evaporation at $t = 5.0$ ms.

In Fig. 5.9, a 3D visualisation of the fuel vapour mist resulting from n-dodecane evaporation. The injected droplets are also represented, as well as the blocks where the computational mesh is most refined.

In Fig. 5.10, criteria Q isosurfaces, which evidence the flow field coherent structures, are presented (JEONG; HUSSAIN, 1995). This figure shows that the presence of the jet of droplets is enough to disturb the flow to the point of generating turbulence structures. The wake seen happens due to the interaction between the gaseous crossflow and the liquid column formed by the droplets.

Figs. 5.11 to 5.14 present the results considering multicomponent droplets. In Fig. 5.11, the adaptive computational mesh is shown, as well as the droplets injected into the domain. As in Fig. 5.6, the droplets are coloured by their diameter. Note that breakup pattern observed for Jet A is quite different from that observed for n-dodecane. This happens because both breakup time

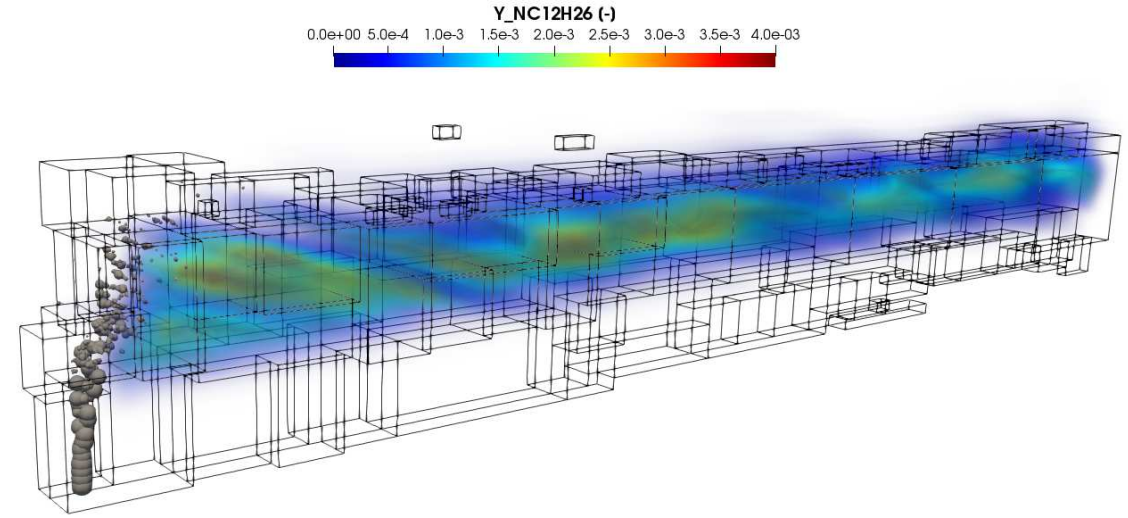

Figure 5.9: 3D visualisation of fuel vapour contours with the injected droplets scaled by their diameter and blocks indicating the computational mesh finest level for n-dodecane evaporation at $t = 5.0$ ms.

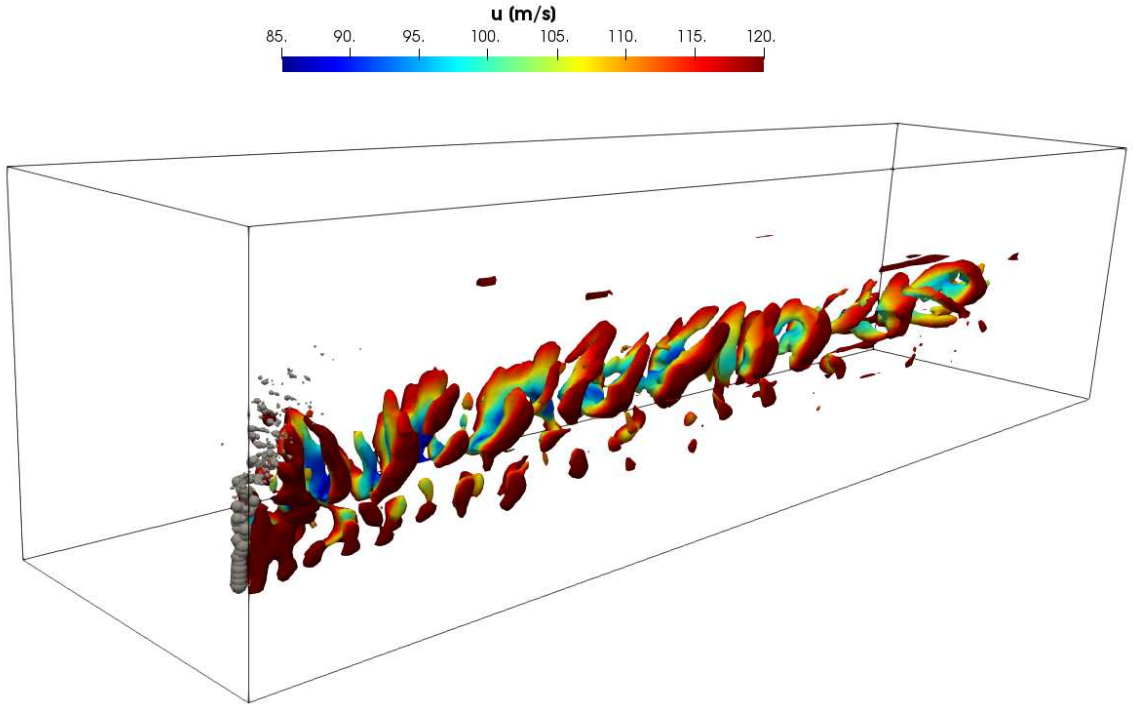

Figure 5.10: Turbulence structures shaped by isovalues of the $Q = 3 \times 10^6$ coloured by the component velocity on x direction for n-dodecane evaporation at $t = 5.0$ ms.

scale (t_d^{bu}) and critical radius ($R_{d,cr}$) parameters depend on liquid properties, such as viscosity, density, and surface tension. Furthermore, not only the parameters that decide whether the breakup event happens or not are influenced by the liquid properties, but also the parameters arising from the breakup event, namely child droplet radius ($R_{d,child}$) and velocity (u_d^{bu}).

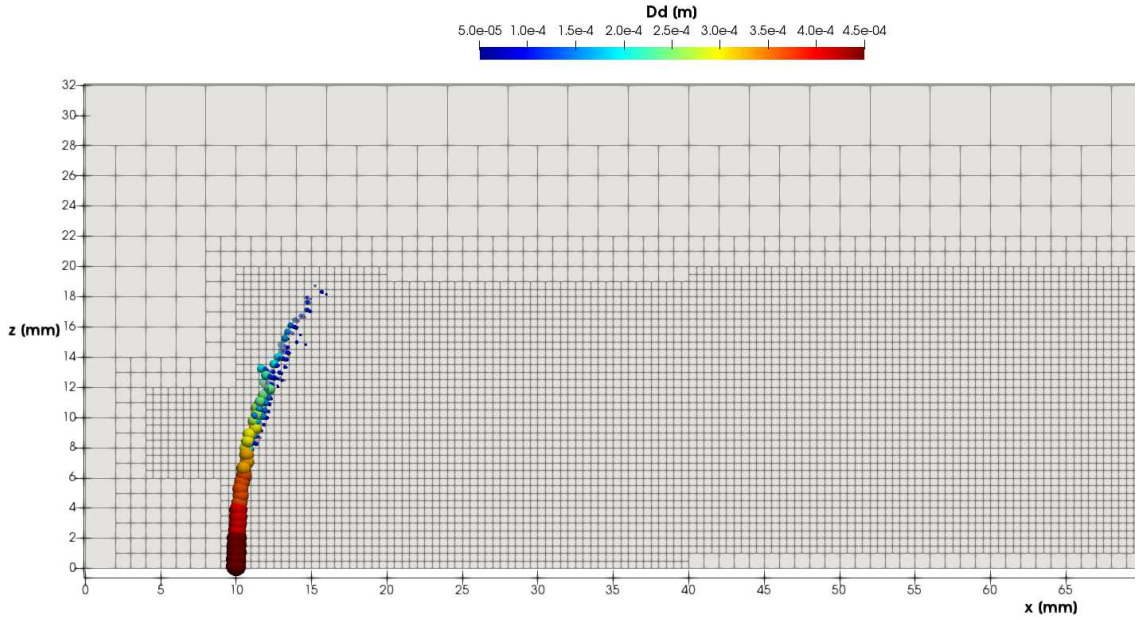

Figure 5.11: Computational mesh with droplets coloured their diameter for Jet A evaporation at $t = 5.0$ ms.

In Fig. 5.12, the ambient gas temperature distribution in a mid plane at $y = 16$ mm is shown. The same behaviour observed in Fig. 5.7 is seen here, but the temperature reduction for Jet A is more pronounced, reaching a minimum value of 1007 K near the liquid column. This happens because the droplets generated by the breakup events are so small that they quickly evaporate without being carried by the flow.

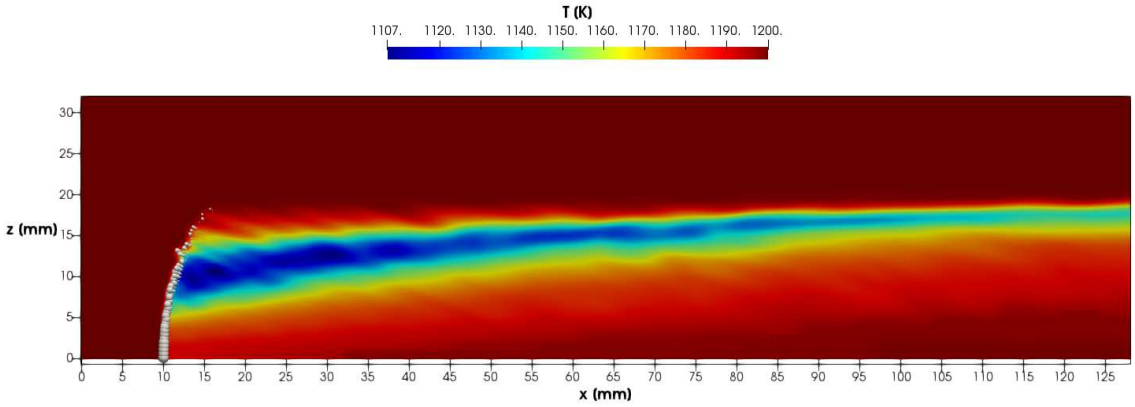

Figure 5.12: Contours of gas temperature in a mid plane for Jet A evaporation at $t = 5.0$ ms.

In Fig. 5.13, the mass fraction distribution of nitrogen and vapour fuel in a mid plane at $y = 16$ mm is shown. Note that Y_{fuel} represents the sum of the nine components considered in Surrogate 11. The same behaviour observed in Fig. 5.8 is seen here, but since Surrogate 11 has

components lighter than n-dodecane, these components tend to evaporate quicker. Therefore, fuel mass fraction achieves higher values here than for monocomponent evaporation.

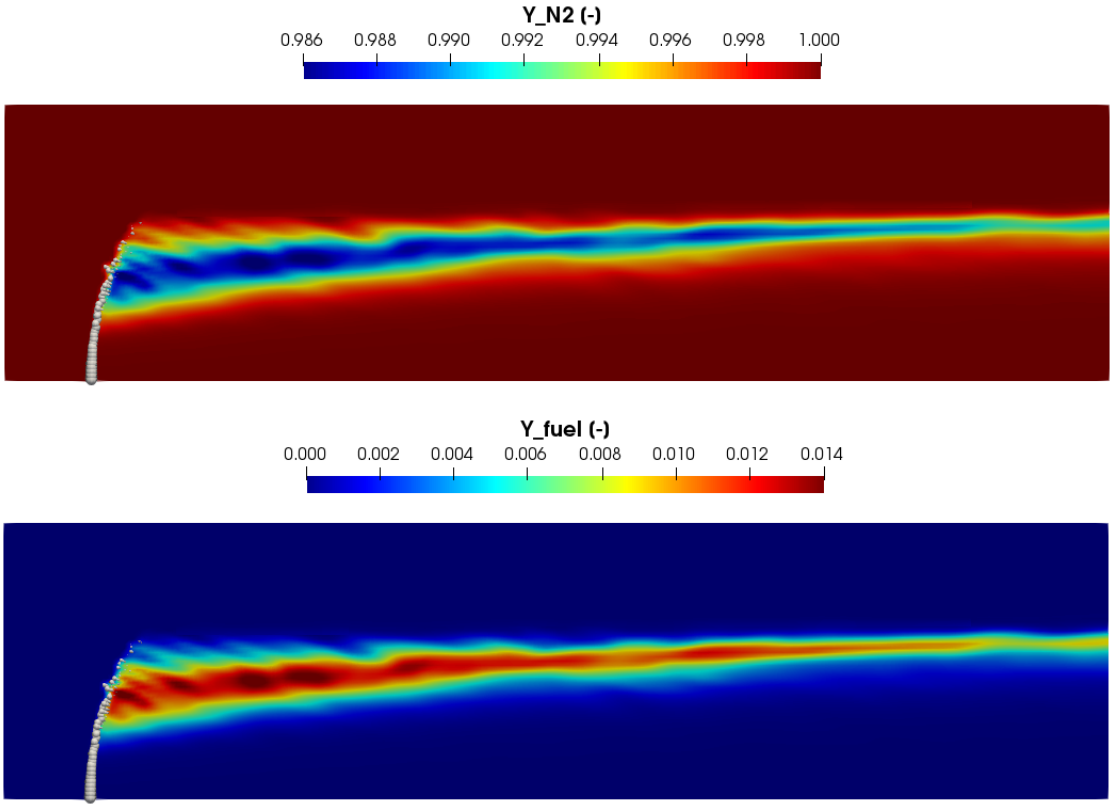

Figure 5.13: Contours of nitrogen and fuel vapour in a mid plane for Jet A evaporation at $t = 5.0$ ms.

In Fig. 5.14, the mass fraction distribution of each individual component of Surrogate 11 in z direction at $x = 32$ mm and $y = 16$ mm is presented. It can be noticed that two aspects determine the evaporated mass of each component: their volatility, which is a physical property, and their availability considering the liquid composition (see Eq. (3.9)). Note that the non-symmetry observed in the curves from Fig. 5.14 is justified by the bulk crossflow. In order to facilitate the understanding of this part, two histograms were created, which are shown in Fig. 5.15. The first histogram represents the liquid initial composition, based on Surrogate 11 composition as seen in Table 5.2. From it, it can be observed that n-dodecane (NC12H26) is the component with the highest contribution for the composition, followed by 1,3,5-trimethylbenzene (C9H12). The second histogram, on the other hand, represents the vapour composition computed by integrating the area below the curves displayed in Fig. 5.14. Even though there is more NC12H26 available in Surrogate 11 initial liquid composition, C9H12 is the main component

in the vapour composition. This happens because C9H12 is more volatile than NC12H26, as concluded from the vapour pressure column of Table 5.2.

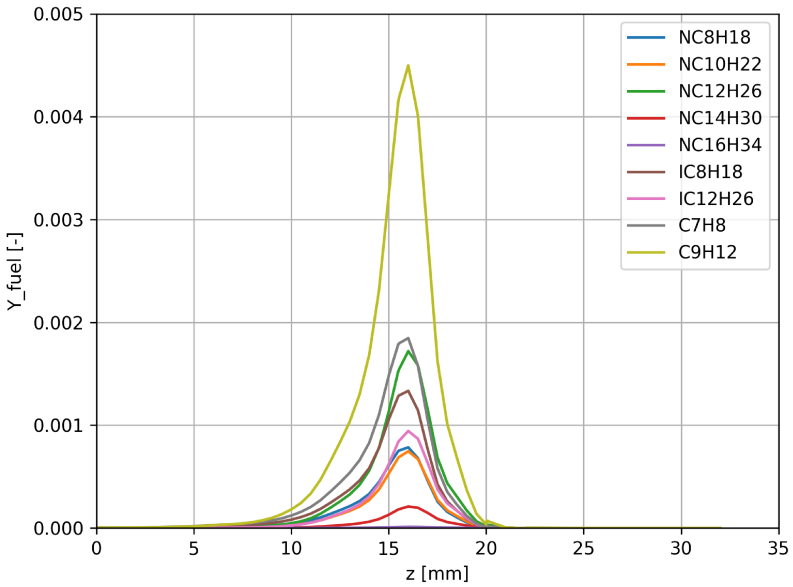

Figure 5.14: Mass fraction distribution of each one the nine components of Surrogate 11 in z direction at $x = 64$ mm and $y = 16$ mm at $t = 5.0$ ms.

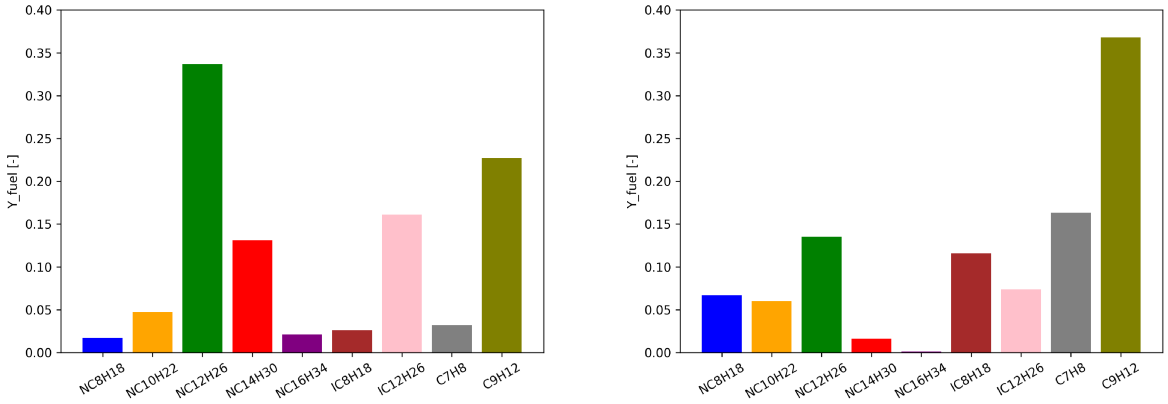

(a) Surrogate 11 initial liquid composition

(b) Vapour composition from Fig. 5.14

Figure 5.15: Histograms of liquid initial composition and vapour composition both in terms of mass fraction.

5.2.2 Liquid jet injection in quiescent environment

5.2.2.1 Geometry and computational details

The implemented models are now tested considering a high-speed liquid jet of fuel sprayed into a chamber filled with stagnant nitrogen at high temperature. The injector is a single hole

Parameter	Value
Gas pressure p_g [atm]	10.0
Gas temperature T_g [K]	1200.0
Liquid mass flow rate $\dot{m}_l$ [g/s]	30.0
Droplet diameter $D_{d,0}$ [μm]	300.0 $\pm$ 50.0
Droplet temperature $T_{d,0}$ [K]	300.0
Droplet injection velocity $u_{d,0}$ [m/s]	150.0
Injection orifice diameter D_{inj} [mm]	1.5
We_g [-]	774
Oh_l [-]	0.018

Table 5.5: Test case conditions for jet injection in quiescent environment simulation.

nozzle with orifice diameter of 1.5 mm in which liquid droplet are injected, with droplet size distribution following a log-normal law. Other information referring to ambient gas conditions and injection parameters are displayed in Table 5.5. We_g and Oh_l at injection indicate that the disintegration of the liquid takes place in a catastrophic breakup mode.

The computational domain consists of a rectangular box with a length of 256 mm and sides of 64 mm, while the nozzle is placed in the centre of the most upstream transversal section of this domain. Therefore, spray penetration is observed in the x direction. A sketch of the domain geometry is provided in Fig. 5.16.

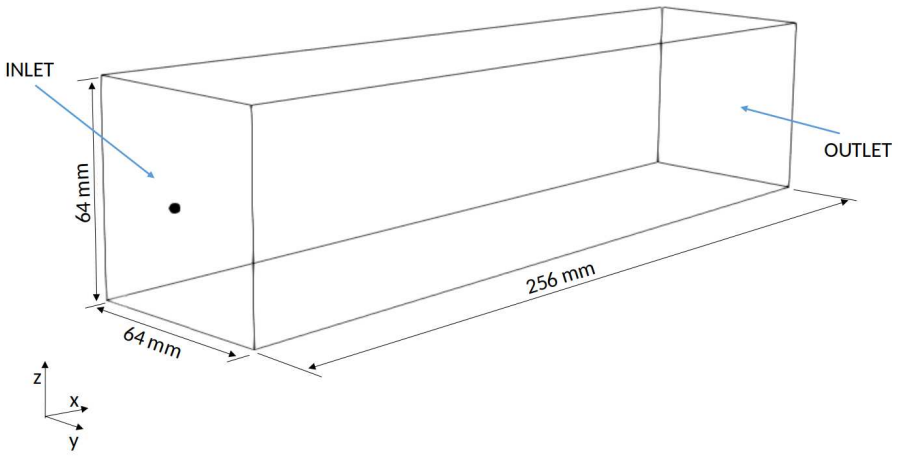

Figure 5.16: View of the computational domain, where the black circle denotes the location of the injection point.

The computational domain is discretised considering an adaptive mesh with 3 levels of refinement and base level composed of $64 \times 16 \times 16$ hexaedric cells, in x, y and z directions, respectively. Vorticity, particle presence and temperature gradient are considered as criteria to

determine where the mesh is refined. As for the domain boundary conditions, where it is neither inlet nor outlet in Fig. 5.16, the free-slip condition is applied. Furthermore, the CUBISTA scheme is used for convection and the dynamic Smagorinsky model for turbulence closure. Other information referring to numerical parameters are similar to those presented in Table 5.4.

5.2.2.2 Results and discussion

Only results for Jet A evaporation are presented here, since the differences between n-dodecane and Jet A evaporation observed for this test case are similar to those reported for the crossflow case. Furthermore, in this section focus is given to showing more detailed aspects of the Lagrangian phase.

Figs. 5.17 and 5.18 show the ambient gas temperature distribution, mass fraction distribution of nitrogen, and mass fraction distribution of vapour fuel in a mid plane at $y = 32$ mm. The same behaviour as observed in Fig. 5.11 is seen here, such as temperature reduction, fuel vapour concentration increase and fuel vapour mixing. Note that the energy reduction is more pronounced in the centre line in x direction ($y = 32$ mm and $z = 32$ mm), where droplets are injected. Since temperature decreases in this line, evaporation becomes less dominant. In fact, droplets tend to evaporate more as they are further away of the centre line in the radial direction, as noticed in Fig. 5.18 by mass fraction distribution of vapour fuel. This happens because there is more energy available in this region and the droplets are smaller, since they are in fact child droplets originated from breakup events. Once these child droplets are created, they gain an additional velocity component (u_d^{bu}) in radial direction.

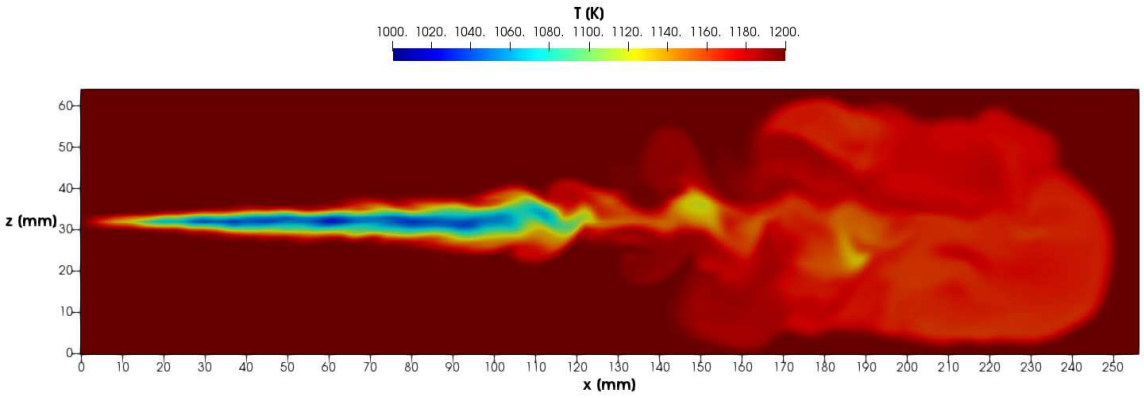

Figure 5.17: Contours of gas temperature in a mid plane for Jet A evaporation at $t = 30.0$ ms.

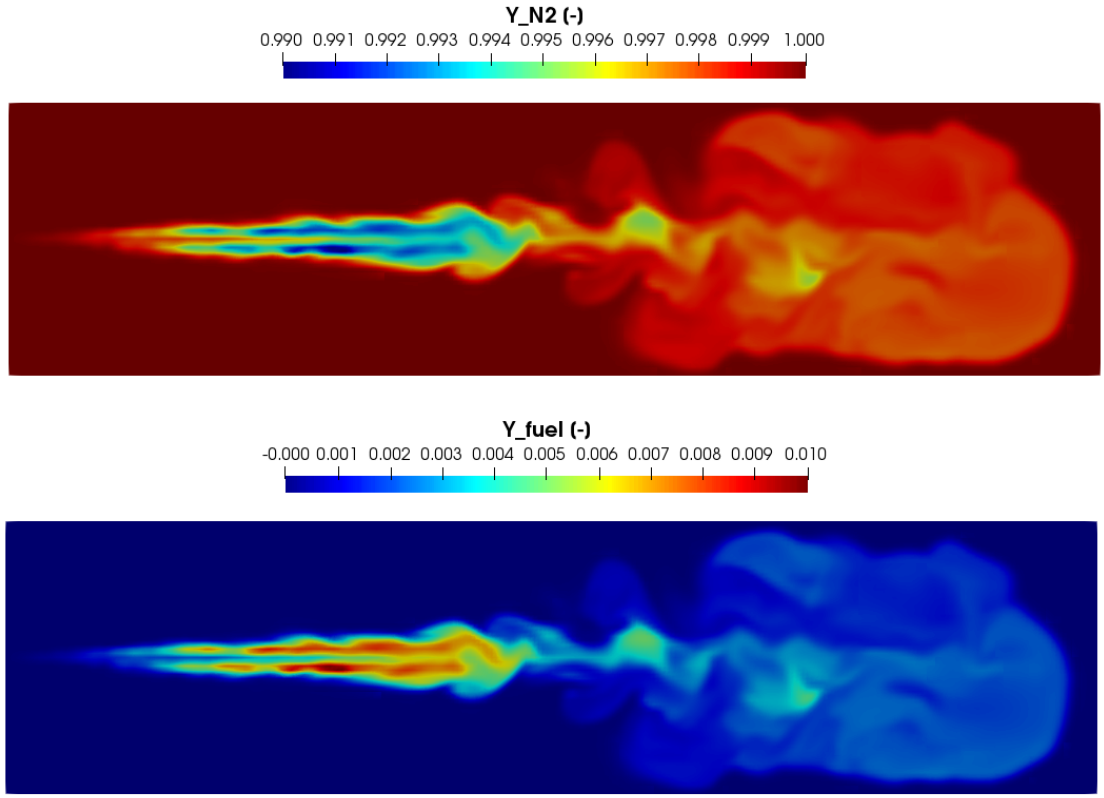

Figure 5.18: Contours of nitrogen and fuel vapour in a mid plane for Jet A evaporation at $t = 30.0$ ms.

Fig. 5.19 shows the droplets average temperature (T_d), energy transfer term (S_{energy}) and mass transfer term (S_{mass}). Note that S_{energy} takes into account both sensible and latent heat, and $S_{mass} = -\dot{m}_d$, in which the evaporated mass of all nine components is included. Also, S_{energy} and S_{mass} represent the contribution of each individual droplet. For computing ${S_{c_pT}}^L$ and ${S_m}^L$, the contribution of all the droplets inside a certain Eulerian cell is added up and then divided by the Eulerian cell volume, as explained before in Section 2.1.3. In Fig. 5.19(a), it can be observed that droplets are injected with $T_{d,0} = 300.0$ K and they are heated once in contact with the ambient hot gas. In Fig. 5.19(b), it is seen that droplets with lower temperature receive a higher amount of energy S_{energy}, since the temperature difference ($T_g - T_d$) is greater. Note that the amount of energy transferred from the ambient gas to the liquid droplet depends not only on the temperature difference, but also on the droplet size. Bigger droplets receive more energy, because of their higher surface area. Finally, in Fig. 5.19(c), it is noticed that when the droplets start being heated the largest share of the energy is received as sensible heat. Just later it is received as latent heat, representing an increase in S_{mass}.

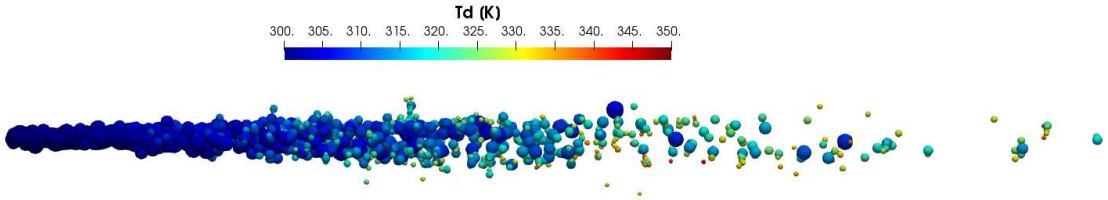

(a) Average droplet temperature

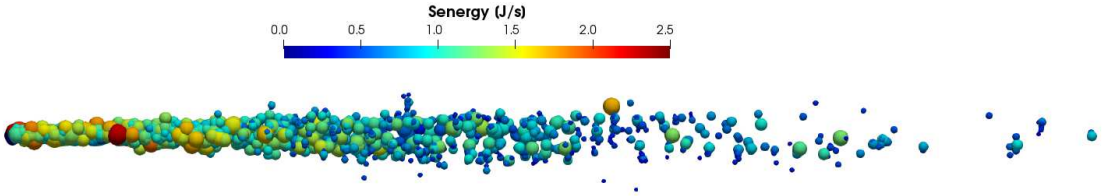

(b) Droplet energy transfer term, in which positive values represent that the liquid droplets are receiving energy in heat form from the ambient gas

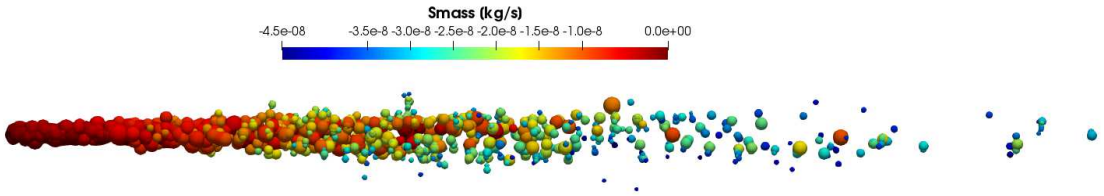

(c) Droplet mass transfer term, in which negative values represent that the liquid droplets are giving mass in vapour form to the ambient gas

Figure 5.19: Lagrangian phase parameters for Jet A evaporation at $t = 30.0$ ms.

5.3 Evaluation of droplet heating and evaporating models

When dealing with microsized droplets, the finite thermal conductivity and finite species diffusivity inside droplets has been ignored in most studies in order to reduce model complexity and computational cost. However, the importance of considering temperature and concentration gradients inside droplets has already been advertised in many studies (AL-QUBEISSI *et al.*, 2021). This section is dedicated to evaluating the impact of considering temperature and concentration gradients by means of a parametric analysis. Since the main interest in this section is in understanding droplet heating and evaporating models, the test case chosen do not include droplet breakup.

5.3.1 Geometry and computational details

The test case used in this section simulates the injection of a liquid jet perpendicularly to a gaseous crossflow of nitrogen at high temperature. Two ambient gas temperatures are considered in the simulations: T_g = 600 K, which is lower than Jet A boiling temperature at p_g = 10 atm, and T_g = 1200 K, which is higher than Jet A boiling temperature at p_g = 10 atm. The computational domain consists of a rectangular box with a length of 64 mm and sides of 8 mm, as seen in Fig. 5.20. The gaseous bulk flow is the x direction, while the liquid injection happens in the z direction. The liquid injection point is located 5 mm downstream the air inlet. Considering the air is injected with 30 m/s and the channel width is 8 mm, the flow Reynolds number is 4.62×10^4 for T_g = 600 K, and 1.45×10^4 for T_g = 1200 K. Other information referring to ambient gas conditions and injection parameters are displayed in Table 5.6. Additionally, We_g is 11.5 for T_g = 600 K and 5.7 for T_g = 1200 K, and Oh_l is 0.04 for both gas temperatures at injection. This indicates that, as expected, droplets do not atomise, since $We_g < We_{cr}$.

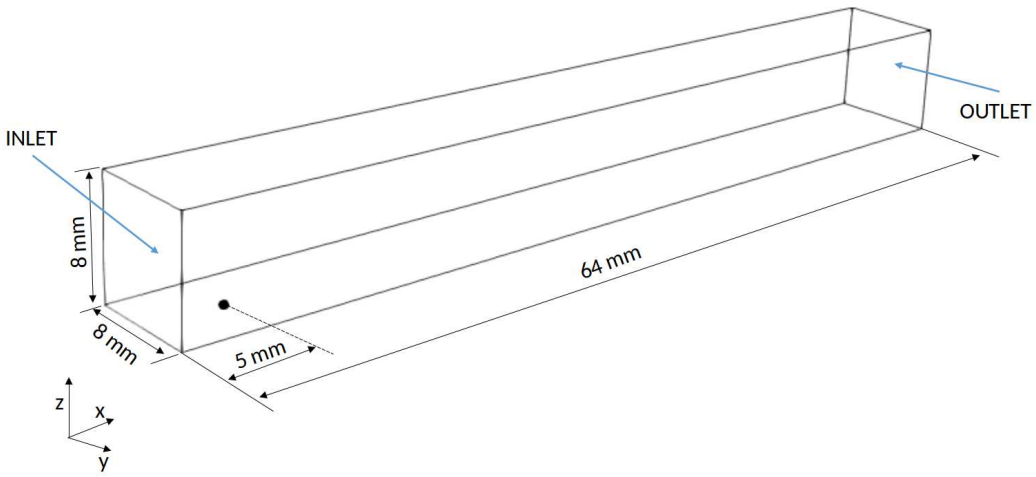

Figure 5.20: View of the computational domain, where the black circle in which the coordinates are denotes the location of the injection point.

The computational domain is discretised considering an adaptive mesh with 3 levels of refinement and base level composed of $64 \times 8 \times 8$ hexaedric cells, in x, y and z directions, respectively. Vorticity, particle presence and temperature gradient are considered as criteria to determine where the mesh is refined. As for the domain boundary conditions, where it is neither inlet nor outlet in Fig. 5.20, the free-slip condition is applied. Furthermore, the CUBISTA scheme is used for convection and the dynamic Smagorinsky model for turbulence closure. Other

Parameter	Value
Gas pressure p_g [atm]	10.0
Gas temperature T_g [K]	600.0 / 1200.0
Gas bulk velocity u_g [m/s]	30.0
Liquid mass flow rate $\dot{m}_l$ [g/s]	2.44×10^{-5}
Droplet diameter $D_{d,0}$ [μm]	50.0
Droplet temperature $T_{d,0}$ [K]	300.0
Droplet injection velocity $u_{d,0}$ [m/s]	10.0

Table 5.6: Test case conditions for jet injection in in gaseous crossflow simulation.

Parameter	Value
Number of layers n_{layers} [-]	50
Time step Δt [s]	1×10^{-6}
Bisection method accuracy α_{BSM} [-]	10^{-12}
Number of eigenvalues for temperature n_T [-]	20
Number of eigenvalues for species diffusion n_Y [-]	20

Table 5.7: Numerical parameters for jet injection in quiescent environment simulation.

information referring to numerical parameters are in Table 5.7.

5.3.2 Results and discussion

First, it was verified that stochastic breakup model is properly working for this test case, because even when it is activated in the MFSim code, droplets do not atomise. Therefore, it could be deactivated just to avoid extra unnecessary computational cost.

Four different tests were simulated. The first two tests considered monocomponent droplets composed by n-dodecane and either ITC (called ITCmono from now on) or ETC models were applied. The last two tests considered multicomponent droplets of Jet A by using Surrogate 11 and either ITC (called ITCmulti from now on) or ETC-ED models were applied. Note that if ITC model is applied, no gradient is computed inside droplets. In other words, it is assumed uniform temperate and uniform species concentration. Even though, ITCmono takes into account droplet temperature variation throughout time, ITCmulti does not take into account species concentration variation, maintaining Surrogate 11 initial composition.

Ambient gas temperature distribution in a mid plane at $y = 4$ mm for all the four tests is presented in Fig. 5.21 for $T_g = 600$ K and in Fig. 5.22 for $T_g = 1200$ K. The same tendency of temperature reduction previously mentioned is observed here. For both monocomponent and

multicomponent cases, it is noticed that when temperature gradient is not taken into account (ITC model) the temperature reduction is even more significant. This happens because, as seen in Section 5.1, droplet average temperature increases more quickly in ITC, resulting in higher ${S_{c_pT}}^L$. Furthermore, the difference between considering or not temperature gradient has a higher impact in ambient gas temperature distribution for higher temperatures.

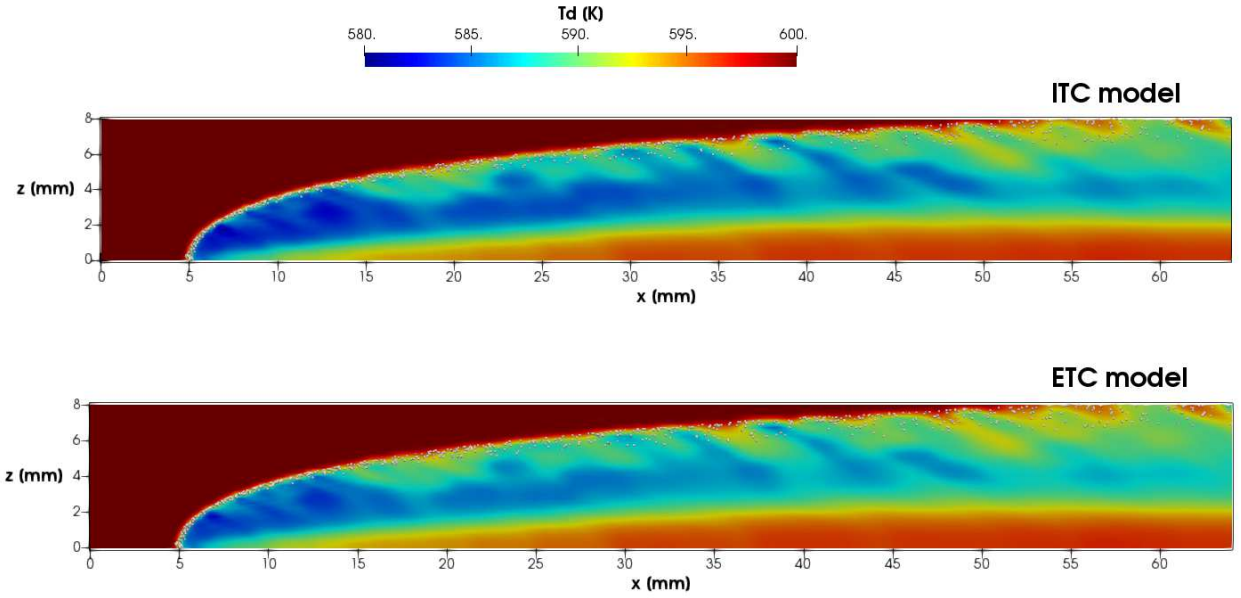

(a) n-dodecane evaporation

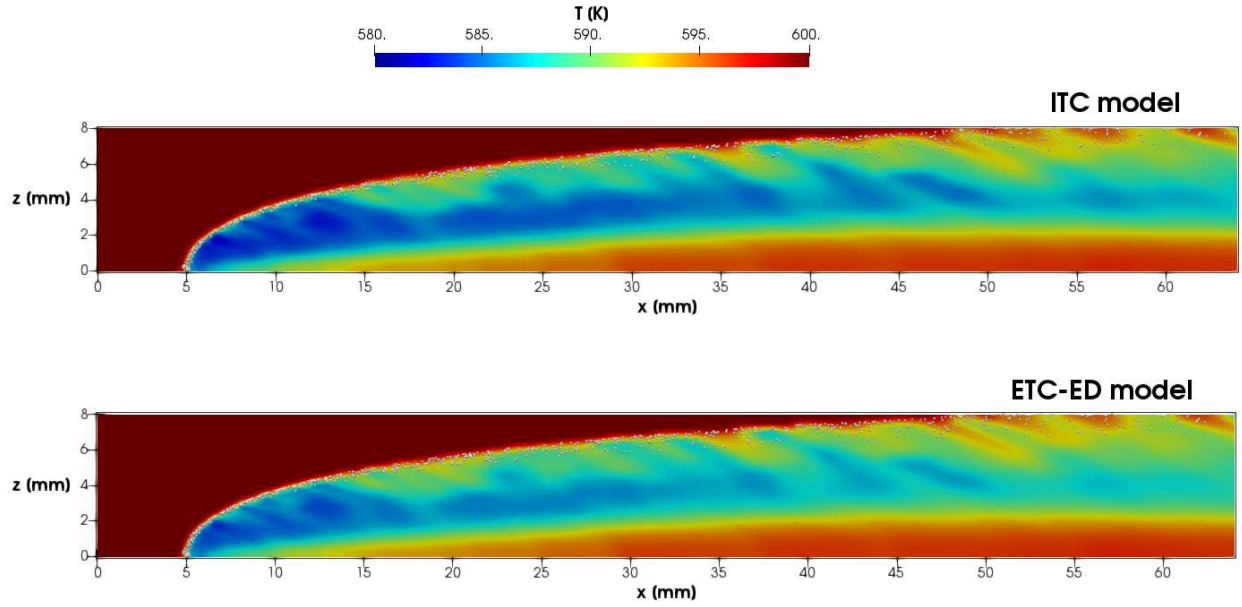

(b) Jet A evaporation

Figure 5.21: Contours of gas temperature in a mid plane for $T_g = 600$ K at $t = 7.5$ ms.

Mass fraction distribution of vapour fuel in a mid plane at $y = 4$ mm for all the four tests is presented in Fig. 5.23 for $T_g = 600$ K and in Fig. 5.24 for $T_g = 1200$ K. The same tendency of

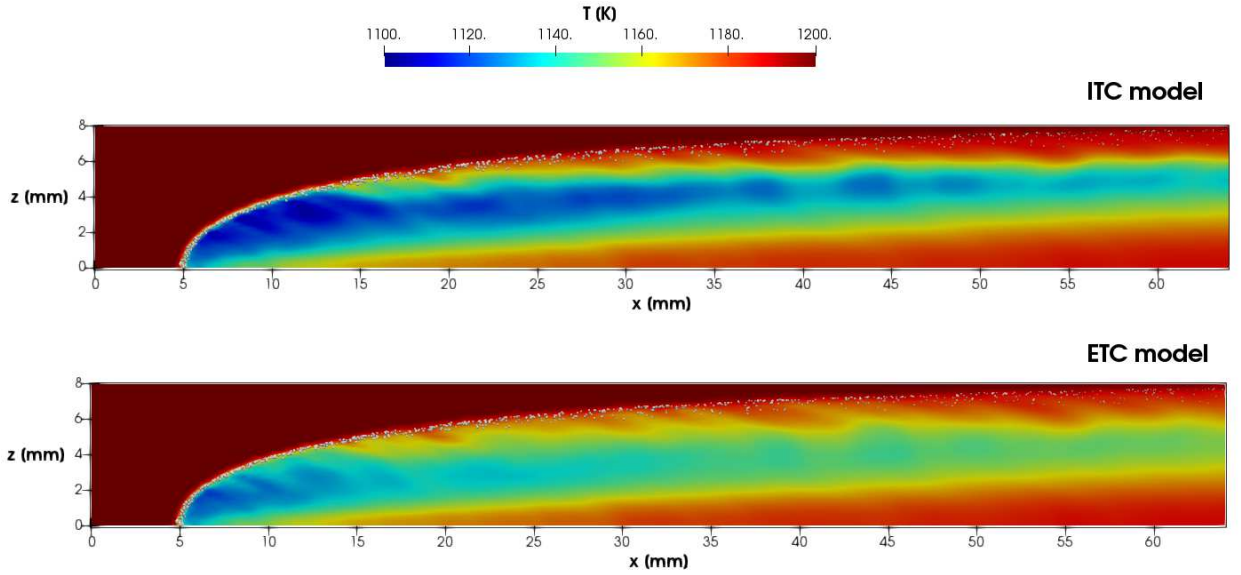

(a) n-dodecane evaporation

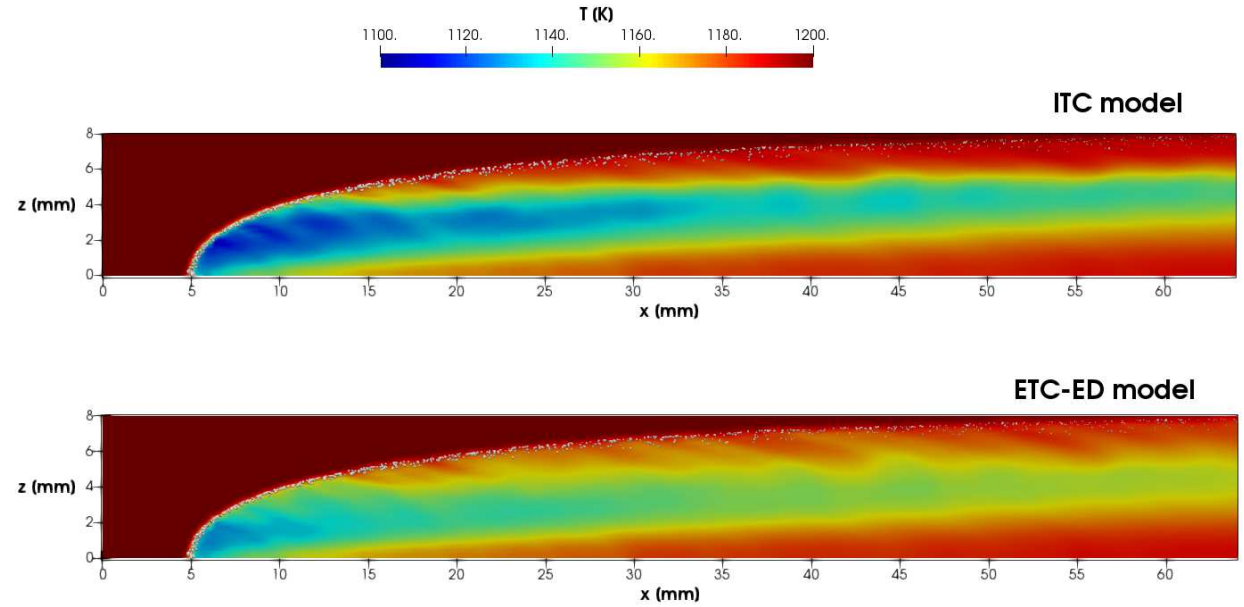

(b) Jet A evaporation

Figure 5.22: Contours of gas temperature in a mid plane for $T_g = 1200$ K at $t = 7.5$ ms.

fuel vapour concentration growth previously mentioned is observed here. For $T_g = 600$ K, there is not a noticeable difference between considering or not gradients inside the droplet in fuel vapour concentration for both monocomponent and multicomponent cases. ITCmono and ETC cases presented similar results. When gradients inside the droplet are taken into account (ETC and ETC-ED models), droplets tend to start evaporating earlier. This happens because, as seen in Section 5.1, droplet surface temperature increases more quickly in ETC, resulting in higher ${S_m}^L$. Multicomponent simulations present a higher evaporation rate in comparison to monocomponent

ones due to the existence of components lighter than n-dodecane in Surrogate 11 composition. Furthermore, the difference between considering or not gradients inside the droplet has a higher impact in fuel vapour mass fraction distribution for higher temperatures.

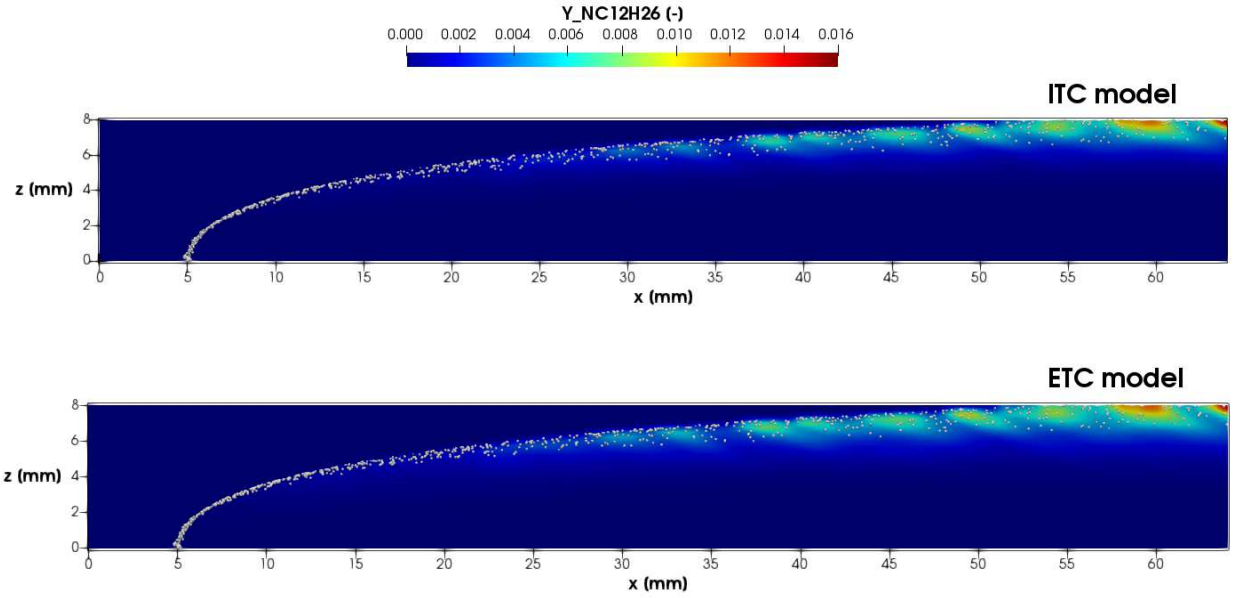

(a) n-dodecane evaporation

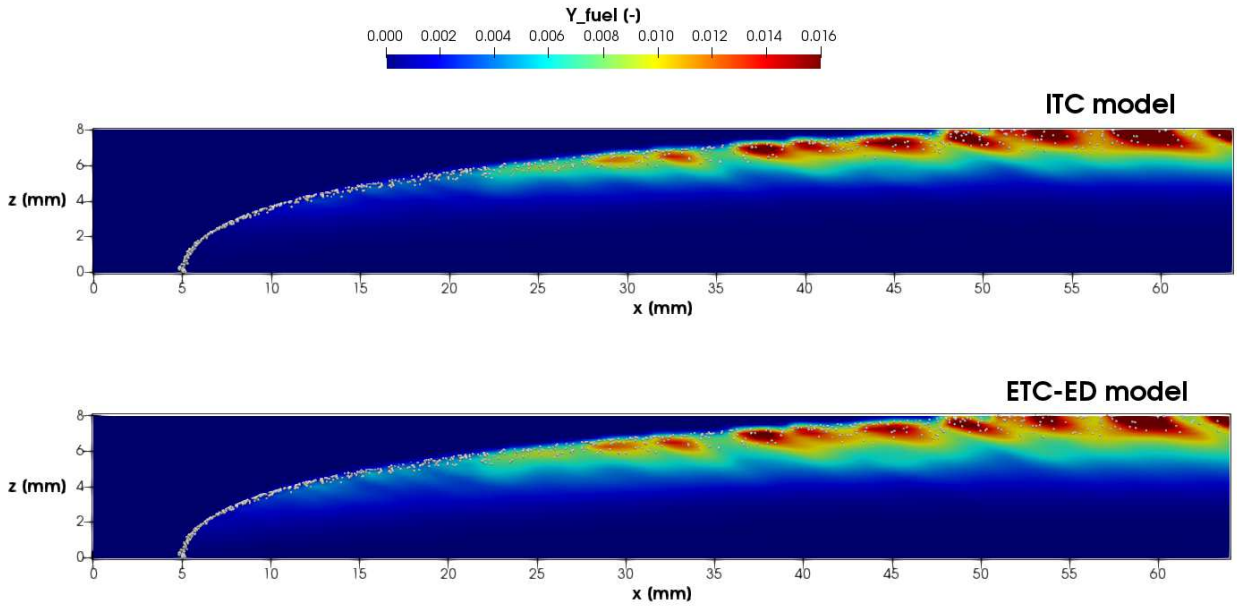

(b) Jet A evaporation

Figure 5.23: Contours of fuel vapour in a mid plane for $T_g = 600$ K at $t = 7.5$ ms.

Fig. 5.25 shows contours of the two main components in Surrogate 11, namely n-dodecane (NC12H26) and 1,3,5-trimethylbenzene (C9H12), for $T_g = 600$ K and $T_g = 1200$ K. Even though there is more NC12H26 available in Surrogate 11 initial liquid composition, it is observed

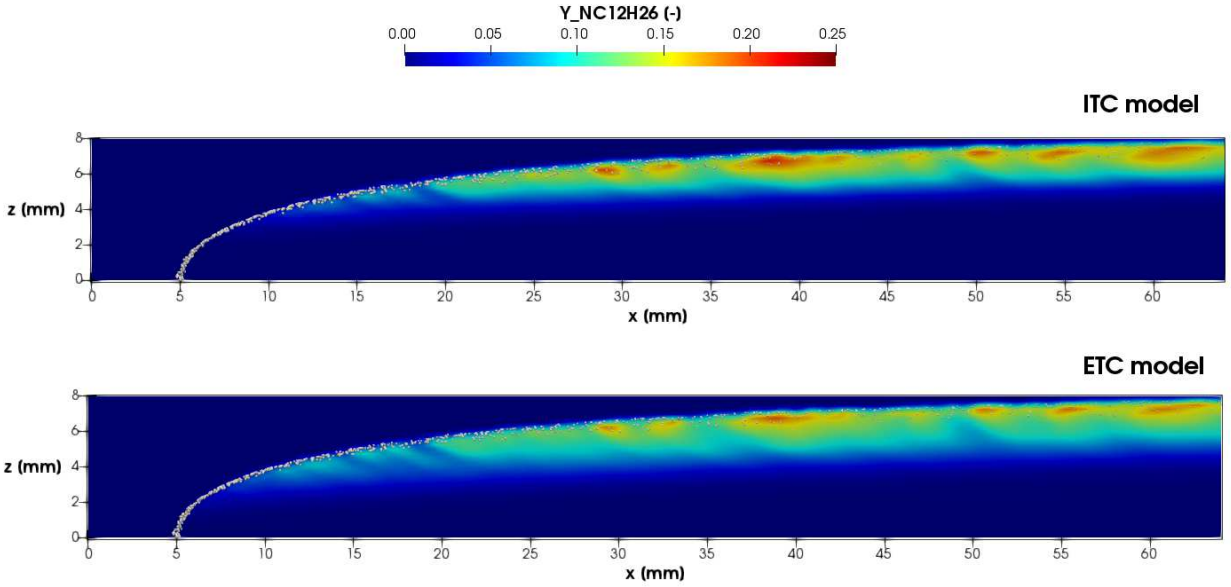

(a) n-dodecane evaporation

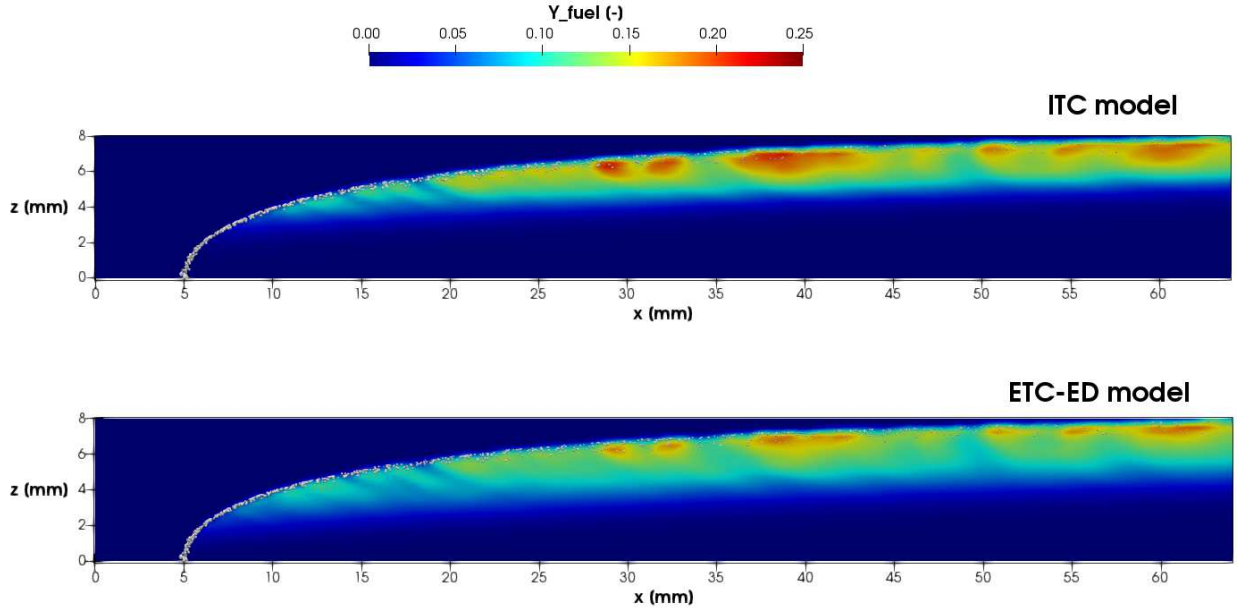

(b) Jet A evaporation

Figure 5.24: Contours of fuel vapour in a mid plane for $T_g = 1200$ K at $t = 7.5$ ms.

a higher concentration of C9H12 for $T_g = 600$ K at $t = 7.5$ ms. This happens because C9H12 is more volatile than NC12H26. For $T_g = 1200$ K, on the other hand, both components present concentrations with similar order of magnitude. For this higher temperature scenario, droplets have reached a higher temperature, resulting with a higher evaporation rate of NC12H26 than observed for the lower temperature scenario. In some regions, the concentration of NC12H26 is even higher than the one of C9H12. But it can be observed in Fig. 5.25(b) that C9H12

evaporation starts first due its higher volatility. In order to verify the better understand the impact of availability and volatility on vapour concentration, the evolution of NC12H26 and C9H12 vapour contours over time is presented in Fig. Fig. 5.26. At first, for $t = 1.0$ ms, C9H12 presented a higher concentration in comparison to NC12H26. Only for $t = 3.0$ ms NC12H26 concentration achieved higher values, especially in the regions near the domain outlet, where the droplets presented the higher temperature.

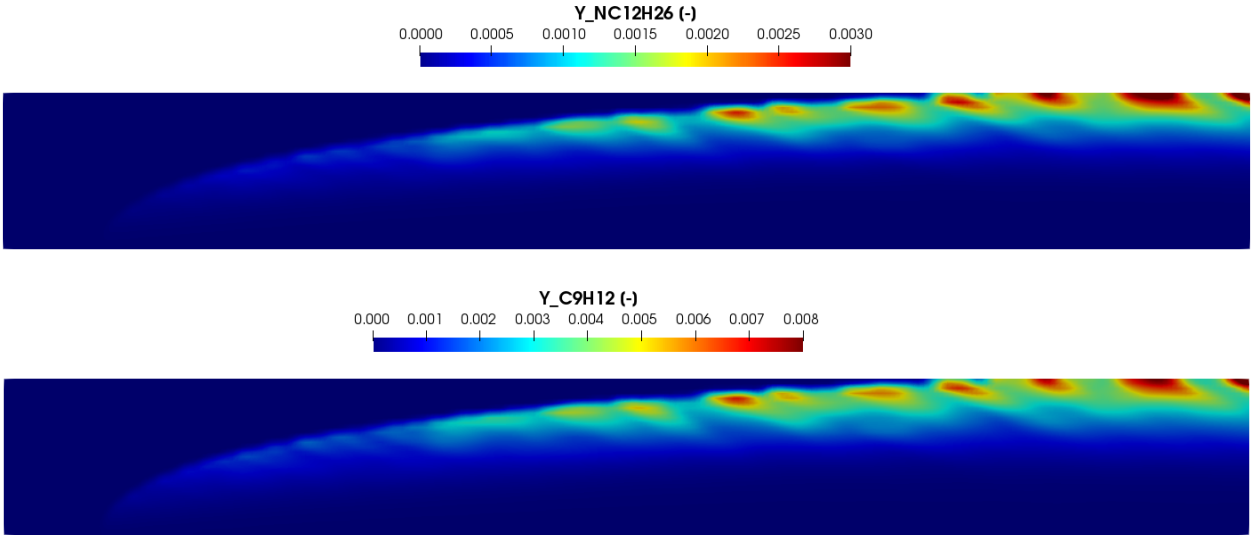

(a) $T_g = 600$ K

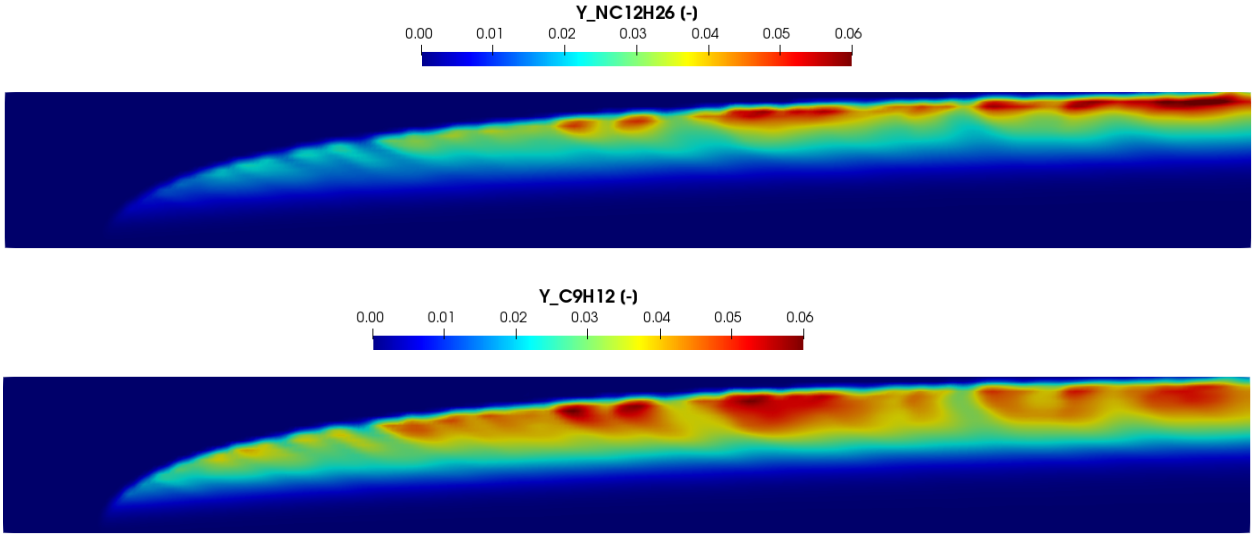

(b) $T_g = 1200$ K

Figure 5.25: Contours of n-dodecane and 1,3,5-trimethylbenzene vapour in a mid plane at $t = 7.5$ ms.

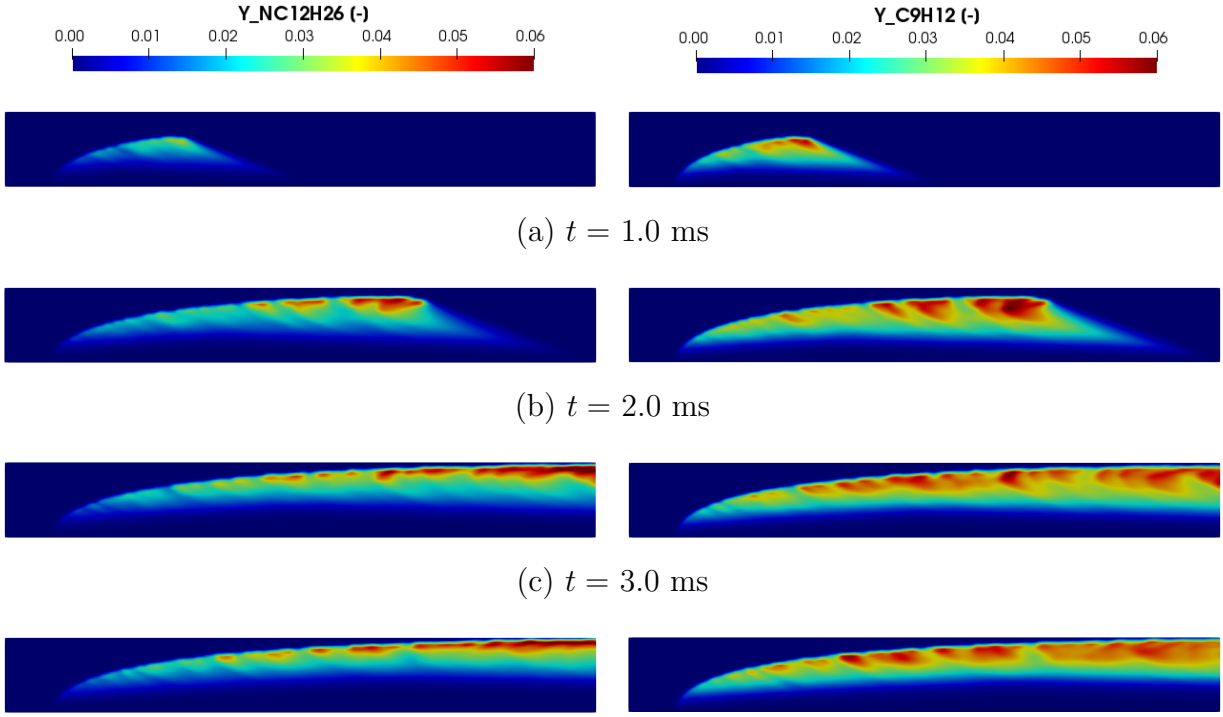

(a) $t = 1.0$ ms

(b) $t = 2.0$ ms

(c) $t = 3.0$ ms

(d) $t = 4.0$ ms

Figure 5.26: Temporal evolution of n-dodecane and 1,3,5-trimethylbenzene vapour distributions in a mid plane for $T_g = 1200$ K.

Fig. 5.27 displays the evolution of SMD and droplet average temperature along the spray axis x. Both parameters obtained from an average of the droplet diameters and temperatures in transversal slices of 2 mm thickness. For $T_g = 600$ K, it can be seen that the thermal swelling effect is more pronounced when using ITC for both monocomponent and multicomponent cases, and that Jet A droplets evaporate faster than n-dodecane ones due to the existence of lighter components than n-dodecane in Surrogate 11 composition. Considering the droplet temperature, all models presented a similar behaviour for $T_g = 600$ K. Note that for this lower temperature scenario, droplets leave the domain while they are still being heated, so they have not reached a plateau temperature yet. For $T_g = 1200$ K, thermal swelling is also more evident when considering ITCmono, but as the evaporation process evolves ITCmono predicts a lower droplet lifetime in comparison to ETC, as expected. This same tendency occurs when considering multicomponent droplets. Additionally, even though a similar behaviour is noticed in Fig. 5.27 for ETC and ETC-ED, tending to almost the same value at the end of the domain, it is important to highlight that the monocomponent simplification impacts the computation of the gaseous ambient composition.

Now, the computational cost of each one of the four models considered in this section is

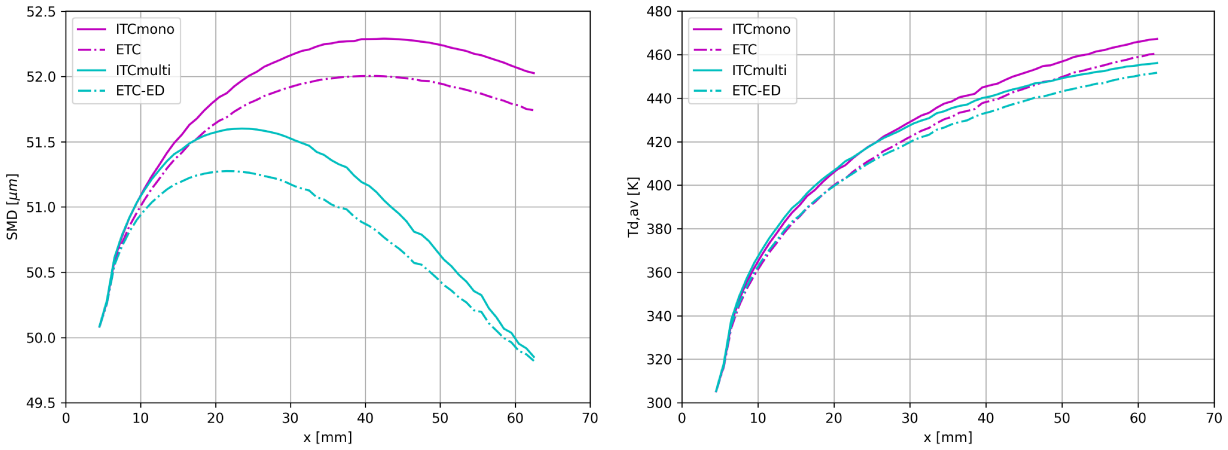

(a) $T_g = 600$ K

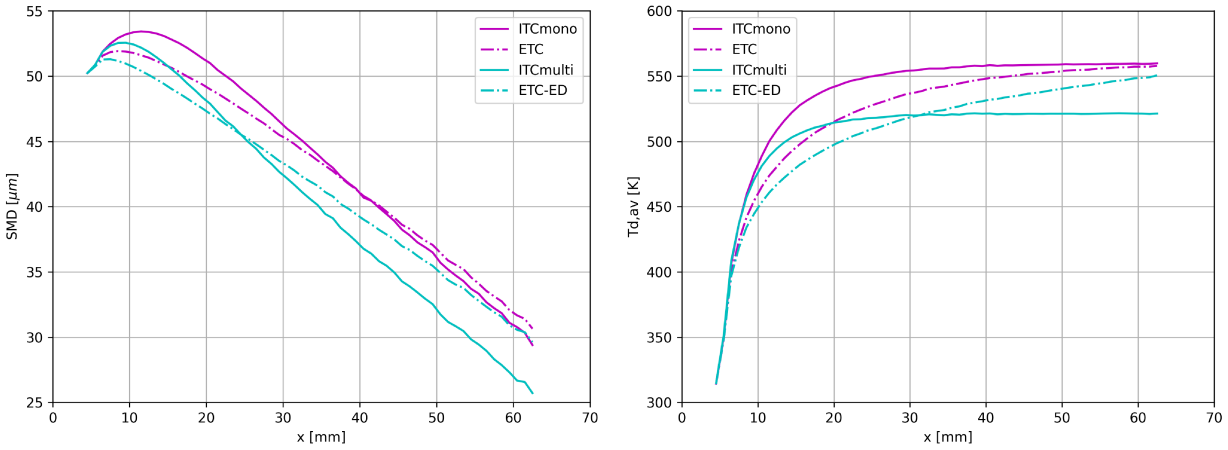

(b) $T_g = 1200$ K

Figure 5.27: Evolution of droplet Sauter Mean Diameter (SMD) and droplet average temperature (Td,av) in x direction at $t = 7.5$ ms.

evaluated by means of the Reduced Computational Time (RCT) parameter (SACOMANO FILHO *et al.*, 2020):

$$\text{RCT} = \frac{\text{Elapsed time} \times \text{Number of CPUs}}{\text{Number of cells} \times \text{Number of timesteps}}. \tag{5.1}$$

For this part, an Intel(R) Core(TM) i7-1065G7 CPU @ 1.30GHz processor with a 100 MHz clock was used and the elapsed time was measured as the execution time required to run 1000 time steps. From the results presented in Table 5.8, it can be concluded that what mostly increases the computational cost is not solving the gradients inside droplet, but increasing the number of species transported in the Eulerian phase. From ITCmono, the most simple model, to ETC-ED,

Model	Elapsed time [s]	N CPUs	N cells	N time steps	RCT [s]
ITCmono	311.90	4	101233	1000	1.23×10^{-5}
ETC	344.40	4	99931	1000	1.38×10^{-5}
ITCmulti	828.69	4	100255	1000	3.31×10^{-5}
ETC-ED	876.25	4	98025	1000	3.58×10^{-5}

Table 5.8: Computational cost of each model in terms of RCT.

the most complex one, RCT increases 2.9 times.

CHAPTER VI

CONCLUSIONS AND OUTLOOK

The main contributions of this research are related to multicomponent evaporation. First, it focused on deeply understanding Jet A heating and evaporation processes and reducing the computational cost of numerical simulations by using surrogates instead of the fuel complete composition. This strategy has shown promising results, revealing that Surrogate 11, from Won *et al.* (2017), is the one which best reproduced Jet A heating and evaporation behaviour.

Considering the MFSim code, the Abramzon-Sirignano model was generalised for multicomponent evaporation and new models for solving temperature and concentration distributions inside droplets were implemented into the code. The models implemented were validated against available experimental results considering the evaporation of a single droplet of aviation fuel. Additionally, a hybrid deterministic-stochastic secondary breakup model was included into the MFSim code. Its implementation is validated using a benchmark case of a non-evaporating spray by comparison of both spray penetration and Sauter Mean Diameter (SMD) with experimental data. Including these models for droplet atomisation, heating and evaporation into the MFSim code enables a wide range of simulations for future applications.

Computational simulations of high-speed evaporating sprays considering both monocomponent and multicomponent droplets were performed. Different models either solving or not temperature and composition inside droplets were applied. Based on the modelling results obtained, it was possible to demonstrate the influence of the liquid composition on its breakup behaviour. Furthermore, by comparing the outcome from different models it was possible to

determine the importance of solving inside droplets, especially when dealing with high ambient temperature.

In the present research some simplifications have been adopted due to limitations in the thesis scope. Although the outcome was satisfying in view of the proposed objectives, some topics may be interesting for future research. These topics are listed below:

- Including radiation effect on the droplet heating model (ABRAMZON; SAZHIN, 2006);
- Including droplet collision/coalescence models (SOMMERFELD; KUSCHEL, 2016; KAMP; VILLWOCK; KRAUME, 2017);
- Including the volumetric effect of dispersed phase (CAPECELATRO; DESJARDINS, 2013; EVRARD; DENNER; WACHEM, 2019; PAKSERESHT; APTE, 2019);
- Using parabolic models (SNEGIREV, 2013) to solve the temperature distribution inside droplets as a way of reducing even more the computational cost;
- Using an auto-selection algorithm for choosing quasi-components as a way to generalise the selection of liquid fuel composition (AL-QUBEISSI; AL-ESAWI; SAZHIN, 2021);
- Implementing the Fully-Lagrangian method (LI; RYBDYLOVA, 2021) for spray modelling into the MFSim code.

BIBLIOGRAPHY

ABDUL-JAMEEL, A. G.; NASER, N.; EMWAS, A.-H.; SARATHY, S. M. Surrogate formulation for diesel and jet fuels using the minimalist functional group (MFG) approach. *Proceedings of the Combustion Institute*, v. 37, n. 4, p. 4663–4671, 2019. Available at: <https://doi.org/10.1016/j.proci.2018.09.035>.

ABRAMZON, B.; SAZHIN, S. Convective vaporization of a fuel droplet with thermal radiation absorption. *Fuel*, v. 85, n. 1, p. 32–46, 2006. Available at: <https://doi.org/10.1016/j.fuel.2005.02.027>.

ABRAMZON, B.; SIRIGNANO, W. A. Droplet vaporization model for spray combustion calculations. *International Journal of Heat and Mass Transfer*, v. 32, n. 9, p. 1605–1618, 1989. Available at: <https://doi.org/10.1016/0017-9310(89)90043-4>.

AL-QUBEISSI, M.; AL-ESAWI, N.; SAZHIN, S. S. Auto-selection of quasi-components/components in the multi-dimensional quasi-discrete model. *Fuel*, v. 294, p. 120245, 2021. Available at: <https://doi.org/10.1016/j.fuel.2021.120245>.

AL-QUBEISSI, M.; SAZHIN, S. S.; AL-ESAWI, N.; KOLODNYTSKA, R.; KHANAL, B.; GHALEEH, M.; ELWARDANY, A. Heating and evaporation of droplets of multicomponent and blended fuels: A review of recent modeling approaches. *Energy & Fuels*, ACS Publications, v. 35, n. 22, p. 18220–18256, 2021. Available at: <https://doi.org/10.1021/acs.energyfuels.1c02316>.

ALVES, M. A.; OLIVEIRA, P. J.; PINHO, F. T. A convergent and universally bounded interpolation scheme for the treatment of advection. *International Journal for Numerical Methods in Fluids*, v. 41, n. 1, p. 47–75, 2003. Available at: <https://doi.org/10.1002/fld.428>.

APTE, S.; GOROKHOVSKI, M.; MOIN, P. LES of atomizing spray with stochastic modeling of secondary breakup. *International Journal of Multiphase Flow*, v. 29, n. 9, p. 1503–1522, 2003. Available at: <https://doi.org/10.1016/S0301-9322(03)00111-3>.

ASHGRIZ, N. *Handbook of Atomization and Sprays: Theory and Applications*. [S.l.]: Springer Science & Business Media, 2011.

BAUMI, J.; BERTOSSE, C. M.; GUEDES, C. L. B. Aviation fuels and biofuels. In: AL-QUBEISSI, M.; EL-KHAROUF, A.; SOYHAN, H. S. (Ed.). *Renewable Energy*. Rijeka: IntechOpen, 2020. chap. 12. Available at: <https://doi.org/10.5772/intechopen.89397>.

BIRD, R. B.; LIGHTFOOT, E. N.; STEWART, W. E. *Transport Phenomena*. [S.l.]: Wiley, 2002.

BURGER, M.; SCHMEHL, R.; PROMMERSBERGER, K.; SCHÄFER, O.; KOCH, R.; WITTIG, S. Droplet evaporation modeling by the distillation curve model: accounting for kerosene fuel and elevated pressures. *International Journal of Heat and Mass Transfer*, v. 46, n. 23, p. 4403–4412, 2003. Available at: <https://doi.org/10.1016/S0017-9310(03)00286-2>.

CAPECELATRO, J.; DESJARDINS, O. An Euler–Lagrange strategy for simulating particle-laden flows. *Journal of Computational Physics*, v. 238, p. 1–31, 2013. Available at: <https://doi.org/10.1016/j.jcp.2012.12.015>.

CASTRO, L. P.; PINHEIRO, A. P.; VILELA, V.; MAGALHÃES, G. M.; SERFATY, R.; VEDOVOTTO, J. M. Implementation of a hybrid Lagrangian filtered density function–large eddy simulation methodology in a dynamic adaptive mesh refinement environment. *Physics of Fluids*, v. 33, n. 4, p. 045126, 2021. Available at: <https://doi.org/10.1063/5.0045873>.

CHORIN, A. J. Numerical solution of the navier-stokes equations. *Mathematics of Computation*, American Mathematical Society, v. 22, n. 104, p. 745–762, 1968. Available at: <https://doi.org/10.1090/S0025-5718-1968-0242392-2>.

CLIFT, R.; GRACE, J. R.; WEBER, M. E. *Bubbles, Drops, and Particles*. [S.l.]: Courier Corporation, 2005.

COLELLA, P.; PAO, K. A projection method for low speed flows. *Journal of Computational Physics*, v. 149, n. 2, p. 245–269, 1999. Available at: <https://doi.org/10.1006/jcph.1998.6152>.

CONTINILLO, G.; SIRIGNANO, W. Numerical study of multicomponent fuel spray flame propagation in a spherical closed volume. *Symposium (International) on Combustion*, v. 22, p. 1941–1949, 1989. Available at: <https://doi.org/10.1016/S0082-0784(89)80209-7>.

CROWE, C. T.; SHARMA, M. P.; STOCK, D. E. The Particle-Source-In Cell (PSI-CELL) model for gas-droplet flows. *Journal of Fluids Engineering*, v. 99, n. 2, p. 325–332, 06 1977. Available at: <https://doi.org/10.1115/1.3448756>.

CUMPSTY, N.; HEYES, A. *Jet Propulsion - A Simple Guide to the Aerodynamic and Thermodynamic Design and Performance of Jet Engines*. [S.l.]: Cambridge University Press, 2015.

DAGAUT, P.; CATHONNET, M. The ignition, oxidation, and combustion of kerosene: A review of experimental and kinetic modeling. *Progress in Energy and Combustion Science*, v. 32, n. 1, p. 48–92, 2006. Available at: <https://doi.org/10.1016/j.pecs.2005.10.003>.

DAMASCENO, M. M. R. *Desenvolvimento de uma modelagem para escoamentos reativos em malhas adaptativas do tipo bloco-estruturada*. Phd Thesis (PhD Thesis) — Universidade Federal de Uberlândia, 2018. Available at: <https://doi.org/10.14393/ufu.te.2018.771>.

DAMASCENO, M. M. R.; SANTOS, J. G. d.-F.; VEDOVOTO, J. M. Simulation of turbulent reactive flows using a fdf methodology – advances in particle density control for normalized variables. *Computers Fluids*, v. 170, p. 128 – 140, 2018. Available at: <https://doi.org/10.1016/j.compfluid.2018.05.004>.

DE-KLERK, A. *Fischer-Tropsch Refining*. John Wiley & Sons, 2012. Available at: <https://doi.org/10.1002/9783527635603>.

DENNER, F.; HEUL, D. R. van-der; OUD, G. T.; VILLAR, M. M.; SILVEIRA-NETO, A. da; WACHEM, B. van. Comparative study of mass-conserving interface capturing frameworks for two-phase flows with surface tension. *International Journal of Multiphase Flow*, v. 61, p. 37 – 47, 2014. ISSN 0301-9322. Available at: <https://doi.org/10.1016/j.ijmultiphaseflow.2013.12.011>.

DOOLEY, S.; WON, S. H.; CHAOS, M.; HEYNE, J.; JU, Y.; DRYER, F. L.; KUMAR, K.; SUNG, C.-J.; WANG, H.; OEHLSCHLAEGER, M. A.; SANTORO, R. J.; LITZINGER, T. A. A jet fuel surrogate formulated by real fuel properties. *Combustion and Flame*, v. 157, n. 12, p. 2333–2339, 2010. Available at: <https://doi.org/10.1016/j.combustflame.2010.07.001>.

DOOLEY, S.; WON, S. H.; HEYNE, J.; FAROUK, T. I.; JU, Y.; DRYER, F. L.; KUMAR, K.; HUI, X.; SUNG, C.-J.; WANG, H.; OEHLSCHLAEGER, M. A.; IYER, V.; IYER, S.; LITZINGER, T. A.; SANTORO, R. J.; MALEWICKI, T.; BREZINSKY, K. The experimental evaluation of a methodology for surrogate fuel formulation to emulate gas phase combustion kinetic phenomena. *Combustion and Flame*, v. 159, n. 4, p. 1444–1466, 2012. Available at: <https://doi.org/10.1016/j.combustflame.2011.11.002>.

ECKEL, G.; GROHMANN, J.; CANTU, L.; SLAVINSKAYA, N.; KATHROTIA, T.; RACHNER, M.; Le Clercq, P.; MEIER, W.; AIGNER, M. LES of a swirl-stabilized kerosene spray flame with a multi-component vaporization model and detailed chemistry. *Combustion and Flame*, v. 207, p. 134–152, 2019. Available at: <https://doi.org/10.1016/j.combustflame.2019.05.011>.

EVRARD, F.; DENNER, F.; WACHEM, B. van. A multi-scale approach to simulate atomisation processes. *International Journal of Multiphase Flow*, v. 119, p. 194–216, 2019. Available at: <https://doi.org/10.1016/j.ijmultiphaseflow.2019.07.005>.

FENG, Z.-G.; MICHAELIDES, E. E. Drag Coefficients of Viscous Spheres at Intermediate and High Reynolds Numbers . *Journal of Fluids Engineering*, v. 123, n. 4, p. 841–849, 05 2001. Available at: <https://doi.org/10.1115/1.1412458>.

FERREIRA, V. M. V. *A hybrid LES/Lagrangian FDF method on adaptive, block-structured mesh*. Master's Thesis (Master's Thesis) — Universidade Federal de Uberlândia, 2015. Available at: <https://doi.org/10.14393/ufu.di.2015.238>.

FERZIGER, J. H.; PERIĆ, M.; STREET, R. L. *Computational Methods for Fluid Dynamics*. [S.l.]: Springer, 2002.

GABRIEL, E.; FAGG, G. E.; BOSILCA, G.; ANGSKUN, T.; DONGARRA, J. J.; SQUYRES, J. M.; SAHAY, V.; KAMBADUR, P.; BARRETT, B.; LUMSDAINE, A. *et al.* Open mpi: Goals, concept, and design of a next generation mpi implementation. In: SPRINGER. *European Parallel Virtual Machine/Message Passing Interface Users' Group Meeting*. [S.l.], 2004. p. 97–104.

GERMANO, M.; PIOMELLI, U.; MOIN, P.; CABOT, W. H. A dynamic subgrid-scale eddy viscosity model. *Physics of Fluids A: Fluid Dynamics*, v. 3, n. 7, p. 1760, 1991. Available at: <https://doi.org/10.1063/1.857955>.

GHASSEMI, H.; BAEK, S. W.; KHAN, Q. S. Experimental study on evaporation of kerosene droplets at elevated pressures and temperatures. *Combustion Science and Technology*, Taylor Francis, v. 178, n. 9, p. 1669–1684, 2006. Available at: <https://doi.org/10.1080/00102200600582392>.

GOODWIN, D. G.; MOFFAT, H. K.; SPETH, R. L. Cantera: An object-oriented software toolkit for chemical kinetics, thermodynamics, and transport processes. 2016. Version 2.2.1. Available at: <https://www.cantera.org>.

GOROKHOVSKI, M. A.; SAVELIEV, V. L. Analyses of Kolmogorov's model of breakup and its application into Lagrangian computation of liquid sprays under air-blast atomization. *Physics of Fluids*, v. 15, n. 1, p. 184–192, 2003. Available at: <https://doi.org/10.1063/1.1527914>.

GOROKHOVSKI, M. A.; SAVELIEV, V. L. Statistical universalities in fragmentation under scaling symmetry with a constant frequency of fragmentation. *Journal of Physics D: Applied Physics*, IOP Publishing, v. 41, n. 8, p. 085405, mar 2008. Available at: <https://doi.org/10.1088/0022-3727/41/8/085405>.

GROPP, W.; LUSK, E.; DOSS, N.; SKJELLUM, A. A high-performance, portable implementation of the mpi message passing interface standard. *Parallel Computing*, v. 22, n. 6, p. 789–828, 1996. Available at: <https://doi.org/10.1016/0167-8191(96)00024-5>.

GUILDENBECHER, D. R.; LÓPEZ-RIVERA, C.; SOJKA, P. E. Secondary atomization. *Experiments in Fluids*, v. 46, n. 371, p. 1432–1114, 2009. Available at: <https://doi.org/10.1007/s00348-008-0593-2>.

HALLETT, W. L. H.; LEGAULT, N. V. Modelling biodiesel droplet evaporation using continuous thermodynamics. *Fuel*, v. 90, n. 3, p. 1221–1228, 2011. Available at: <https://doi.org/10.1016/j.fuel.2010.11.035>.

HANSON, T. D. Uthash. 2013. Version 1.9.6. Available at: <https://github.com/troydhanson/uthash>.

HIROYASU, H.; KADOTA, T. Fuel droplet size distribution in diesel combustion chamber. *SAE Transactions*, JSTOR, p. 2615–2624, 1974.

HUBBARD, G. L.; DENNY, V. E.; MILLS, A. F. Droplet evaporation: Effects of transients and variable properties. *International Journal of Heat and Mass Transfer*, v. 18, n. 9, p. 1003–1008, 1975.

HUBER, M. L.; LEMMON, E. W.; BRUNO, T. J. Surrogate mixture models for the thermophysical properties of aviation fuel Jet-A. *Energy & Fuels*, ACS Publications, v. 24, n. 6, p. 3565–3571, 2010. Available at: <https://doi.org/10.1021/ef700562c>.

IRANNEJAD, A.; JABERI, F. Large eddy simulation of turbulent spray breakup and evaporation. *International Journal of Multiphase Flow*, v. 61, p. 108 – 128, 2014. Available at: <https://doi.org/10.1016/j.ijmultiphaseflow.2014.01.004>.

JAVED, I.; BAEK, S. W.; WAHEED, K.; ALI, G.; CHO, S. O. Evaporation characteristics of kerosene droplets with dilute concentrations of ligand-protected aluminum nanoparticles at elevated temperatures. *Combustion and Flame*, v. 160, n. 12, p. 2955–2963, 2013. Available at: <https://doi.org/10.1016/j.combustflame.2013.07.007>.

JENNY, P.; ROEKAERTS, D.; BEISHUIZEN, N. Modeling of turbulent dilute spray combustion. *Progress in Energy and Combustion Science*, v. 38, n. 6, p. 846 – 887, 2012. Available at: <https://doi.org/10.1016/j.pecs.2012.07.001>.

JEONG, J.; HUSSAIN, F. On the identification of a vortex. *Journal of Fluid Mechanics*, Cambridge Univ Press, v. 285, n. -1, p. 69–94, 1995.

KAMP, J.; VILLWOCK, J.; KRAUME, M. Drop coalescence in technical liquid/liquid applications: A review on experimental techniques and modeling approaches. *Reviews in Chemical Engineering*, De Gruyter, v. 33, n. 1, p. 1–47, 2017. Available at: <https://doi.org/10.1515/revce-2015-0071>.

KHAN, Q.; BAEK, S. W.; LEE, S. Y. Effect of droplet initial diameter on droplet vaporization regimes for kerosene fuel droplet. In: *45th AIAA Aerospace Sciences Meeting and Exhibit*. [S.l.: s.n.], 2007. p. 1181.

KIM, D.; MARTZ, J.; VIOLI, A. A surrogate for emulating the physical and chemical properties of conventional jet fuel. *Combustion and Flame*, v. 161, n. 6, p. 1489–1498, 2014. Available at: <https://doi.org/10.1016/j.combustflame.2013.12.015>.

KIUSALAAS, J. *Numerical Methods in Engineering with Python 3*. 3. ed. Cambridge University Press, 2013. Available at: <https://doi.org/10.1017/CBO9781139523899>.

KOESTERS, A. *Modeling of Diesel Fuel Spray Formation and Combustion in OpenFOAM*. Phd Thesis (PhD Thesis) — Chalmers University of Technology, 2012. Available at: <https://research.chalmers.se/en/publication/154696>.

KOLMOGOROV, A. N. On the log-normal distribution of particles sizes during breakup process. In: *Dokl. Akad. Nauk. SSSR*. [S.l.: s.n.], 1941. p. 99–101.

LAW, C.; SIRIGNANO, W. Unsteady droplet combustion with droplet heating - II: Conduction limit. *Combustion and Flame*, v. 28, p. 175–186, 1977. Available at: <https://doi.org/10.1016/0010-2180(77)90023-2>.

LEBOISSETIER, A.; OKONG'O, N.; BELLAN, J. Consistent large-eddy simulation of a temporal mixing layer laden with evaporating drops. part 2. a posteriori modelling. *Journal of Fluid Mechanics*, Cambridge University Press, v. 523, p. 37–78, 2005. Available at: <https://doi.org/10.1017/S0022112004002101>.

LEFEBVRE, A. H.; MCDONELL, V. G. *Atomization and Sprays*. [S.l.]: CRC press, 2017.

LI, J.; MASON, D. A computational investigation of transient heat transfer in pneumatic transport of granular particles. *Powder Technology*, v. 112, n. 3, p. 273–282, 2000. Available at: <https://doi.org/10.1016/S0032-5910(00)00302-8>.

LI, Y.; RYBDYLOVA, O. Application of the generalised fully lagrangian approach to simulating polydisperse gas-droplet flows. *International Journal of Multiphase Flow*, v. 142, p. 103716, 2021. Available at: <https://doi.org/10.1016/j.ijmultiphaseflow.2021.103716>.

LILLY, D. A proposed modification of the Germano subgrid-scale closure method. *Physics of Fluids A: Fluid Dynamics*, v. 4, p. 633, 1992.

LIMA, R. S. de. *Desenvolvimento e implementação de malhas adaptativas bloco-estruturadas para computação paralela em mecânica dos fluidos*. Phd Thesis (PhD Thesis) — Universidade Federal de Uberlândia, 2012. Available at: <https://repositorio.ufu.br/handle/123456789/14727>.

LISSITSYNA, K.; HUERTAS, S.; QUINTERO, L. C.; POLO, L. M. PIONA analysis of kerosene by comprehensive two-dimensional gas chromatography coupled to time of flight mass spectrometry. *Fuel*, v. 116, p. 716–722, 2014. Available at: <https://doi.org/10.1016/j.fuel.2013.07.077>.

LIU, G.; YAN, B.; CHEN, G. Technical review on jet fuel production. *Renewable and Sustainable Energy Reviews*, v. 25, p. 59–70, 2013. Available at: <https://doi.org/10.1016/j.rser.2013.03.025>.

MELO, R. R. d. S. *Modelagem e simulação de escoamentos turbulentos com efeitos térmicos, utilizando a metodologia da fronteira imersa e malha adaptativa*. Phd Thesis (PhD Thesis) — Universidade Federal de Uberlândia, 2017. Available at: <https://doi.org/10.14393/ufu.te.2017.79>.

MICHAELIDES, E. *Particles, Bubbles & Drops: Their Motion, Heat And Mass Transfer*. World Scientific, 2006. Available at: <https://doi.org/10.1142/9789812774316_0001>.

MICHAELIDES, E.; CROWE, C. T.; SCHWARZKOPF, J. D. *Multiphase Flow Handbook*. [S.l.]: CRC Press, 2016.

NOVAES, V. Brasil estuda introduzir novo tipo de querosene de aviação. *PANROTAS*, 2021. Available at: <https://www.panrotas.com.br/mercado/economia-e-politica/2021/01/brasil-estuda-introduzir-novo-tipo-de-querosene-de-aviacao_179362.html>.

OLCAY, H.; MALINA, R.; UPADHYE, A. A.; HILEMAN, J. I.; HUBER, G. W.; BARRETT, S. R. H. Techno-economic and environmental evaluation of producing chemicals and drop-in aviation biofuels via aqueous phase processing. *Energy Environ. Sci.*, The Royal Society of Chemistry, v. 11, p. 2085–2101, 2018. Available at: <https://doi.org/10.1039/C7EE03557H>.

OLIVEIRA, D. de. A adoção do querosene de aviação Jet A no brasil é um alento para a indústria nacional. *Portal da Infra*, 2021. Available at: <https://www.agenciainfra.com/blog/infradebate-a-adocao-do-querosene-de-aviacao-jet-a-no-brasil-e-um-alento-para-a-industria-nacional/>.

O'ROURKE, P. J.; AMSDEN, A. A. *The TAB method for numerical calculation of spray droplet breakup*. [S.l.], 1987.

PAKSERESHT, P.; APTE, S. V. Volumetric displacement effects in Euler-Lagrange LES of particle-laden jet flows. *International Journal of Multiphase Flow*, v. 113, p. 16–32, 2019. Available at: <https://doi.org/10.1016/j.ijmultiphaseflow.2018.12.013>.

PATEL, N.; MENON, S. Simulation of spray–turbulence–flame interactions in a lean direct injection combustor. *Combustion and Flame*, v. 153, n. 1, p. 228–257, 2008. Available at: <https://doi.org/10.1016/j.combustflame.2007.09.011>.

PILCH, M.; ERDMAN, C. Use of breakup time data and velocity history data to predict the maximum size of stable fragments for acceleration-induced breakup of a liquid drop. *International Journal of Multiphase Flow*, v. 13, n. 6, p. 741–757, 1987. Available at: <https://doi.org/10.1016/0301-9322(87)90063-2>.

PINHEIRO, A. P. *Lagrangian modeling of droplet evaporation*. Master's Thesis (Master's Thesis) — Universidade Federal de Uberlândia, 2018. Available at: <https://doi.org/10.14393/ufu.di.2018.1180>.

PINHEIRO, A. P.; RYBDYLOVA, O.; ZUBRILIN, I. A.; SAZHIN, S. S.; SACOMANO FILHO, F. L.; VEDOVOTTO, J. M. Modelling of aviation kerosene droplet heating and evaporation using complete fuel composition and surrogates. *Fuel*, v. 305, p. 121564, 2021. Available at: <https://doi.org/10.1016/j.fuel.2021.121564>.

PINHEIRO, A. P.; VEDOVOTO, J. M. Evaluation of droplet evaporation models and the incorporation of natural convection effects. *Flow, Turbulence and Combustion*, v. 102, n. 3, p. 537–558, Mar 2019. Available at: <https://doi.org/10.1007/s10494-018-9973-8>.

PINHEIRO, A. P.; VEDOVOTO, J. M.; SILVEIRA-NETO, A. da. Ethanol droplet evaporation: Effects of ambient temperature, pressure and fuel vapor concentration. *International Journal of Heat and Mass Transfer*, v. 143, p. 118472, 2019. Available at: <https://doi.org/10.1016/j.ijheatmasstransfer.2019.118472>.

POULTON, L.; RYBDYLOVA, O.; ZUBRILIN, I. A.; MATVEEV, S. G.; GURAKOV, N. I.; AL-QUBEISSI, M.; AL-ESAWI, N.; KHAN, T.; GUN'KO, V. M.; SAZHIN, S. S. Modelling of multi-component kerosene and surrogate fuel droplet heating and evaporation characteristics: A comparative analysis. *Fuel*, v. 269, p. 117115, 2020. Available at: <https://doi.org/10.1016/j.fuel.2020.117115>.

RANZ, W.; MARSHALL, W. Evaporation from drops: Part I. *Chemical Engineering Progress*, v. 48, n. 3, p. 141–146, 1952.

RAUCH, B. *Systematic accuracy assessment for alternative aviation fuel evaporation models*. Phd Thesis (PhD Thesis) — University of Stuttgart, 2018. Available at: <https://doi.org/10.18419/opus-9922>.

REITZ, R. Modeling atomization processes in high-pressure vaporizing sprays. *Atomisation and Spray Technology*, v. 3, n. 4, p. 309–337, 1987.

RYBDYLOVA, O.; AL-QUBEISSI, M.; BRAUN, M.; CRUA, C.; MANIN, J.; PICKETT, L. M.; DE-SERCEY, G.; SAZHINA, E. M.; SAZHIN, S. S.; HEIKAL, M. A model for droplet heating and its implementation into ANSYS Fluent. *International Communications in Heat and Mass Transfer*, Elsevier, v. 76, p. 265–270, 2016. Available at: <https://doi.org/10.1016/j.icheatmasstransfer.2016.05.032>.

RYBDYLOVA, O.; POULTON, L.; AL-QUBEISSI, M.; ELWARDANY, A. E.; CRUA, C.; KHAN, T.; SAZHIN, S. S. A model for multi-component droplet heating and evaporation and its implementation into ANSYS Fluent. *International Communications in Heat and Mass Transfer*, v. 90, p. 29–33, 2018. Available at: <https://doi.org/10.1016/j.icheatmasstransfer.2017.10.018>.

SACOMANO FILHO, F. L.; HOSSEINZADEH, A.; SADIKI, A.; JANICKA, J. On the interaction between turbulence and ethanol spray combustion using a dynamic wrinkling model coupled with tabulated chemistry. *Combustion and Flame*, v. 215, p. 203–220, 2020. Available at: <https://doi.org/10.1016/j.combustflame.2020.01.038>.

SANJOSÉ, M. *Evaluation de la méthode Euler-Euler pour la simulation aux grandes échelles des chambres à carburant liquide*. Phd Thesis (PhD Thesis) — Institut National Polytechnique de Toulouse, 2009. Available at: <https://tel.archives-ouvertes.fr/tel-00451199/>.

SANTOS, J. G. d.-F. *Modelagem matemática e computacional de escoamentos gás-sólido em malha adaptativa dinâmica*. Master's Thesis (Master's Thesis) — Universidade Federal de Uberlândia, 2019. Available at: <https://doi.org/10.14393/ufu.di.2019.2218>.

SAZHIN, S. S. *Droplets and Sprays*. Springer, 2014. Available at: <https://doi.org/10.1007/978-1-4471-6386-2>.

SAZHIN, S. S.; AL-QUBEISSI, M.; NASIRI, R.; GUN'KO, V. M.; ELWARDANY, A.; LEMOINE, F.; GRISCH, F.; HEIKAL, M. R. A multi-dimensional quasi-discrete model for the analysis of diesel fuel droplet heating and evaporation. *Fuel*, v. 129, p. 238–266, 2014. Available at: <https://doi.org/10.1016/j.fuel.2014.03.028>.

SCHERER, P. O. J. Interpolation. In: _____. *Computational Physics: Simulation of Classical and Quantum Systems*. Heidelberg: Springer International Publishing, 2013. p. 15–35. Available at: <https://doi.org/10.1007/978-3-319-00401-3_2>.

SENONER, J.-M. *Simulations aux grandes échelles de l'écoulement diphasique dans un brûleur aéronautique par une approche Euler-Lagrange*. Phd Thesis (PhD Thesis), 2010. Available at: <https://tel.archives-ouvertes.fr/tel-00282523/>.

SHIROLKAR, J.; COIMBRA, C.; MCQUAY, M. Q. Fundamental aspects of modeling turbulent particle dispersion in dilute flows. *Progress in Energy and Combustion Science*, v. 22, n. 4, p. 363 – 399, 1996. Available at: <https://doi.org/10.1016/S0360-1285(96)00006-8>.

SILVA, C. M.; LIU, H.; MACEDO, E. A. Models for self-diffusion coefficients of dense fluids, including hydrogen-bonding substances. *Chemical Engineering Science*, v. 53, n. 13, p. 2423–2429, 1998. Available at: <https://doi.org/10.1016/S0009-2509(98)00037-2>.

SILVA, R. P. *Desenvolvimento, implementação e validação de uma estrutura de dados para transporte euleriano-lagrangeano e aplicações em escoamentos bifásicos usando refinamento adaptativo de malha*. Phd Thesis (PhD Thesis) — Universidade Federal de Uberlândia, 2016.

SIRIGNANO, W. A. *Fluid Dynamics and Transport of Droplets and Sprays*. 2. ed. Cambridge University Press, 2010. Available at: <https://doi.org/10.1017/CBO9780511806728>.

SNEGIREV, A. Transient temperature gradient in a single-component vaporizing droplet. *International Journal of Heat and Mass Transfer*, v. 65, p. 80–94, 2013. Available at: <https://doi.org/10.1016/j.ijheatmasstransfer.2013.05.064>.

SOMMERFELD, M.; KUSCHEL, M. Modelling droplet collision outcomes for different substances and viscosities. *Experiments in Fluids*, v. 57, n. 12, p. 1–23, 2016. Available at: <https://doi.org/10.1007/s00348-016-2249-y>.

SUNDARARAJ, R. H.; KUMAR, R. D.; RAUT, A. K.; SEKAR, T. C.; PANDEY, V.; KUSHARI, A.; PURI, S. Combustion and emission characteristics from biojet fuel blends in a gas turbine combustor. *Energy*, v. 182, p. 689–705, 2019. Available at: <https://doi.org/10.1016/j.energy.2019.06.060>.

VEDOVOTO, J. M. *Mathematical and numerical modeling of turbulent reactive flows using a hybrid LES/PDF methodology*. Phd Thesis (PhD Thesis) — Universidade Federal de Uberlândia, 2011. Available at: <https://repositorio.ufu.br/handle/123456789/14704>.

VILLAR, M. M. *Análise numérica detalhada de escoamentos multifásicos bidimensionais*. Phd Thesis (PhD Thesis) — Universidade Federal de Uberlândia, 2007. Available at: <https://repositorio.ufu.br/handle/123456789/14664>.

VOZKA, P.; VRTIŠKA, D.; ŠIMÁČEK, P.; KILAZ, G. Impact of alternative fuel blending components on fuel composition and properties in blends with Jet A. *Energy & Fuels*, ACS Publications, v. 33, n. 4, p. 3275–3289, 2019. Available at: <https://doi.org/10.1021/acs.energyfuels.9b00105>.

WANG, F.; LIU, R.; LI, M.; YAO, J.; JIN, J. Kerosene evaporation rate in high temperature air stationary and convective environment. *Fuel*, v. 211, p. 582–590, 2018. Available at: <https://doi.org/10.1016/j.fuel.2017.08.062>.

WEN, J.; HU, Y.; NAKANISHI, A.; KUROSE, R. Atomization and evaporation process of liquid fuel jets in crossflows: A numerical study using Eulerian/Lagrangian method. *International Journal of Multiphase Flow*, v. 129, p. 103331, 2020. Available at: <https://doi.org/10.1016/j.ijmultiphaseflow.2020.103331>.

WON, S. H.; HAAS, F. M.; DOOLEY, S.; EDWARDS, T.; DRYER, F. L. Reconstruction of chemical structure of real fuel by surrogate formulation based upon combustion property targets. *Combustion and Flame*, v. 183, p. 39–49, 2017. Available at: <https://doi.org/10.1016/j.combustflame.2017.04.032>.

WOODROW, J. E. The laboratory characterization of jet fuel vapor and liquid. *Energy & Fuels*, ACS Publications, v. 17, n. 1, p. 216–224, 2003. Available at: <https://doi.org/10.1021/ef020140p>.

YAWS, C. *Yaws' Handbook of Thermodynamic and Physical Properties of Chemical Compounds*. [S.l.]: Knovel, 2003.

YAWS, C. *Thermophysical Properties of Chemicals and Hydrocarbons*. [S.l.]: William Andrew, 2008.

YAWS, C. *Transport Properties of Chemicals and Hydrocarbons: Viscosity, Thermal Conductivity, and Diffusivity of C1 to C100 Organics and Ac to Zr Inorganic*. [S.l.]: William Andrew, 2009.

YOON, J.; BAEK, S. W. Droplet evaporation behavior of kerosene/nano-aluminum fuels at high pressure environment. *International Journal of Material and Mechanical Engineering*, v. 4, p. 44–49, 2015. Available at: <https://doi.org/10.14355/ijmme.2015.04.007>.

YU, J.; JU, Y.; GOU, X. Surrogate fuel formulation for oxygenated and hydrocarbon fuels by using the molecular structures and functional groups. *Fuel*, v. 166, p. 211–218, 2016. Available at: <https://doi.org/10.1016/j.fuel.2015.10.085>.

YUEN, M. C.; CHEN, L. W. On drag of evaporating liquid droplets. *Combustion Science and Technology*, Taylor Francis, v. 14, n. 4-6, p. 147–154, 1976.

ZANG, D.; TARAFDAR, S.; TARASEVICH, Y. Y.; CHOUDHURY, M. D.; DUTTA, T. Evaporation of a droplet: From physics to applications. *Physics Reports*, v. 804, p. 1 – 56, 2019. Available at: <https://doi.org/10.1016/j.physrep.2019.01.008>.

APPENDIX A

A Thermodynamic and transport properties database

The transport and thermodynamic properties of the individual Jet A components used, based on the tabulated data collected from Yaws (2003), Yaws (2008), Yaws (2009), are presented in the following section. In Section 2, the transport and thermodynamic properties of the components used in Jet A surrogates are presented. The transport and thermodynamic properties are presented in SI units, unless the unit is specified.

A.1 Jet A properties

The properties here presented are valid for the following components, with n representing the number of carbon atoms of each component:

- n-paraffins (C_nH_{2n+2}) for $7 \leqslant n \leqslant 18$;
- iso-paraffins (C_nH_{2n+2}) for $7 \leqslant n \leqslant 18$;
- monocycloparaffins (C_nH_{2n}) for $7 \leqslant n \leqslant 17$;
- dicycloparaffins (C_nH_{2n-2}) for $8 \leqslant n \leqslant 15$;
- alkylbenzenes (C_nH_{2n-6}) for $6 \leqslant n \leqslant 17$;
- cycloaromatics (C_nH_{2n-8}) for $9 \leqslant n \leqslant 15$;
- alkylnaphthalenes (C_nH_{2n-12}) for $10 \leqslant n \leqslant 15$.

A.1.1 Critical temperature and pressure

Following Sazhin *et al.* (2014) and using data provided in Yaws (2008), the dependencies of critical temperature and pressure on carbon number are approximated by the following equations:

$$T_{\mathrm{cr}}(n) = A_{\mathrm{cr}} + B_{\mathrm{cr}}n + C_{\mathrm{cr}}n^2 + D_{\mathrm{cr}}n^3, \tag{1}$$

$$p_{\mathrm{cr}}(n) = A_{\mathrm{cr}} + B_{\mathrm{cr}}n + C_{\mathrm{cr}}n^2 + D_{\mathrm{cr}}n^3, \tag{2}$$

where p_{cr} is given in bar and the coefficients A_{cr}, B_{cr}, C_{cr} and D_{cr} for each hydrocarbon group to calculate both critical temperature and pressure are:

Table A.1: Coefficients to calculate critical temperature based on Eq. (1).

Coef	n-par	iso-par	monocyclo	dicyclo
A_{cr}	263.57832168	292.10720280	29.09477525	-320.64867965
B_{cr}	51.40631961	41.58990417	128.15485043	190.61380231
C_{cr}	-1.89891220	-1.18311577	-7.75925408	-11.29790043
D_{cr}	0.02973323	0.01732971	0.17323815	0.22717172

Coef	alkyb	cycloa	alkylnaph
A_{cr}	451.04119991	-111.160952	445.642857
B_{cr}	9.75417786	167.850397	36.9344312
C_{cr}	1.92963148	-11.4427381	-0.711031746
D_{cr}	-0.07296685	0.29305556	0.00453704

Table A.2: Coefficients to calculate critical pressure based on Eq. (2).

Coef	n-par	iso-par	monocyclo	dicyclo
A_{cr}	50.97492507	44.16799201	56.96146853	41.43409091
B_{cr}	-4.44716302	-3.09357402	-2.18197747	0.71171717
C_{cr}	0.16675547	0.10287324	-0.11116550	-0.36636364
D_{cr}	-0.00206553	-0.00150479	0.00626651	0.01479798

A.1.2 Liquid density

The following approximations are based on droplet average temperatures. They are assumed to be valid until the vicinity of the liquid component critical temperatures are reached. Following Sazhin *et al.* (2014) and using data provided in Yaws (2008), the dependency of liquid density on carbon number and droplet average temperature is approximated by the following equation:

$$\rho_l(T) = 1000 A_\rho B_\rho^{-\left(1-\frac{T}{T_{\mathrm{cr}}}\right)^{C_\rho}}, \tag{3}$$

Coef	alkyb	cycloa	alkylnaph
A_{cr}	117.09889777	38.57904762	71.12714286
B_{cr}	-16.50622156	5.78865079	4.39328042
C_{cr}	0.96297869	-0.88821429	-1.20222222
D_{cr}	-0.02007382	0.02861111	0.04592593

where A_ρ, B_ρ and C_ρ are approximated using the following expressions:

for n-paraffins,

$$\begin{cases} A_\rho = -3.651 \times 10^{-5} n^3 + 1.23322 \times 10^{-3} n^2 - 0.01233966 n + 0.27108194, \\ B_\rho = -1.308 \times 10^{-5} n^3 + 5.2495 \times 10^{-4} n^2 - 7.41829 \times 10^{-3} n + 0.29111626, \\ C_\rho = -3.3428 \times 10^{-4} n^3 + 0.01169429 n^2 - 0.12576357 n + 0.70298720, \\ C_\rho = 0.27348, \quad \text{if} \quad n = 14. \end{cases} \tag{4}$$

for iso-paraffins,

$$\begin{cases} A_\rho = -4.56 \times 10^{-6} n^3 + 5.956 \times 10^{-5} n^2 + 1.52591 \times 10^{-3} n + 0.22380305, \\ A_\rho = 0.23379, \quad \text{if} \quad n = 18, \\ B_\rho = -1.389 \times 10^{-5} n^3 + 5.9426 \times 10^{-4} n^2 - 8.56097 \times 10^{-3} n + 0.30516675, \\ B_\rho = 5.075 \times 10^{-5} n^3 - 1.80925 \times 10^{-3} n^2 + 0.01873450 n + 0.2019320, \\ \text{if} \quad n = 8, 9, 12, 18, \\ C_\rho = -3.56167 \times 10^{-3} n^3 + 0.096530 n^2 - 0.85372833 n + 2.746780, \quad \text{if} \quad n \leqslant 10, \\ C_\rho = 0.28571, \quad \text{if} \quad n \geqslant 11. \end{cases} \tag{5}$$

for monocycloparaffins,

$$\begin{cases} A_\rho = -1.708 \times 10^{-5} n^3 + 4.7114 \times 10^{-4} n^2 - 2.21842 \times 10^{-3} n + 0.27093140, \\ B_\rho = -1.4619 \times 10^{-4} n^3 + 4.98771 \times 10^{-3} n^2 - 0.0524475 n + 0.44174696, \\ B_\rho = 1.9250 \times 10^{-4} n^2 - 4.19250 \times 10^{-3} n + 0.333120, \quad \text{if} \quad n = 14, 16, 17, \\ C_\rho = 0.28571. \end{cases} \tag{6}$$

for dicycloparaffins,

$$\begin{cases} A_\rho = -3.705 \times 10^{-5} n^3 + 4.8848 \times 10^{-4} n^2 + 5.33995 \times 10^{-3} n + 0.21543407, \\ B_\rho = -1.0292 \times 10^{-4} n^3 + 3.62171 \times 10^{-3} n^2 - 0.04138827 n + 0.4190520, \\ B_\rho = 0.27581, \quad \text{if} \quad n = 13, \\ C_\rho = 0.28571. \end{cases} \tag{7}$$

for alkylbenzenes,

$$\begin{cases} A_\rho = -9.714 \times 10^{-5} n^3 + 3.62102 \times 10^{-3} n^2 - 0.04655698 n + 0.47235423, \\ B_\rho = -6.912 \times 10^{-10} n^3 + 2.41783 \times 10^{-3} n^2 - 0.02853582 n + 0.36699367, \\ C_\rho = 1.8244 \times 10^{-4} n^3 - 5.84519 \times 10^{-3} n^2 + 0.05870678 n + 0.10448834, \\ C_\rho = -0.0151250 n^2 + 0.4137250 n - 2.501350, \quad \text{if} \quad n = 13, 14, 15. \end{cases} \tag{8}$$

for cycloaromatics,

$$\begin{cases} A_\rho = -1.250 \times 10^{-4} n^3 + 4.95940 \times 10^{-3} n^2 - 0.068848607 n + 0.61540095, \\ B_\rho = 6.11 \times 10^{-6} n^3 + 1.5298 \times 10^{-4} n^2 - 7.25956 \times 10^{-3} n + 0.30978857, \\ C_\rho = 0.28571, \\ C_\rho = -0.034530 n + 0.6130, \quad \text{if} \quad n = 9, 10. \end{cases} \tag{9}$$

for alkylnaphthalenes,

$$\begin{cases} A_\rho = -3.62 \times 10^{-6} n^3 + 3.4528 \times 10^{-4} n^2 - 0.01143223 n + 0.39374717, \\ A_\rho = 0.2719, \quad \text{if} \quad n = 11, \\ B_\rho = -4.2796 \times 10^{-4} n^3 + 0.01404540 n^2 - 0.14220378 n + 0.66715857, \\ C_\rho = -2.620 \times 10^{-3} n^3 + 0.097870 n^2 - 1.203960 n + 5.14560, \\ C_\rho = 0.28571, \quad \text{if} \quad n = 13, 15. \end{cases} \tag{10}$$

A.1.3 Liquid dynamic viscosity

The following approximations are based on droplet average temperatures. They are assumed to be valid until the vicinity of the liquid component critical temperatures are reached.

Following Sazhin *et al.* (2014) and using data provided in Yaws (2009), the dependency of liquid dynamic viscosity on carbon number and droplet average temperature is approximated by the following equation:

$$\mu_l(T) = 0.001 \times 10^{A_v + \frac{B_v}{T} + C_v T + D_v T^2}, \tag{11}$$

where the coefficients A_v, B_v, C_v and D_v for each hydrocarbon group are:

for n-paraffins,

$$\begin{cases} A_\mu = 1.6635 \times 10^{-3} n^3 - 0.052863 n^2 + 0.21103 n - 4.8442, \\ B_\mu = -0.24372 n^3 + 6.1103 n^2 + 49.962 n + 191.42, \\ C_\mu = -6.8753 \times 10^{-6} n^3 + 2.5868 \times 10^{-4} n^2 - 2.7814 \times 10^{-3} n + 0.021678, \\ D_\mu = 1.2888 \times 10^{-8} n^3 - 5.0968 \times 10^{-7} n^2 + 6.5990 \times 10^{-6} n - 4.0175 \times 10^{-5}. \end{cases} \tag{12}$$

for iso-paraffins,

$$\begin{cases} A_\mu = 0.012873 n^3 - 0.49949 n^2 + 6.2260 n - 30.166, \\ B_\mu = -1.3323 n^3 + 51.923 n^2 - 618.43 n + 3.1441 E3, \\ C_\mu = -3.5487 \times 10^{-5} n^3 + 1.3934 \times 10^{-3} n^2 - 0.017960 n + 0.085316, \\ D_\mu = 3.4619 \times 10^{-8} n^3 - 1.3814 \times 10^{-6} n^2 + 1.8379 \times 10^{-5} n - 8.9821 \times 10^{-5}. \end{cases} \tag{13}$$

for monocycloparaffins,

$$\begin{cases} A_\mu = 8.6111 \times 10^{-3} n^3 - 0.33451 n^2 + 3.9745 n - 20.158, \\ B_\mu = -1.1679 n^3 + 44.088 n^2 - 474.62 n + 2.5092 E3, \\ C_\mu = -2.3440 \times 10^{-5} n^3 + 9.2128 \times 10^{-4} n^2 - 0.011445 n + 0.054663, \\ D_\mu = 2.2707 \times 10^{-8} n^3 - 9.0395 \times 10^{-7} n^2 + 1.1655 \times 10^{-5} n - 5.6371 \times 10^{-5}. \end{cases} \tag{14}$$

for dicycloparaffins,

$$\begin{cases} A_\mu = 0.072794n^3 - 1.9886n^2 + 16.419n - 42.703, \\ B_\mu = -15.668n^3 + 463.60n^2 - 4.3255E3n + 1.3464E4, \\ C_\mu = -8.6777 \times 10^{-5}n^3 + 1.8914 \times 10^{-3}n^2 - 8.5977 \times 10^{-3}n - 8.4313 \times 10^{-3}, \\ D_\mu = -1.1165 \times 10^{-7}n^3 + 3.9247 \times 10^{-6}n^2 - 4.5025 \times 10^{-5}n + 1.6352 \times 10^{-4}. \end{cases} \quad (15)$$

for alkylbenzenes,

$$\begin{cases} A_\mu = -0.041760n^3 + 1.3069n^2 - 13.448n + 38.038, \\ B_\mu = 2.2210n^3 - 66.855n^2 + 744.21n - 1.7787E3, \\ C_\mu = 1.0143 \times 10^{-4}n^3 - 3.1853 \times 10^{-3}n^2 + 0.032736n - 0.096135, \\ D_\mu = -9.7759 \times 10^{-8}n^3 + 3.0771 \times 10^{-6}n^2 - 3.1220 \times 10^{-5}n + 8.9907 \times 10^{-5}. \end{cases} \quad (16)$$

for cycloaromatics,

$$\begin{cases} A_\mu = 5.5000 \times 10^{-3}n^3 - 0.44859n^2 + 8.6641n - 53.134, \\ B_\mu = 4.2774n^3 - 105.25n^2 + 623.23n + 1.1654E3, \\ C_\mu = -1.5417 \times 10^{-5}n^3 + 1.0300 \times 10^{-3}n^2 - 0.018711n + 0.10910, \\ D_\mu = -3.8333 \times 10^{-8}n^3 + 1.0913 \times 10^{-6}n^2 - 8.9503 \times 10^{-6}n + 1.1289 \times 10^{-5}. \end{cases} \quad (17)$$

for alkylnaphthalenes,

$$\begin{cases} A_\mu = 2.7433n^3 - 95.336n^2 + 1.1001E3n - 4.2213E3, \\ B_\mu = -474.32n^3 + 1.6475E4n^2 - 1.8997E5n + 7.2836E5, \\ C_\mu = -5.9552 \times 10^{-3}n^3 + 0.20671n^2 - 2.3827n + 9.1302, \\ D_\mu = 4.1097 \times 10^{-6}n^3 - 1.4245 \times 10^{-4}n^2 + 1.6398 \times 10^{-3}n - 6.2761 \times 10^{-3}. \end{cases} \quad (18)$$

A.1.4 Liquid thermal conductivity

The following approximations are based on droplet average temperatures. They are assumed to be valid until the vicinity of the liquid component critical temperatures are reached. Following Sazhin *et al.* (2014) and using data provided in Yaws (2009), the dependency of liquid

thermal conductivity on carbon number and droplet average temperature is approximated by the following equation:

$$k_l(T) = \left(A_k + B_k T + C_k T^2\right). \tag{19}$$

where the coefficients A_k, B_k and C_k for each hydrocarbon group are:

for n-paraffins,

$$\begin{cases} A_k = -1.28427 \times 10^{-5} n^3 - 5.98159 \times 10^{-6} n^2 + 5.96748 \times 10^{-3} n + 1.80190 \times 10^{-1}, \\ A_k = -3.51286 \times 10^{-5} n^3 + 1.65484 \times 10^{-3} n^2 - 2.44423 \times 10^{-2} n + 3.11264 \times 10^{-1}, \\ \quad \text{if} \quad n = 9, 13, 14, 15, 16, \\ B_k = 2.81312 \times 10^{-8} n^3 + 1.9869 \times 10^{-6} n^2 - 5.84508 \times 10^{-5} n + 7.34781 \times 10^{-6}, \\ B_k = -2.0 \times 10^{-4}, \quad \text{if} \quad n = 9, 13, 14, 15, 16, \\ C_k = -7.45277 \times 10^{-10} n^3 + 1.97325 \times 10^{-8} n^2 - 1.10986 \times 10^{-7} n - 1.18479 \times 10^{-8}, \\ C_k = 0, \quad \text{if} \quad n = 13, 14, 15, 16. \end{cases} \tag{20}$$

for iso-paraffins,

$$\begin{cases} A_k = 5.89225589 \times 10^{-6} n^3 - 1.42463092 \times 10^{-4} n^2 + 2.41178451 \times 10^{-3} n + \\ +1.75310490 \times 10^{-1}, \\ B_k = -2.5 \times 10^{-4}, \\ B_k = -2.57 \times 10^{-4}, \quad \text{if} \quad n = 8, \\ C_k = 0. \end{cases} \tag{21}$$

for monocycloparaffins,

$$\begin{cases} A_k = 5.83916084 \times 10^{-5} n^3 - 2.00268065 \times 10^{-3} n^2 + 1.65643357 \times 10^{-2} n + \\ +1.44828205 \times 10^{-1}, \\ B_k = -7.81721057 \times 10^{-8} n^3 + 2.44378788 \times 10^{-6} n^2 - 1.52993687 \times 10^{-5} n - \\ -1.84743007 \times 10^{-4}, \\ C_k = 0. \end{cases} \tag{22}$$

for dicycloparaffins,

$$\begin{cases} A_k = -1.38333333 \times 10^{-3} n^3 + 4.29440476 \times 10^{-2} n^2 - 4.426750 \times 10^{-1} n + 1.70659286, \\ A_k = 2.17 \times 10^{-1}, \quad \text{if} \quad n = 15, \\ B_k = -2.5 \times 10^{-4}, \\ B_k = -6.18 \times 10^{-6} n^2 + 1.63919 \times 10^{-4} n - 1.16888 \times 10^{-3}, \quad \text{if} \quad n = 10, 13, 14, \\ C_k = 0. \end{cases} \tag{23}$$

for alkylbenzenes,

$$\begin{cases} A_k = 5.82390601 \times 10^{-5} n^3 - 1.76280647 \times 10^{-3} n^2 + 1.81168242 \times 10^{-2} n + \\ +1.26657757 \times 10^{-1}, \\ A_k = 2.1 \times 10^{-1}, \quad \text{if} \quad n = 7, \\ B_k = 4.53152174 \times 10^{-7} n^3 - 2.96894410 \times 10^{-7} n^2 - 1.21991693 \times 10^{-4} n + \\ +5.64151957 \times 10^{-4}, \\ B_k = -2.86 \times 10^{-4}, \quad \text{if} \quad n = 7, \\ B_k = -2.0 \times 10^{-4}, \quad \text{if} \quad 13 \leqslant n \leqslant 17, \\ C_k = 3.44898148 \times 10^{-9} n^3 - 1.01939849 \times 10^{-7} n^2 + 1.00913420 \times 10^{-6} n - \\ -3.30045979 \times 10^{-6}, \\ C_k = 0, \quad \text{if} \quad 12 \leqslant n \leqslant 17. \end{cases} \tag{24}$$

for cycloaromatics,

$$\begin{cases} A_k = 3.04347826 \times 10^{-4} n^3 - 1.18446170 \times 10^{-2} n^2 + 1.54743789 \times 10^{-1} n - \\ -4.65067495 \times 10^{-1}, \\ A_k = 1.50 \times 10^{-1}, \quad \text{if} \quad n = 10, \\ B_k = -2.5 \times 10^{-4}, \\ B_k = 1.2104 \times 10^{-4} n - 1.277097 \times 10^{-3}, \quad \text{if} \quad n = 9, 10, \\ C_k = 0. \end{cases} \tag{25}$$

for alkylnaphthalenes,

$$\begin{cases} A_k = 5.86792453 \times 10^{-4} n^3 - 2.36010782 \times 10^{-2} n^2 + 3.17659299 \times 10^{-1} n - 1.21404636, \\ A_k = 1.63 \times 10^{-1}, \quad \text{if} \quad n = 11, \\ B_k = -2.5 \times 10^{-4}, \\ B_k = 2.889 \times 10^{-5} n - 4.289 \times 10^{-4}, \quad \text{if} \quad n = 10, 11, \\ C_k = 0. \end{cases} \tag{26}$$

A.1.5 Liquid specific heat capacity

The following approximations are based on droplet average temperatures. They are assumed to be valid until the vicinity of the liquid component critical temperatures are reached. Following Sazhin *et al.* (2014) and using data provided in Yaws (2003), the dependency of liquid specific heat capacity on carbon number and droplet average temperature is approximated by the following equation:

$$c_l(T) = \frac{1000}{M(n)} \left(A_c + B_c T + C_c T^2 + D_c T^3 \right), \tag{27}$$

where $M(n)$ is the component molar mass and the coefficients A_c, B_c, C_c and D_c for each hydrocarbon group are:

for n-paraffins,

$$\begin{cases} A_c = 0.13603069 n^3 - 4.07475758 n^2 + 38.32630264 n - 22.56629371, \\ B_c = -3.5284 \times 10^{-4} n^3 + 8.21387 \times 10^{-3} n^2 + 0.13820726 n - 0.22870, \\ C_c = 9.91712 \times 10^{-8} n^3 + 1.02012 \times 10^{-5} n^2 - 5.90184 \times 10^{-4} n + 4.16866 \times 10^{-4}, \\ D_c = -4.87995 \times 10^{-10} n^3 + 9.55370 \times 10^{-9} n^2 + 1.3320 \times 10^{-7} n + 3.04028 \times 10^{-6}. \end{cases} \tag{28}$$

for iso-paraffins,

$$\begin{cases} A_c = -2.347009 \times 10^{-2} n^3 + 0.31530003 n^2 + 18.49326762 n - 21.46292907, \\ B_c = 6.5180 \times 10^{-4} n^3 - 2.267697 \times 10^{-2} n^2 + 0.34579880 n - 0.85354515, \\ C_c = -1.34132 \times 10^{-6} n^3 + 4.32455 \times 10^{-5} n^2 - 6.07901 \times 10^{-4} n + 3.56658 \times 10^{-4}, \\ D_c = 8.85496 \times 10^{-10} n^3 - 2.40940 \times 10^{-8} n^2 + 2.60783 \times 10^{-7} n + 2.45139 \times 10^{-6}. \end{cases} \tag{29}$$

for monocycloparaffins,

$$\begin{cases} A_c = 0.10425117 n^3 - 4.04246037 n^2 + 63.74764744 n - 173.940669, \\ B_c = -2.13813 \times 10^{-3} n^3 + 8.881317 \times 10^{-2} n^2 - 1.05086735 n + 4.23265268, \\ C_c = 5.13963 \times 10^{-6} n^3 - 2.09951 \times 10^{-4} n^2 + 2.51306 \times 10^{-3} n - 0.0103186, \\ D_c = -4.9857 \times 10^{-9} n^3 + 2.01118 \times 10^{-7} n^2 - 2.44869 \times 10^{-6} n + 1.06439 \times 10^{-5}. \end{cases} \tag{30}$$

for dicycloparaffins,

$$\begin{cases} A_c = -1.78825505 n^3 + 62.94041234 n^2 - 698.63173088 n + 2628.71217965, \\ B_c = 0.01080833 n^3 - 0.37819048 n^2 + 4.330275 n - 15.62234286, \\ C_c = -2.78888 \times 10^{-5} n^3 + 9.72118 \times 10^{-4} n^2 - 1.10501 \times 10^{-2} n + 3.95482 \times 10^{-2}, \\ D_c = 2.57278 \times 10^{-8} n^3 - 8.87394 \times 10^{-7} n^2 + 9.94176 \times 10^{-6} n - 3.44554 \times 10^{-5}. \end{cases} \tag{31}$$

for alkylbenzenes,

$$\begin{cases} A_c = 0.73529552 n^3 - 26.59176035 n^2 + 325.16134562 n - 1170.11013398, \\ B_c = -2.65776 \times 10^{-3} n^3 + 0.11104252 n^2 - 1.40254946 n + 6.10534237, \\ C_c = 6.72440 \times 10^{-6} n^3 - 2.82790 \times 10^{-4} n^2 + 3.64120 \times 10^{-3} n - 1.62253 \times 10^{-2}, \\ D_c = -6.09978 \times 10^{-9} n^3 + 2.54403 \times 10^{-7} n^2 - 3.26094 \times 10^{-6} n + 1.51168 \times 10^{-5}. \end{cases} \tag{32}$$

for cycloaromatics,

$$\begin{cases} A_c = 1.318n^3 - 50.82504762n^2 + 663.61557143n - 2726.1422381, \\ B_c = -0.01116667n^3 + 0.42945595n^2 - 5.36197262n + 22.2708333, \\ C_c = 3.01617 \times 10^{-5}n^3 - 1.15686 \times 10^{-3}n^2 + 1.44459 \times 10^{-2}n - 5.99228 \times 10^{-2}, \\ D_c = -2.85694 \times 10^{-8}n^3 + 1.08908 \times 10^{-6}n^2 - 1.35182 \times 10^{-5}n + 5.60791 \times 10^{-5}. \end{cases} \tag{33}$$

for alkylnaphthalenes,

$$\begin{cases} A_c = 4.41637963n^3 - 181.03675397n^2 + 2483.50515212n - 11177.81671428, \\ B_c = -0.03188704n^3 + 1.30490675n^2 - 17.64329907n + 79.36332857, \\ C_c = 5.94756 \times 10^{-5}n^3 - 2.46284 \times 10^{-3}n^2 + 3.36634 \times 10^{-2}n - 1.53081 \times 10^{-1}, \\ D_c = -3.88611 \times 10^{-8}n^3 + 1.62467 \times 10^{-6}n^2 - 2.23411 \times 10^{-5}n + 1.02473 \times 10^{-4}. \end{cases} \tag{34}$$

A.1.6 Latent heat of evaporation

Following Sazhin *et al.* (2014) and using data provided in Yaws (2008), the dependency of latent heat of evaporation on carbon number and droplet surface temperature is approximated by the following equation:

$$L = \frac{A_L(1 - T_r)^{B_L}}{M(n)} \times 10^6, \tag{35}$$

where $M(n)$ is the component molar mass, $T_r = T/T_{\mathrm{cr}}$ and the coefficients A_L and B_L for each hydrocarbon group are:

for n-paraffins,

$$\begin{cases} A_L = 0.02371026n^3 - 0.93664206n^2 + 16.77309084n - 29.36052817, \\ B_L = 4.891 \times 10^{-5}n^3 - 1.69720 \times 10^{-3}n^2 + 0.02395828n + 0.27914689, \\ B_L = 6.0 \times 10^{-3}n + 0.391, \quad \text{if} \quad n = 8, 10. \end{cases} \tag{36}$$

for iso-paraffins,

$$\begin{cases} A_L = 0.01401159n^3 - 0.53344205n^2 + 10.29494376n + 0.95414985, \\ B_L = 0.38, \\ B_L = 0.044833333n^3 - 1.1545n^2 + 9.81366667n - 27.095, \quad \text{if} \quad 7 \leqslant n \leqslant 10. \end{cases} \tag{37}$$

for monocycloparaffins,

$$\begin{cases} A_L = -3.60049 \times 10^{-3}n^3 + 0.04521772n^2 + 4.01286599n + 20.92204848, \\ B_L = 0.38, \\ B_L = 0.382, \quad \text{if} \quad n = 7. \end{cases} \tag{38}$$

for dicycloparaffins,

$$\begin{cases} A_L = -0.21151616n^3 + 7.44189329n^2 - 80.90626739n + 333.14012965, \\ B_L = 0.38. \end{cases} \tag{39}$$

for alkylbenzenes,

$$\begin{cases} A_L = -0.01015154n^3 + 0.56325414n^2 - 3.65181645n + 52.98586128, \\ B_L = -4.8006 \times 10^{-4}n^3 + 0.01880347n^2 - 0.2322112n + 1.2884813. \end{cases} \tag{40}$$

for cycloaromatics,

$$\begin{cases} A_L = -0.16622778n^3 + 6.12692857n^2 - 70.25798413n + 318.35692381, \\ B_L = 0.38, \\ B_L = -0.112n + 1.428, \quad \text{if} \quad n = 9, 10. \end{cases} \tag{41}$$

for alkylnaphthalenes,

$$\begin{cases} A_L = -0.04475185n^3 + 1.9486623n^2 - 23.16606442n + 152.2001, \\ B_L = -8.66667 \times 10^{-3}n^3 + 0.3145n^2 - 3.78483333n + 15.53, \\ B_L = 0.38, \quad \text{if} \quad n = 13, 15. \end{cases} \tag{42}$$

A.1.7 Saturated vapor pressure

Following Sazhin *et al.* (2014) and using data provided in Yaws (2003), the dependencies of saturated vapor pressure on carbon number and droplet surface temperature are approximated by the following equations:

$$p_{\text{sat}} = 10^{A_p - \frac{B_p}{T + C_p}} \times 133.322387415, \tag{43}$$

where T is in °C and the coefficients A_p, B_p and C_p for each hydrocarbon group are:

for n-paraffins,

$$\begin{cases} A_p = 1.729 \times 10^{-4}n^3 - 8.90265 \times 10^{-3}n^2 + 0.15972231n + 6.32493506, \\ B_p = 0.42901709n^3 - 19.62526141n^2 + 348.74864857n - 271.18350649, \\ C_p = 0.07338086n^3 - 2.8025752n^2 + 28.16525173n + 140.3191029. \end{cases} \tag{44}$$

for iso-paraffins,

$$\begin{cases} A_p = -4.6396 \times 10^{-4} n^3 + 0.01791282 n^2 - 0.21598098 n + 7.85098323, \\ A_p = -9.17 \times 10^{-3} n^2 + 0.16612 n + 6.38501, \quad \text{if} \quad 8 \leqslant n \leqslant 10, \\ B_p = 0.40284641 n^3 - 16.09970252 n^2 + 251.44656196 n + 262.57155844, \\ C_p = 0.05250932 n^3 - 1.63418332 n^2 + 6.50947219 n + 251.7032977. \end{cases} \tag{45}$$

for monocycloparaffins,

$$\begin{cases} A_p = -2.0264 \times 10^{-4} n^3 + 0.01027486 n^2 - 0.17190187 n + 7.79361147, \\ B_p = 0.12405983 n^3 - 5.66221445 n^2 + 131.48430847 n + 746.06058275, \\ C_p = -0.05383683 n^3 + 2.32390793 n^2 - 35.83641142 n + 381.36450816. \end{cases} \tag{46}$$

for dicycloparaffins,

$$\begin{cases} A_p = 2.90646 \times 10^{-3} n^3 - 0.09640732 n^2 + 1.04406791 n + 3.28678719, \\ B_p = 2.00133838 n^3 - 72.24837662 n^2 + 921.33511183 n - 2355.50867965, \\ C_p = 0.2047096 n^3 - 7.0249632 n^2 + 74.00056962 n - 34.47946753. \end{cases} \tag{47}$$

for alkylbenzenes,

$$\begin{cases} A_p = 1.1956 \times 10^{-4} n^3 - 3.44724 \times 10^{-3} n^2 + 0.06802439 n + 6.76796999, \\ B_p = 0.08982906 n^3 - 6.15867299 n^2 + 193.77953324 n + 351.23931402, \\ C_p = 6.2217 \times 10^{-3} n^3 - 0.50178965 n^2 + 4.6466855 n + 219.98779276. \end{cases} \tag{48}$$

for cycloaromatics,

$$\begin{cases} A_p = -1.4837 \times 10^{-4} n^3 + 0.01522933 n^2 - 0.29303564 n + 8.70964201, \\ A_p = 7.07391, \quad \text{if} \quad n = 11, \\ B_p = 0.07888889 n^3 + 4.55285714 n^2 - 88.2229365 n + 2110.11381, \\ C_p = -0.0121 n^3 + 5.45827381 n^2 - 84.0731071 n + 625.767333. \end{cases} \tag{49}$$

for alkylnaphthalenes,

$$\begin{cases} A_p = 8.64034 \times 10^{-3} n^3 - 0.32482139 n^2 + 4.07331789 n - 9.71979122, \\ A_p = 7.10905, \quad \text{if} \quad n = 12, \\ B_p = 6.17222222 n^3 - 222.169762 n^2 + 2715.4823 n - 9235.68, \\ C_p = 0.57264815 n^3 - 20.4402698 n^2 + 236.464082 n - 677.375714. \end{cases} \tag{50}$$

A.2 Surrogates properties

The surrogates properties are calculated using the same expressions presented previously for Jet A and they come from the same database. However, as the coefficients used in the expressions are different, they are showed in the next sections for each property and each surrogate component.

A.2.1 Critical temperature

Comp	T_{cr}	p_{cr}
1	568.70	24.90
2	617.70	21.10
3	658.00	18.20
4	693.00	15.70
5	723.00	14.00
6	530.40	27.40
7	559.64	24.84
8	650.75	19.79
9	725.72	14.77
10	572.19	34.80
11	708.63	19.56
12	687.05	32.00
13	740.84	26.38
14	701.48	26.38
15	697.11	26.38
16	591.79	41.08
17	630.37	37.32
18	638.35	32.00
19	637.36	32.10
20	744.47	21.04
21	720.00	36.50

Table A.3: Critical temperature and pressure for each surrogate component.

A.2.2 Liquid density

Comp	A_ρ	B_ρ	C_ρ
1	0.23220	0.26024	0.26940
2	0.23590	0.25668	0.28570
3	0.23440	0.25231	0.28960
4	0.23540	0.25561	0.27348
5	0.24350	0.25447	0.32380
6	0.23800	0.26963	0.27900
7	0.23410	0.26200	0.27130
8	0.24282	0.25391	0.28571
9	0.24467	0.26337	0.28571
10	0.26680	0.27028	0.29270
11	0.26180	0.26826	0.28571
12	0.28800	0.27116	0.29520
13	0.28597	0.26757	0.28571
14	0.28597	0.26369	0.28571
15	0.28597	0.26475	0.28571
16	0.29180	0.26188	0.29889
17	0.28760	0.26513	0.27410
18	0.27320	0.25222	0.29130
19	0.27760	0.25914	0.27982
20	0.27210	0.25690	0.32095
21	0.29980	0.25893	0.26770

Table A.4: Coefficients to calculate liquid density for each surrogate component based on Eq. (3).

A.2.3 Liquid dynamic viscosity

Comp	A_μ	B_μ	C_μ	D_μ
1	-5.9245	888.09	1.2955×10^{-2}	-1.3596×10^{-5}
2	-6.0716	1017.70	1.2247×10^{-2}	-1.1892×10^{-5}
3	-7.0687	1253.00	1.3735×10^{-2}	-1.2215×10^{-5}
4	-7.8717	1446.70	1.4940×10^{-2}	-1.2495×10^{-5}
5	-8.1894	1557.10	1.5270×10^{-2}	-1.2371×10^{-5}
6	-7.2033	979.69	1.6986×10^{-2}	-1.7924×10^{-5}
7	-4.8603	715.64	1.0793×10^{-2}	-1.2293×10^{-5}
8	-4.6058	827.75	7.8684×10^{-3}	-7.3286×10^{-6}
9	-5.7519	1086.50	9.4927×10^{-3}	-7.7577×10^{-6}
10	-1.9879	508.06	1.2152×10^{-3}	-2.7318×10^{-6}
11	-7.9515	1529.10	1.4023×10^{-2}	-1.1002×10^{-5}
12	-3.6981	916.71	3.9609×10^{-3}	-2.9206×10^{-6}
13	-4.6518	910.91	7.5034×10^{-3}	-6.2957×10^{-6}
14	-4.5546	858.14	7.5743×10^{-3}	-6.6918×10^{-6}
15	-4.3915	836.22	7.1422×10^{-3}	-6.2706×10^{-6}
16	-5.6379	910.54	1.0861×10^{-2}	-1.0251×10^{-5}
17	-7.8805	1250.00	1.6116×10^{-2}	-1.3993×10^{-5}
18	-6.9452	1127.60	1.3933×10^{-2}	-1.2344×10^{-5}
19	-4.8328	832.75	8.9147×10^{-3}	-8.5136×10^{-6}
20	-9.0835	1599.90	1.7555×10^{-2}	-1.3886×10^{-5}
21	-6.3710	1274.00	1.0494×10^{-2}	-8.1163×10^{-6}

Table A.5: Coefficients to calculate liquid dynamic viscosity for each surrogate component based on Eq. (11).

A.2.4 Liquid thermal conductivity

Comp	A_k	B_k	C_k
1	0.2229	-3.2988×10^{-4}	5.4691×10^{-8}
2	0.2218	-3.2560×10^{-4}	1.1282×10^{-7}
3	0.2292	-3.5926×10^{-4}	0
4	0.1956	-2.0000×10^{-4}	0
5	0.1996	-2.0000×10^{-4}	0
6	0.1864	-2.5000×10^{-4}	0
7	0.1900	-2.5667×10^{-4}	0
8	0.1938	-2.5000×10^{-4}	0
9	0.2018	-2.5000×10^{-4}	0
10	0.1555	-1.0944×10^{-4}	0
11	0.1793	-2.0000×10^{-4}	0
12	0.2076	-2.5000×10^{-4}	0
13	0.1550	-1.5556×10^{-4}	0
14	0.1550	-1.5556×10^{-4}	0
15	0.2091	-2.5000×10^{-4}	0
16	0.2099	-2.8557×10^{-4}	2.6919×10^{-8}
17	0.1873	-1.4690×10^{-4}	-1.2259×10^{-7}
18	0.1935	-2.4126×10^{-4}	5.9259×10^{-8}
19	0.1945	-2.0333×10^{-4}	0
20	0.1935	-2.0000×10^{-4}	0
21	0.1500	-6.6667×10^{-5}	0

Table A.6: Coefficients to calculate liquid thermal conductivity for each surrogate component based on Eq. (19).

A.2.5 Specific heat capacity

Comp	A_c	B_c	C_c	D_c
1	82.736	1.3043	-3.8254×10^{-3}	4.6459×10^{-6}
2	79.741	1.6926	-4.5287×10^{-3}	4.9769×10^{-6}
3	84.485	2.0358	-5.0981×10^{-3}	5.2186×10^{-6}
4	111.814	2.2092	-5.2555×10^{-3}	5.0865×10^{-6}
5	89.101	2.7062	-6.1478×10^{-3}	5.7520×10^{-6}
6	115.052	0.6577	-2.1698×10^{-3}	3.3303×10^{-6}
7	134.965	0.8146	-2.5182×10^{-3}	3.5416×10^{-6}
8	213.729	1.0747	-2.8164×10^{-3}	3.4514×10^{-6}
9	258.868	1.5606	-3.8431×10^{-3}	4.1357×10^{-6}
10	103.668	0.4622	-1.3973×10^{-3}	2.0550×10^{-6}
11	211.195	0.9626	-2.3470×10^{-3}	2.7780×10^{-6}
12	108.262	0.9578	-2.3377×10^{-3}	2.4579×10^{-6}
13	190.982	0.4250	-9.2118×10^{-4}	1.1739×10^{-6}
14	180.486	0.4898	-1.1269×10^{-3}	1.4549×10^{-6}
15	185.965	0.4531	-1.0267×10^{-3}	1.3443×10^{-6}
16	83.703	0.5167	-1.4910×10^{-3}	1.9725×10^{-6}
17	56.460	0.9493	-2.4902×10^{-3}	2.6838×10^{-6}
18	123.471	0.6197	-1.6883×10^{-3}	2.1608×10^{-6}
19	83.637	0.8786	-2.3192×10^{-3}	2.5989×10^{-6}
20	139.356	0.7940	-1.8805×10^{-3}	2.3121×10^{-6}
21	154.318	0.3523	-7.7637×10^{-4}	1.0223×10^{-6}

Table A.7: Coefficients to calculate liquid specific heat capacity for each surrogate component based on Eq. (27).

A.2.6 Latent heat of evaporation

Comp	A_L	B_L
1	59.0771	0.439
2	71.4282	0.451
3	77.1658	0.407
4	86.8851	0.418
5	96.6800	0.422
6	49.9169	0.408
7	59.5032	0.481
8	70.7797	0.380
9	87.1109	0.380
10	49.4195	0.415
11	73.9481	0.380
12	58.8676	0.380
13	67.8685	0.380
14	64.0928	0.380
15	65.0708	0.380
16	50.1390	0.383
17	55.6060	0.375
18	60.1072	0.397
19	60.0700	0.365
20	81.3400	0.410
21	59.4549	0.308

Table A.8: Coefficients to calculate latent heat of evaporation for each surrogate component based on Eq. (35).

A.2.7 Saturated vapor pressure

Comp	A_p	B_p	C_p
1	7.14462	1498.96	225.874
2	7.21745	1693.93	216.459
3	7.22883	1807.47	199.381
4	7.26165	1914.86	183.519
5	7.36235	2094.08	180.407
6	7.05830	1340.21	230.768
7	7.12709	1473.84	229.440
8	7.03727	1632.18	181.835
9	7.07426	1828.55	154.450
10	7.00107	1375.13	232.819
11	7.10051	1835.18	189.998
12	6.82768	1544.81	204.090
13	6.90824	1729.18	194.350
14	6.91430	1643.57	199.480
15	6.91266	1665.76	198.150
16	7.13620	1457.29	231.827
17	7.14914	1566.59	222.596
18	7.18167	1655.21	225.615
19	7.26105	1695.83	222.415
20	7.25666	1945.86	198.582
21	7.16735	1806.14	213.732

Table A.9: Coefficients to calculate saturated vapor pressure for each surrogate component based on Eq. (43).